1-1-2010

Develop Sonic Infrared Imaging Nde For Local Damage Assessment In Civil Structures

Qi He
Wayne State University

DEVELOP SONIC INFRARED IMAGING NDE FOR LOCAL DAMAGE ASSESSMENT IN CIVIL STRUCTURES

by

QI HE

DISSERTATION

Submitted to the Graduate School

of Wayne State University,

Detroit, Michigan

in partial fulfillment of the requirements

for the degree of

DOCTOR OF PHILOSOPHY

2010

MAJOR: ELECTRICAL ENGINEERING

Approved by:

_____

Advisor Date

_____

_____

_____

ACKNOWLEDGMENTS

First of all, I would like to express my deep and sincere gratitude to my supervisor, Professor Xiaoyan Han, Ph.D., Electrical and Computer Engineering Department, College of Engineering, Wayne State University. Her knowledge and her logical way of thinking have been of great value for me and provided a good basis for this research. Her understanding, encouraging guidance and support have shed light on the path of this research work. She provided detailed and constructive comments, and important support throughout this work.

I warmly thank Professor Lawrence 'Skip' Favor, Ph.D., Physic Department, College of Science and Liberal Arts, Wayne State University, for his valuable advice and friendly help. His extensive discussions around my work and interesting explorations in operations have been very helpful for this study.

My sincere thanks are due to the members of my doctoral dissertation committee, Professor Pepy Siy, Ph.D., Professor Golam Newaz, Ph.D., and Professor Hao Ying, Ph.D., for their inestimable time and patience to help me get through this work.

During this work I have collaborated with many colleagues for whom I have great regard. I like to thank my colleagues and also friends — Wei Li, Yuyang Song, A.S Abhijith ,Zeeshan Ahmed, Xinyue Zhao and Ding Zhang for their help and friendship, and I wish to extend my warmest thanks to all those who have helped me with my work

in the Electrical and Computer Engineering Department and Physic Department in Wayne State University.

I owe my loving thanks to my wife Qin Su, my sons Jacob Zun He and Ray Su. They had sacrificed so much for me. Their love and support without any complaint or regret has enabled me to complete this project. Without their encouragement and understanding it would have been impossible for me to finish this work.

My special gratitude is due to my father, Jinyu He, my mother, Shuxian Luo, my brother, Ying He and his family for their loving support.

This project was sponsored in part by NSF CMS-0511046, in part by the DOT/FAA William J. Hughes Technical Center's Airworthiness Assurance Center of Excellence (AACE), in part by NSF Career Award No. CMS-0238622 and in part by the Institute for Manufacturing Research, Wayne State University. The financial supports by these sponsors are gratefully acknowledged.

TABLE OF CONTENTS

LIST OF TABLES

LIST OF FIGURES

CHAPTER 1

INTRODUCTION

Civil Engineering is one of the oldest of engineering disciplines in the human world. Since our ancestors built-up their first hut, engineers had started fighting a battle to keep the civil engineering structures stand. Civil Engineering Structures fail for various reasons. The primary causes of civil engineering structures failures are:

- Human factors (bad construction quality and accidents)
- Design flaws (results of lack of knowledge or unethical practices)
- Material failures (caused by ageing or fatigue)
- Extreme conditions natural environments (hurricane, earthquake, etc.)
- Combinations of the above

The integrity and stability of civil infrastructure have far-reaching economic and social importance. Aging and deterioration can lead to catastrophic failures in civil infrastructure, resulting in loss of not only capital but also, potentially, life. While tougher laws and regulations were instated to prevent unethical engineering practices, maintain construction quality and reduce accidents; engineering schools in universities worked hard to provide sufficient technological and ethical trainings for engineers; natural disaster warning systems were established to minimize the damage; technologies needed to detect the material problems before they fail and cause damage to structures and lose of human lives.

Civil engineering structures like buildings and bridges normally are constructed using materials like steel, concrete (cement) and wood. Recent years composite materials are also more and more often been seen in buildings. Engineers had

developed multiple techniques to detect the material failures when the civil engineering structures are under normal usage.

These techniques called Nondestructive Evaluation share a common goal which is to detect and notify operators of the fatigue and damage in civil structures, and then operators can do an assessment on the severity of the fatigue and damage which will lead to the decision on reparation procedures.

1.1 Nondestructive Evaluation (NDE):

Nondestructive Evaluation (NDE) is also known as **Nondestructive Testing** (**NDT**) and **Nondestructive Inspection** (**NDI**). The basic principle of NDE is simple. To determine the quality or integrity of an item nondestructively, simply find a physical phenomenon (the interrogating parameter) that will interact with and be influenced by the test specimen (the interrogated parameter) without altering the specimen's functionality. NDE is vital for constructing and maintaining all types of components and structures. To detect different defects such as cracking and corrosion.

Nondestructive Evaluation (NDE) is an interdisciplinary field of study which is concerned with the development of analysis techniques and measurement technologies for the quantitative characterization of materials, tissues and structures by noninvasive means. Ultrasonic, radiographic, electromagnetic, and optic methods are employed to probe interior microstructure and characterize subsurface features. NDT examines actual production pieces and reveals the presence of flaws which can be evaluated against accept/reject criteria. It is one of the major tools of quality control and is firmly entrenched in quality programs of industries such as aerospace, automotive, defense, pipe line, power generation, preventative maintenance, pulp and paper, refinery, and

shipbuilding. NDE plays the important role not only in the quality control of the finish products but also during various stages of manufacturing. Through the effective and reliable use of NDT methods, the modern concepts like total quality management that aimed to obtain almost defect free components, is possible. NDT is also used for condition monitoring of various items during operation to predict and assess the remaining life of the component while retaining its structural integrity.

The Nondestructive Evaluation (NDE) techniques had been widely adapted in manufacturing industry, airline plane safety inspection for decades. After several natural disaster like earthquake, hurricane and civil structure failure, such as The collapse of the Silver Bridge in Point Pleasant, West Virginia, on December 15, 1967 which resulted in the deaths of 46 people. The NDE of civil structures is put in the spot light. Traditional civil structure inspection method heavily relays on visual inspection with some nondestructive methods by structural experts. However, visual inspections reveal significant problems sometimes. Because the visual inspection is subjective and sometime it is not possible to access all members of structure, inspectors have to assume their hidden states. In this case, it is also very hard to make a final decision if inspectors have not enough information about that particular structure. Therefore, it is probable for inspectors to make somewhat conservative decision because of uncertainties, and to delay their decision after more detailed inspection. A rapid, accurate and easy-to-conduct inspection method like NDE is need. National Science Foundation (NFS), National Institute of Standards and Technology (NIST) and Federal Highway Administration (FHWA) all launched their own researches in early 70s. Many industry NDE techniques were revised to fit the new application.

1.2 Target of Civil Structure NDE Inspection

The civil infrastructure ages and deteriorates with time as a result of aging of materials, excessive use, overloading, climatic conditions, inadequate maintenance, and deficiencies in inspection methods. Extreme natural force like earthquakes and hurricanes can also bring the structural and nonstructural damage. All of these factors contribute to the obsolescence of constructed systems. As a result, health monitoring, repair, retrofit, rehabilitation, and replacement become necessary to ensure the safety of the public.

Corrosion and cracks of steel supporting structure are the main causes of damage and early failure of civil infrastructures. Hence, the targets of the Civil Structure Inspection are the inner steel supporting structure of buildings, bridges, highway deck and other civil infrastructure. The damage detection techniques need to determine the presence of the damage, determine the geometric location of the damage. From the safety consideration and the natural attributes of these civil infrastructures, the alternation of original structures must be reduced to the minimum. This requirement made the nondestructive inspection the ideal method for this kind application.

In general, damage detection techniques can be classified as four levels by their exactness and applicability.

- Level 1: Determination that damage is present in the structure
- Level 2: Level 1 plus determination of the geometric location of the damage
- Level 3: Level 2 plus quantification of the severity of the damage
- Level 4: Level 3 plus prediction of the remaining service life of the structure

Most NDE methods are categorized as Level 3 technology, which can determine geometric location and the severity of the damage. With the help of information on the building material and structure, the remaining service life can be calculated.

As soon as we have decided to employ NDE methods to improve product quality or ensure the integrity of a part, we are immediately facing another question --- Which MDE method to use? There are several levels to choosing an appropriate NDE method for a specific application. We must have a sense of what NDE methods would maximize the likely hood of detecting the flaw or material property of interest, while also considering economic, regulatory, and other factors.

The basic levels of choosing an NDE method are:

1. Understanding the physical nature of the material property or discontinuity to be inspected;
2. Understanding the underlying physical processes that govern NDE methods;
3. Understanding the physical nature of the interaction of the probing field (or material) with the test material;
4. Understanding the potential and limitations of the available technology;
5. Considering economic, environmental, regulatory, and other factors.

To employ any NDE method, we need to have reasonable knowledge of what we are looking for --- material prosperities, a discontinuity such as a void or crack, sheet or coating thickness; we might be also interested in the mechanical prosperities (elastic constants) or electromagnetic prosperities (conductivity, permittivity, or magnetic permeability). For discontinuities, we must not only be aware of their character, but also understand its relationship to the parent material, e.g. crack in a ceramic part had

different mechanical and electromagnetic prosperities than a crack in a steel part. And these two cracks need total different NDE method to detect.

In the research of a new NDE method, we not only must have a basic knowledge of how the various existing NDE methods work, but also must be aware of the potentials and limitation of the existing NDE technologies. And during the research we should keep in mind that just because there is consistency between the physical of the NDE method and that of the test part does not mean that equipment is available or has the sensitivity to measure the desired feature.

1.3 Current Civil Structure NDI/NDT Techniques

Current civil structure NDI/NDT methods includes acoustic or ultrasonic measurements, Magnetic field changes measurement, radiograph, eddy current, thermal field change detection technique, ground-penetrating radar and methods based on vibration measurement and based on changes in vibration characteristics.

Acoustic or Ultrasonic Measurements

In Ultrasonic Testing (UT), beams of high-frequency sound waves are introduced into materials so as to detect both surface and internal flaws. The sound waves travel through the material (with some attendant loss of energy) and are deflected at interfaces and/or defects. The deflected beam can be displayed and analyzed to assess the presence of flaws or discontinuities.

UT uses complex electronic equipment. Any material, which transmits mechanical vibrations, can be tested. UT detects both linear and non-linear flaws and permits three-dimensional interpretations. Evaluation is often difficult.

Magnetic field changes measurement

In Magnetic field Testing (MT), an internal magnetic field is generated in the tested specimen. In locations where flaws (non-magnetic voids) exist, some of the field will leak off the specimen and bridge the voids through the air. Magnetic (iron) particles dusted over the magnetized area are attracted by the leakage or external fields. Their buildups form a flaw indication.

MT usually requires electrical equipment to generate magnetic fields. Only metals, which can be magnetized, are tested by MT. The flaws do not have to be open to the surface but must be close to it. MT works best for flaws, which are elongated rather than round.

Radiograph

Radiograph Testing (RT) uses penetrating radiation and works on the principle that denser or thicker materials will absorb more of it. The specimen is placed between a source of radiation and a sheet of radiographic film. A flaw present anywhere within the specimen will absorb less radiation than the specimen itself. The flaw's presence and location will be indicated on the film by an area of higher or darker exposure.

The safety hazard inherent in RT dictates a special installation. Material density and its thickness set the limits of usefulness. Internal, non-linear flaws are RT's forte; its two dimensional views sometimes its drawback.

Eddy Current

In Eddy Current Testing (ET), an energized electric coil induces a magnetic field into the tested specimen. The fluctuating magnetic field generates an electric eddy

current. The presence of a flaw increases the resistance to the flow of eddy currents. This is indicated by a deflection on the instrument's voltmeter.

ET instruments are small and portable. The method is used only on electrically conductive materials, and only a small area can be inspected at a time.

Thermal Field Change Detection

Systems based on infrared thermography have been developed for the evaluation of bridge decks. The thermal IR images of the test example were taken for analysis. Because of the temperature difference of the damaged and undamaged areas, the damaged area will be showed ad the “bright spot” thermal IR images.

Infrared thermography is limited by environmental conditions and has difficulty evaluating decks with asphalt overlays.

Ground-Penetrating Radar

Ground-penetrating radar (GPR) is a geophysical technique that collects and records information about the subsurface. It is a technique that has been employed in such fields as engineering, geology, environmental studies, and more recently, archaeology.

It involves the transmission of high frequency radar pulses from a surface antenna into the ground. The elapsed time between when this energy is transmitted, reflected from buried materials or sediment and soil changes in the ground, and then received back at the surface is then measured. When many thousands of radar reflections are measured and recorded as antennas are moved along transects within a grid, a three-dimensional picture of soil, sediment, and feature changes can be created.

The GPR technologies have not satisfied the need for rapid, quantitative bridge deck assessment. Existing GPR systems require significant expert analysis to effectively evaluate deck condition, and have had difficulty providing fast and reliable results that satisfy the needs of state highway agencies.

Methods based on vibration measurement and based on changes in vibration characteristics

This method detects, locates and characterizes damage in structural and mechanical system by examining change in measured vibration response. The basic idea behind this technology is that modal parameters are functions of the physical properties of the structure (mass, damping and stiffness). Therefore change in the physical properties will cause detectable change in the modal properties.

All the modal properties include:

- Frequency Changes
- Mode Shape Changes
- Mode Shape Curvature/Strain Mode Shape Changes

Other similar methods include:

1. Methods based on dynamic measured flexibility
2. Methods based on updating structural model parameters

However, this method’s effectiveness greatly depends on prior analytical models and/or prior test data for the detection and location of damage. (Such as Finite Element Model and/or data set from undamaged structure)

Sonic IR imaging technique can be categorized in the thermal field change technique. However Sonic IR Imaging introduced external excitation source, with the

excitation of the ultrasonic wave, it would be easier to “light up” the damaged area and identify them. Sonic IR imaging technique is capable for using as a civil structure damage identification technique. With certain modification, it could be used as a damage identification tool for civil infrastructure assessments.

1.4 Objective of the Research Work:

Analysis of feasibility of adaptation IR Imaging in Civil Structure:

Sonic IR was originally developed for small scale structure and it has been tested on several different materials from metal to composite materials. We had observed very promising results. Now we intend to extend the use of Sonic IR imaging to civil structures. Modern large scale structures like, buildings and bridges use steel channels and beams as supporting structure. Damages to these supporting structures will lead to the failure of the entire structure. In this research we will apply the Sonic IR imaging NDE technology on large scale channels and beams to test its effectiveness. Different concrete samples with different crack and defects are tested by Sonic IR Imaging technique. So far, we have had very encouraging results from the experiments. After this study, we will find out the full capability of Sonic IR Imaging to be a new technique in civil structure NDI.

Study of IR images and thermal analysis on civil structures:

This part includes the collecting of the corresponding IR images using infrared cameras and the applications of proper image processing techniques on them to study the temperature distribution along the cracks. In order to get more accurate temperature increment and distribution pattern on samples, IR cameras will be carefully calibrated and thermal energy analysis and other corresponding work will be done on the IR

images. We will also study the propagation of the sound in concrete structure. With the help of Laser vibrometers, we can study the 3D motion of the crack surfaces of different samples, including out of plane shearing motion, in plane shearing motion and the motion in which the crack periodically opens and closes in synchronism with the ultrasonic waves. Using wave analyzing tools their frequencies, wave patterns, acoustic energy etc. will be analyzed under different boundary conditions i.e. changing the ultrasonic gun position, sample orientation, coupling material, contact pressure between gun & sample, pulse duration etc.

Simulation Work:

This part includes the employment of finite element analysis (FEA). We will use the finite element method to model different civil structures using FEA simulation software. All the models will be use as input for computation, and from the results we can simulate all the vibration pattern, friction, heat generation and temperature distribution on different structures, materials, equipment settings etc. From the simulation work, we can both have a point of view from the theoretical perspective and data comparison with experimental works.

Design of a new Sonic IR imaging system specific for civil structures:

The ultrasonic vibration infused to the samples causes friction at the crack surfaces and generates heat. Although the idea is very simple, with different simple material and attributes, then chose of equipments and system setups will greatly affect the results we got from the Sonic IR Imaging system. The current Sonic IR Imaging system was design to detect defects in metal parts; to meet this requirement; it is using

relatively less powerful ultrasonic gun and IR cameras with shorter integration time and faster speed. With concrete civil structure with lower elasticity and thermal diffusivity, we need to redesign the system with more powerful ultrasonic gun, different gun driving system and IR cameras with longer integration time and lower speed. With the new system, we can put more excitation energy into the structure and catch the defects, which will show up a lot later than their counterparts in metal parts.

The follow research works were listed in my thesis:

(i) Experiment results of applying the Sonic IR Imaging technology on different civil structures.

(ii) Build civil structure Finite Element model and compare the result with the experiment result.

(iii) Finite element model simulation of heat generation under the different frequencies of acoustic excitation sources and compared the results from different excitation source, find out how excitation source affect the heat generation in civil structure.

(iv) Build up finite element models for crack, analysis both structural and thermal behaviors under different conditions.

CHAPTER 2

Sonic IR Imaging NDE Technology

The basic idea of Sonic IR imaging NDE Technology is simple and straightforward - fraction generates heat. In the Sonic IR imaging technology, a short pulse of ultra-sonic sound wave, normally range from 20 kHz to 40 kHz with a pulse length of 500 ms to 800ms, is infused into a sample through the coupling material by an ultrasonic transducer. As the sound wave propagates thought the sample in various directions, it works as an excitation source by causing the 2 surfaces of each crack and disband in this sample to rubber with each other. The frictions between crack surfaces produce heat and as a result temperature rises at the vicinity of that crack region. An infrared camera is used to detect this temperature rise as the captured images show it as a bright region with a relative higher gray-scale value. The IR images captured by the IR camera are processed by digital image processing software, and thus the presence of crack is detected. This is also true for detecting the delaminated area of a sample.

The following flowchart illustrated the steps of this whole process which had been described above. In the whole process, energy in the form of ultra-sonic wave was input in to the sample; and defects were detected by IR images recorder by IR cameras as the output.

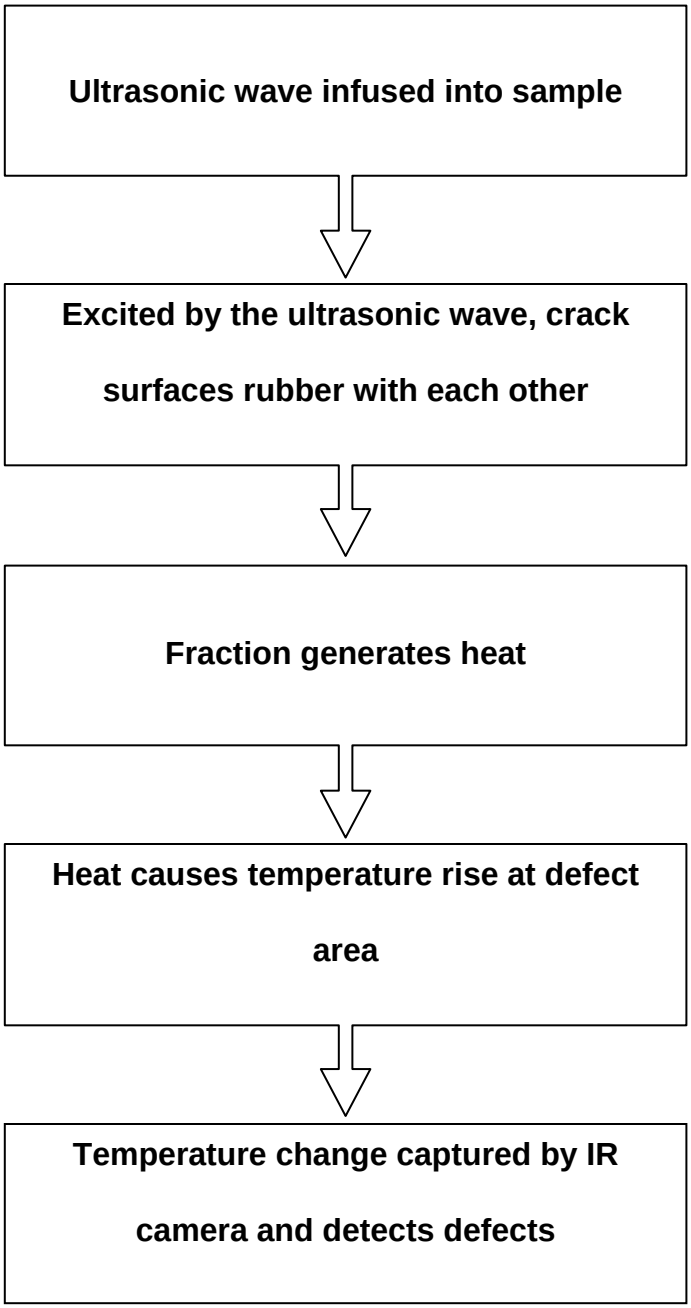

Flowchart 1: Sonic IR Imaging NDE Working Process

2.1 Sonic IR Imaging NDE System

From the name of Sonic IR Imaging, it is obvious that the whole system contains 2 major sub systems, which are Ultra-Sonic excitation subsystem and the Infrared Imaging subsystem. Other than these two major subsystems, there are some peripherals systems, such as laser vibrometer system and strain gauge system, were used during the research work. A typical Sonic IR Imaging NDE system with all subsystems is illustrated in Figure 2.1. In Figure 2.2 and 2.3 typical Sonic IR Imaging NDE experiment setup are demonstrated. In the following part of this chapter, one by one we will go through all the subsystems and peripherals systems of Sonic IR Imaging NDE system. After this, we will get a through and clear understanding how Sonic IR Imaging NDE works and what it can do.

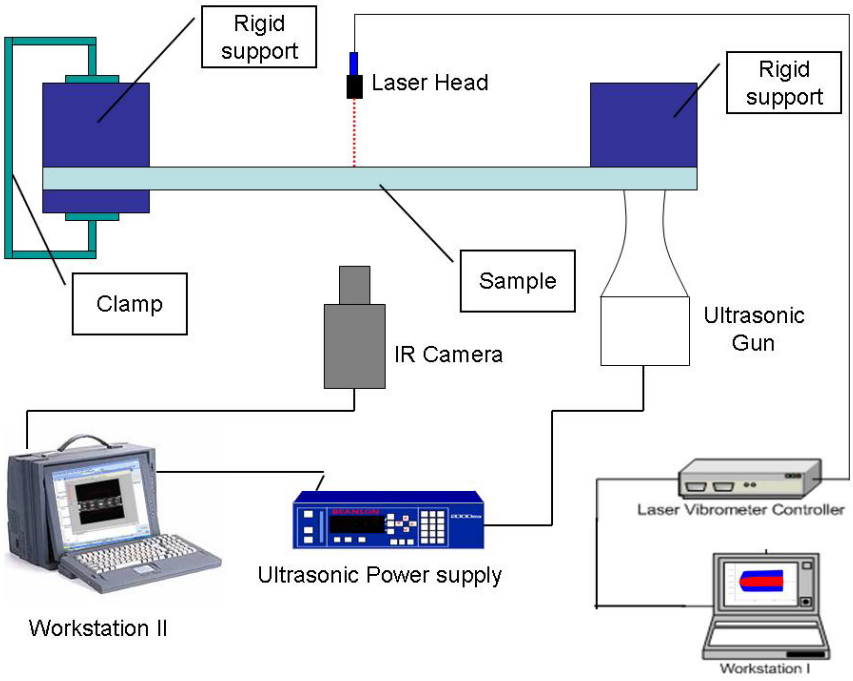

Figure 2.1: Typical Sonic IR Imaging NDE System

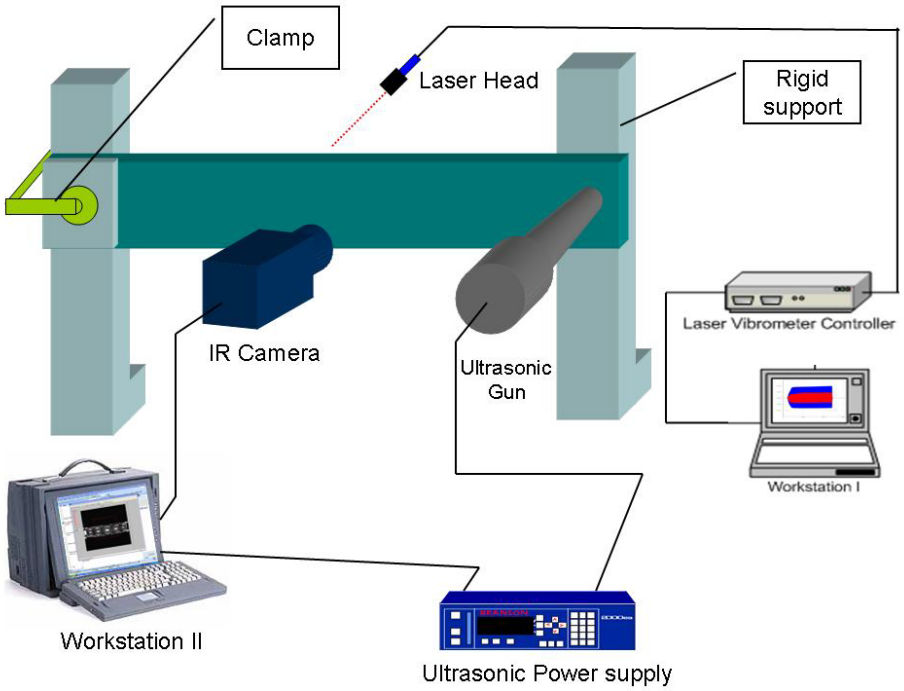

Figure 2.2: Typical Sonic IR Imaging NDE Equipment Setup

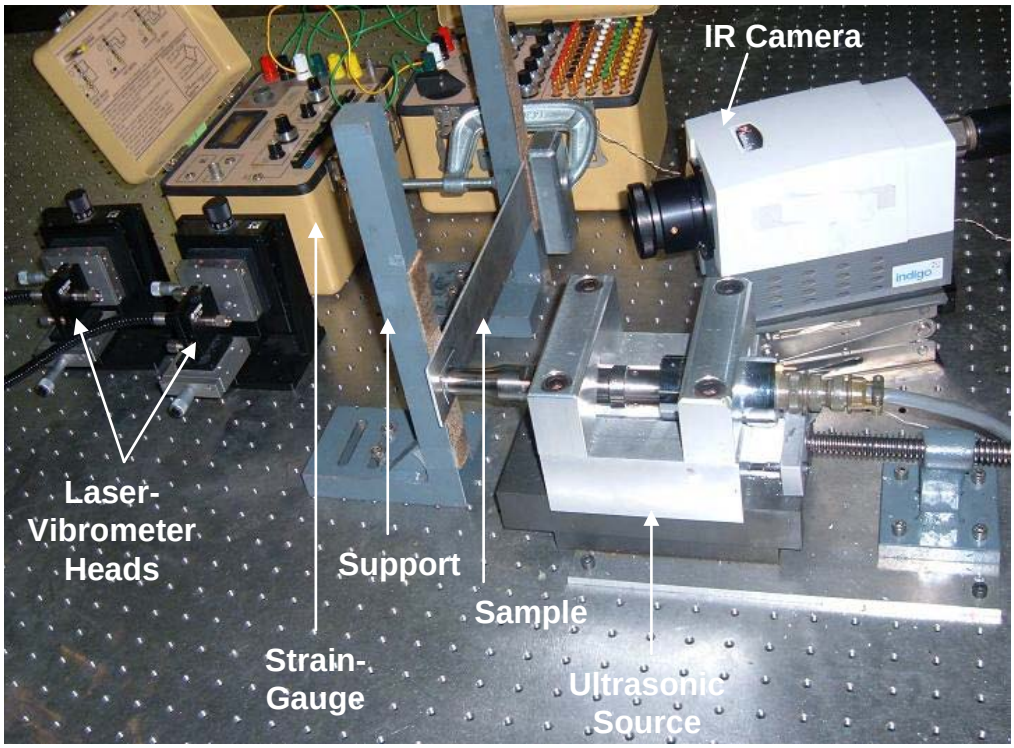

Figure 2.3: Photo of the major components in a typical experiment setting

2.2 The ultrasonic excitation subsystem:

In the Sonic IR Imaging NDE working process, the first subsystem we will meet is the ultrasonic excitation subsystem. The ultrasonic excitation subsystem is responsible for generating ultrasonic wave as the excitation source to be infused into the sample.

An ultrasonic plastic welding system manufactured by Branson® Ultrasonics Corporation was adapted and modified to fit the requirement of Sonic IR Imaging NDE system. The Branson® ultrasonic excitation system consists of the power supply and the actuator (also known as the ultrasound transducer) which contains converter, booster, and horn. Figure 2.4 showed all the components of the Branson ultrasound excitation system.

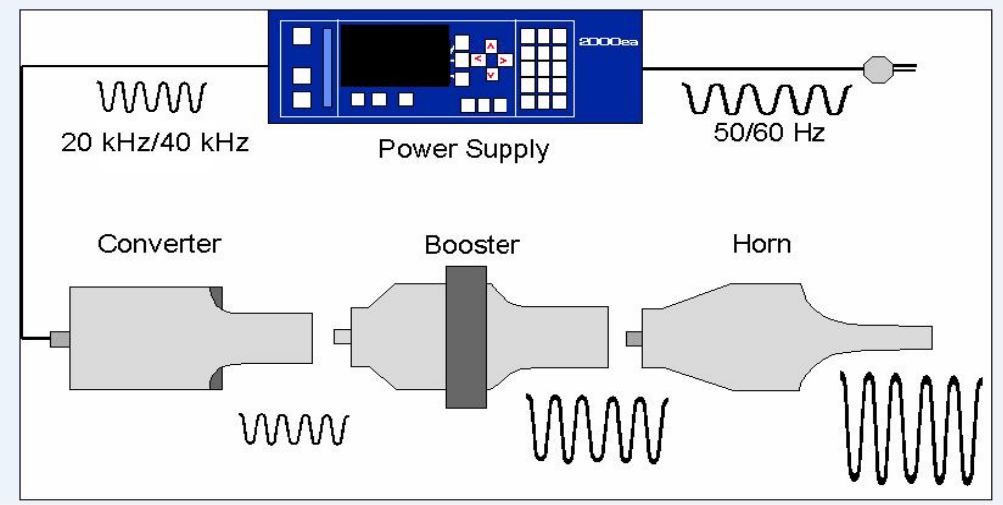

Figure 2.4: Mechanism of ultrasonic power supply

The power supply

The power supply consists of an ultrasonic power supply module and a system controller. The ultrasonic power supply module coverts conventional 50/60 Hz live current to 20/40 kHz electrical energy. The system controller controls the vibration system.

The Actuator

The actuator is an electro-pneumatic system that contains the Ultrasonic Stack (Converter/Booster/Horn) that delivers the force and ultrasonic energy to the work piece. The pneumatics are enclosed in the upper half of the actuator. The converter is mounted in the actuator as part of the ultrasonic stack. The ultrasonic electrical energy from the power supply is applied to the converter (sometimes called the transducer). This transforms the high frequency electrical oscillations into mechanical vibrations at the same frequency as the electrical oscillations. The heart of the converter is piezoelectric ceramic elements. When subjected to an alternating voltage, these elements alternately expand and contract, resulting in better than 90% conversion of electrical to mechanical energy. Success in ultrasonic assembly depends on the right amplitude of movement at the horn face. Amplitude is a function of horn shape, which is largely determined by the size and form of the parts to be assembled. A booster can be used as a mechanical transformer to increase or decrease the amplitude of vibrations applied to the parts through the horn. The horn is selected or designed for a specific application. Each horn is tuned typically as a half-wave section that applies the necessary force and vibration uniformly to the parts to be assembled. It transfers

ultrasonic vibrations from the converter to the work piece. The horn is mounted to the booster as part of the ultrasonic stack.

2.1 The IR camera system:

The IR camera system consists of a camera head and the computer based acquisition system. The IR camera head is a modular family of components that are mixed to cover mid-wavelength (MW) IR spectral regions. The focal plane array is in 640 by 512 format with 25 micron pixel pitch and direct injection up to 11 million electron well capacity. The IR camera system has snapshot readout with integrate while read and integrate then read capability, four video with a maximum total data rate of 40 MHz, and windowing capability with a minimum window size of 4 rows by 128 columns. The details are shown on table.1. The computer based acquisition system receives two high speed serial data streams from the camera head (400Mbits per second each), de-serializes and de-skews them, multiplexes them together and buffers the parallel data stream over to the frame grabber. It also provides the master clock and timing function for the camera system and receives as well as provides system synchronization signals to the external components.

Figure 2.5: The Camera Head

Figure 2.6: The Computer Based Acquisition System

Specifications	Infrared Camera
Spectral Range	1.5~5.0 microns
Resolution	640(H) x 520(V) pixels
Detector Size	25 x 25 um
Integration Time	<50 us
Max frame rate	100 fts in full frame; 22 kHz in smallest window(4x128)
Minimum Detectable temperature change	0.02K

Table.1: Technical data of infrared camera

Lens: INDIGO 13mm F/2.3 MWIR Len

INDIGO 25mm F/2.3 MWIR Len

2.3 The measurement procedure of a laser vibrometer:

Theory of interferometric velocity and Displacement Measurement

Optical interference can be observed when two coherent light beams are made to coincide. The resulting intensity, e.g. on a photo detector, varies with the phase difference $\Delta\varphi$ between the two beams according to the equation.

$$I(\Delta\varphi) = \frac{I_{\max}}{2} \times (1 + \cos\Delta\varphi) \qquad \text{Equation (1)}$$

The phase difference $\Delta\varphi$ is a function of the path difference ΔL between the two beams according to

$$\Delta\varphi = 2\pi \times \frac{\Delta L}{\lambda} \qquad \text{Equation (2)}$$

Where λ is the laser wavelength.

If one of the two beams is scattered back from a moving object (the object beam), the path difference becomes a function of time $\Delta L = \Delta L$ (t). The interference fringe pattern moves on the detector and the displacement of the object can be determined using directionally sensitive counting of the passing fringe pattern.

On scattering from the object the object beam is subjected to a small frequency shift which is called Doppler shift f_D and is a function of the velocity component in the direction of the object beam according to

$$f_D = 2 \times \frac{|V|}{\lambda} \qquad \text{Equation (3)}$$

Superimposing object beam and internal reference beam i.e. two electromagnetic waves with slightly different frequencies generates a beat frequency at the detector which is equal to the Doppler shift. The ratio Equation (3) to determine the velocity can be determined by introducing an additional fixed frequency shift f_B in the interferometer to which the Doppler shift is added with the correct sign. Thus the resulting frequency at the detector f_{mod} is given by

$$f_{\text{mod}} = f_B + 2 \times \frac{V}{\lambda}$$ Equation (4)

Interferometer of this type which are directionally sensitive are described as heterodyne.

Optical Configuration of the Laser Vibrometer:

The optical configuration of the Laser Vibrometer is shown schematically in Figure 2.7.

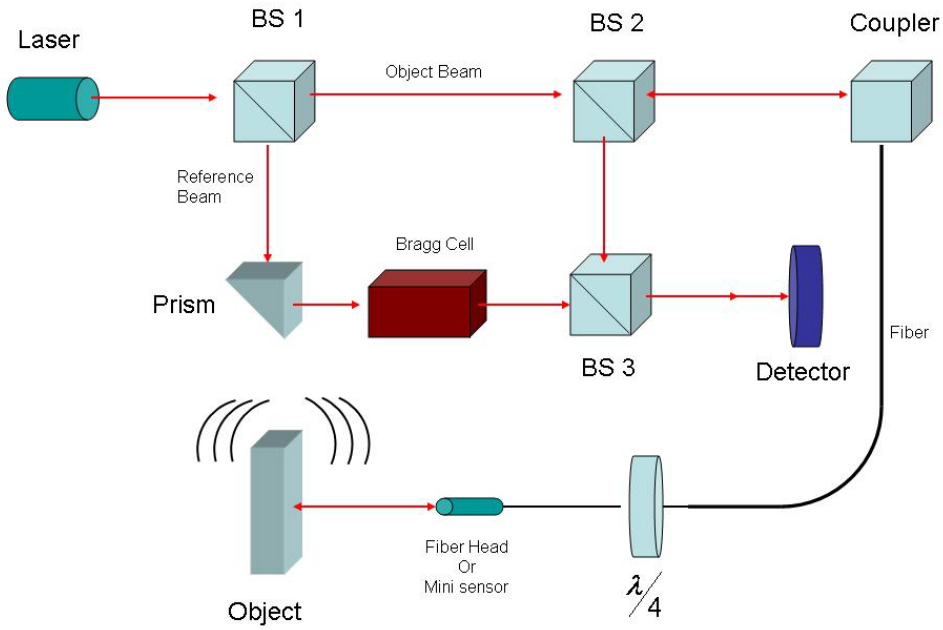

Figure 2.7: Schematic drawing of velocity/displacement measurement of Laser Vibrometer

The light source is a helium neon laser which provides a linear polarized beam. The polarizing beam splitter BS1 splits the beam into the object beam and the reference beam. The object beam passes through the polarizing beam splitter BS2 and is

focused into the fiber with an input coupler. The beam is then emitted from the end of the fiber, passes through a $\lambda/4$ plate, and deflects the object beam to the beam splitter BS3. As both arms of the “internal” interferometer are symmetrical. The optical path difference vanishes within the interferometer. The resulting path difference is equal to twice the distance between the beam splitter BS2 and the object. The Bragg cell in the reference arm generates the additional frequency offset to determine the sign of the velocity. The resulting interference signal of the object beam and reference beam is converted into an electrical signal in the photo detector and subsequently decoded in the controller.

Laser vibrometer parameters:

Specifications	Laser Vibrometer
Laser Type	Helium Neon
Wavelength	633nm
Cavity length	205mm
Output Center Frequency	40MHz
Max Sampling Frequency	2560kHz
Maximum Samples	67108864

Table 2: Technical data of laser vibrometer

2.4 The infrared image series acquired in Sonic IR Imaging technique:

The defects in target object detected by Sonic IR technique are shown as bright spots in infrared image series acquired by IR camera because of the temperature change due to the heat generation by the defect. The temperature change of the defective area is so small; the infrared image series usually need to do some image processing, such as subtraction, noise deduction, etc. to make sure the weak signals can be detected as well. In Figure 2.8, images were taken from result of an experiment done on an aluminum bar with a close crack 2mm in length at the center of one of its edges. The excitation source is 40 kHz ultrasound induced by transducer and the total duration of excitation pulse is 800ms. These images are results of subtractions by the average of first three images in this IR image series as background which was taken by the IR camera prior to the ultrasonic excitation, which was done to make sure that the IR image series only show the temperature changes in the aluminum sample. The temperature increases until the excitation source is turned off and the heat dissipation continues along the cracks. After the excitation pulse is off, the diffusely heated region decays in temperature. One can see the heat diffusion effect from the blurring of the defects. In Figure 2.9, temperature-time plots of the red spot indicated show the temperature change due to heating in the crack during the ultrasound pulse and cooling due to heat diffusion after the sound pulse.

The total duration of the excitation pulse is 800ms. The infrared camera imaging frame rate is 60 frames per second. The infrared camera starts to acquire images approximately 50 ms prior to the excitation pulse. All images were subtracted by the

average of first three images captured by IR camera. Averaging process of the background can effectively reduce the random noise in the background.

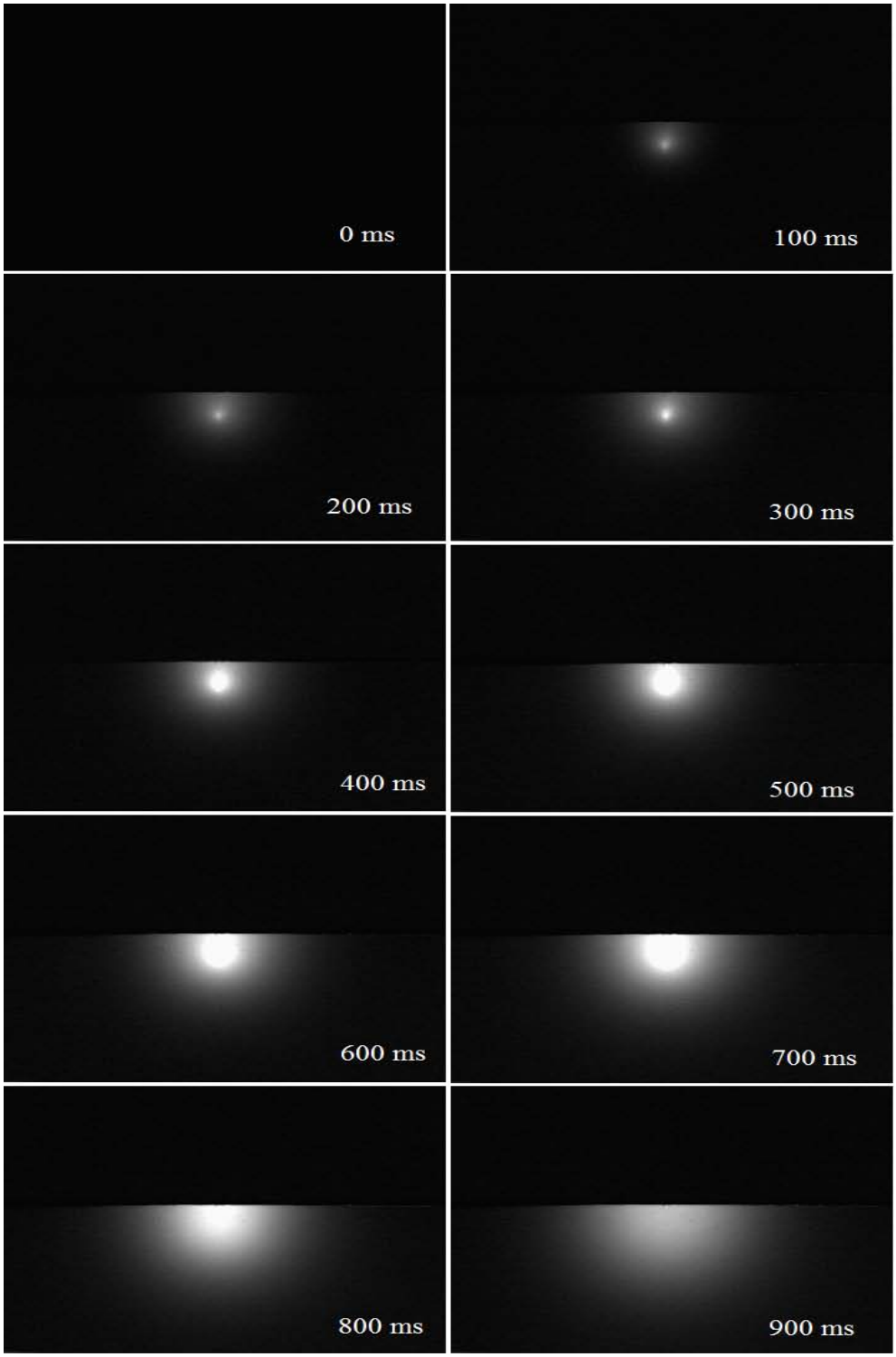

Figure 2.8: IR images taken at different times

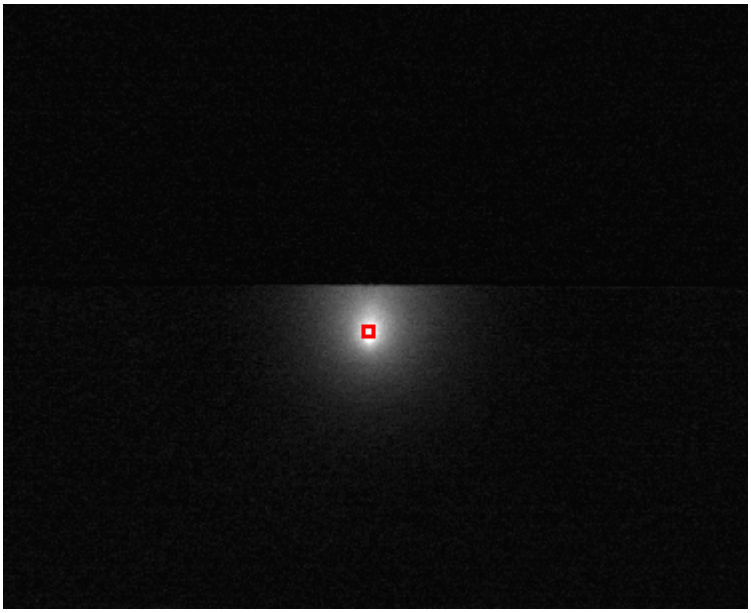

(a) Time-Temperature Plot Sampling Position (Red Square Position)

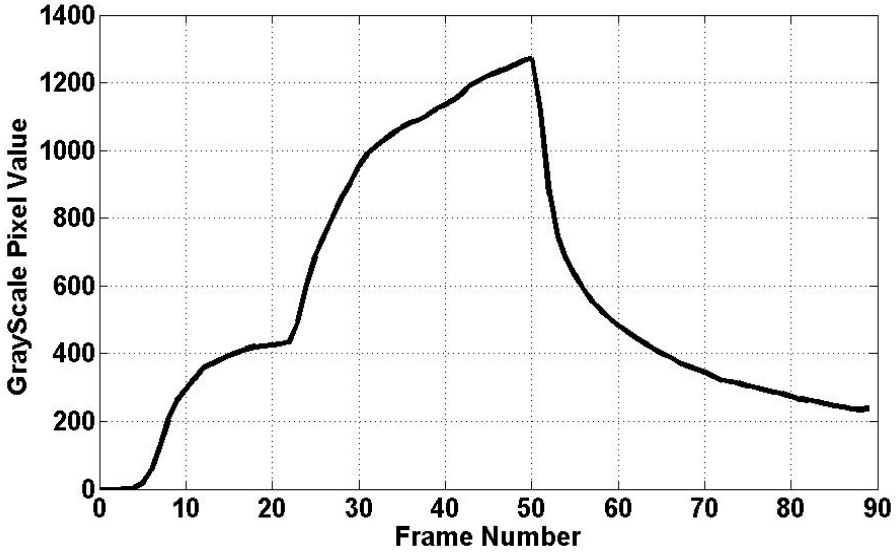

(b) Time-Temperature Plot

Figure 2.9: Temperature-time plots of red spot indicated on the IR image

CHAPTER 3

SONIC IR IMAGING EXPERIMENT RESULTS

In civil engineering structure during the ageing process of the structure, fatigue cracks will generate in girders/ beams and joints where structures bears stress and torque. Most common places for these fatigue cracks are girders/ beams, welding joints, bolt/rivet holes. Once these fatigue cracks appear, they will gradually grow till the whole structure give up. In Figure 3.1, the diagram shows the common positions of these structure and joints; the picture shows a fractured beam caused by structural stress.

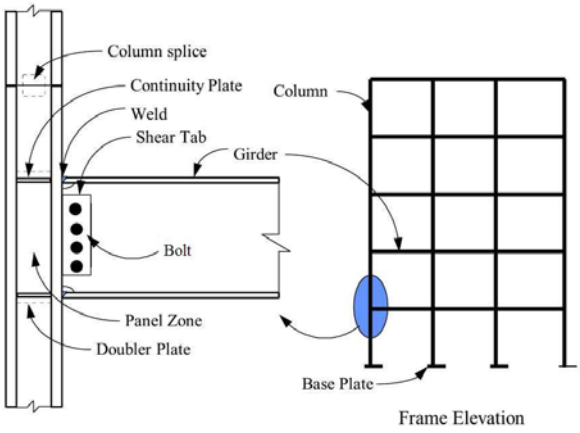

(a) Diagram of building and common joint structure

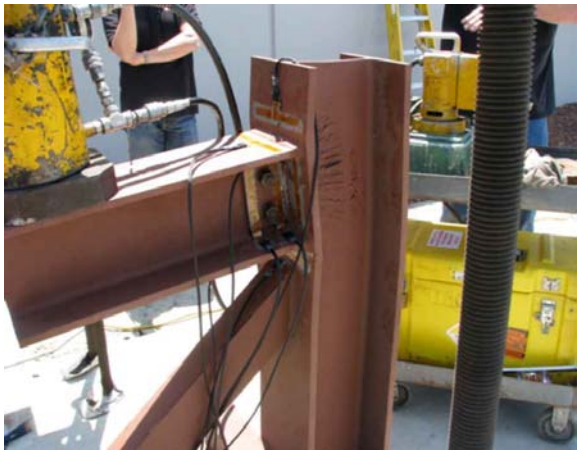

(b) Picture of a common joint structure

Figure 3.1: Common Joint Structure in Civil Structures

In order to prove that Sonic IR Imaging is an universal NDE technology for detecting structural crack can damage in civil engineering structures, experiments had been done to test the effectiveness of Sonic IR Imaging on all the common fatigues cracks listed previously. In the following part of this chapter, all the experiment results will be presented.

3.1 Typical Experiment Setup and Procedure

Experimental Equipment List:

1. Infrared Camera;
2. Ultrasonic Transducer;
3. Experiment Example.

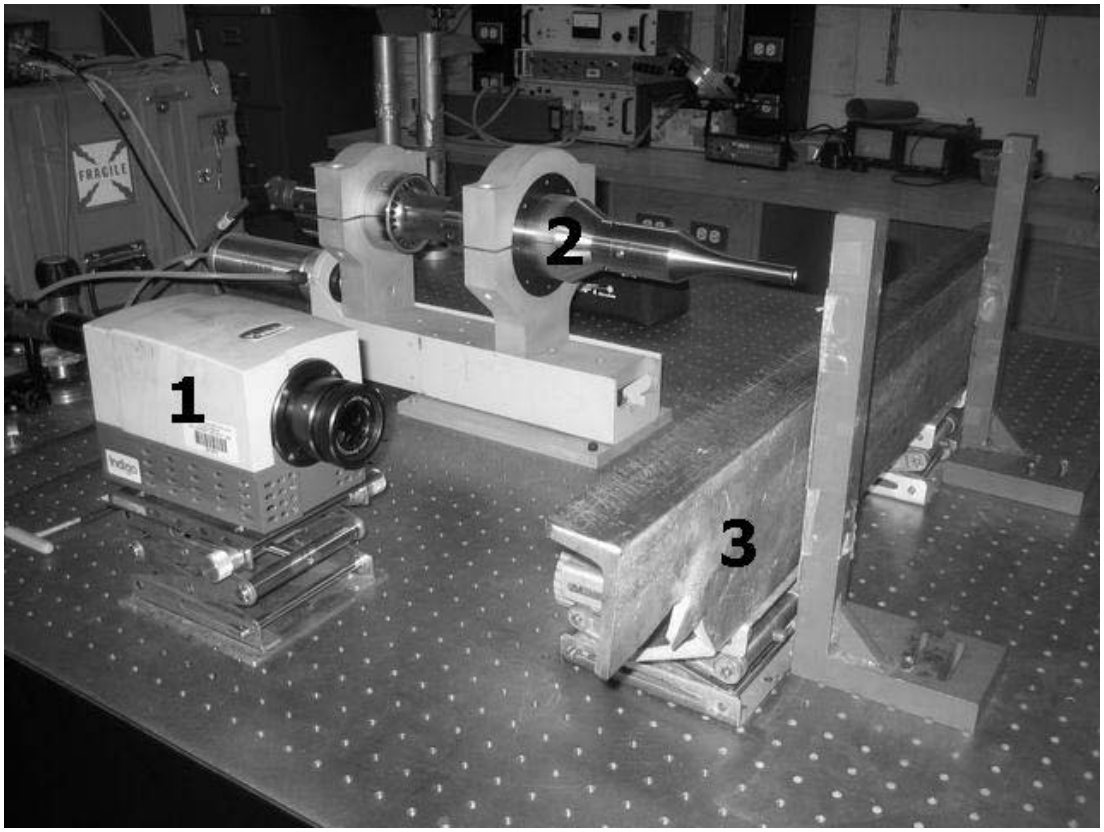

Figure 3.2: Typical Experimental Equipment Arrangement

Several other equipments are not shown in the picture above, which includes the system central control computer, trigger signal box, signal synchronize box and laser vibrometer.

During the experiment, a short pulse of ultra-sonic sound wave is infused into a sample through the coupling material by an ultrasonic transducer. As the sound wave propagates thought the sample in various directions, it works as an excitation source by causing the 2 surfaces of each crack and disband in this sample to rubber with each other. The frictions between crack surfaces produce heat and as a result temperature rises at the vicinity of that crack region. An infrared camera is used to detect this temperature rise as the captured images show it as a bright region with a relative higher gray-scale value. The IR images captured by the IR camera are processed by digital image processing software, and thus the presence of crack is detected by searching for these brighter regions which has higher temperatures.

3.2 Experiment of fatigue crack around bolt/rivet hole

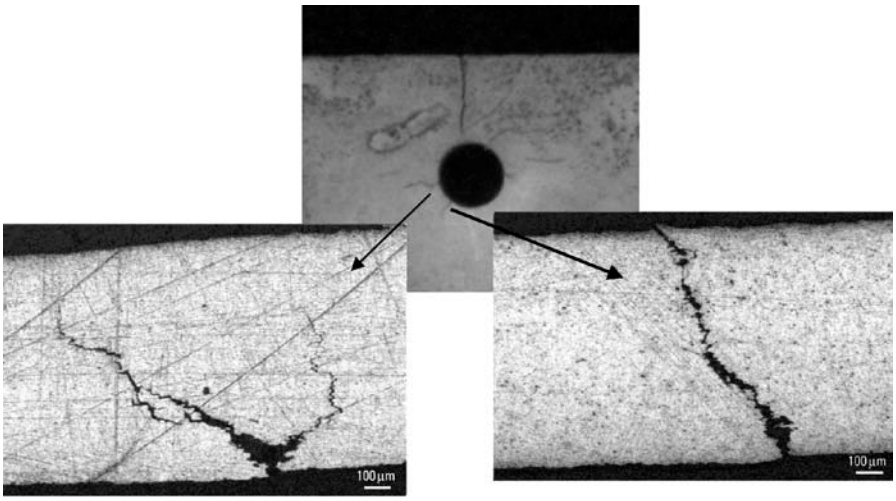

Source: Bellinger and Komorowski (1999)

Figure 3.3: Microscopic image of fatigue crack in bolt/rivet hole

Bolts and rivets are two of the most commonly used and structure joint methods in construction. They are placed in a hole and then fastened to join the two pieces of structures together. Under the load of the structure and the aging process, some of these holes holding the bolts and rivets will generate fatigue crack along the inner surface. Figure 3.3 shows one sample of the cracked bolt/rivet hole. These fatigue cracks will appear in a very small size, normally less than a millimeter, and then grow longer and longer causing the joint to give up. It is critical to find these fatigue cracks before they cause more serious damages to the joint and structure.

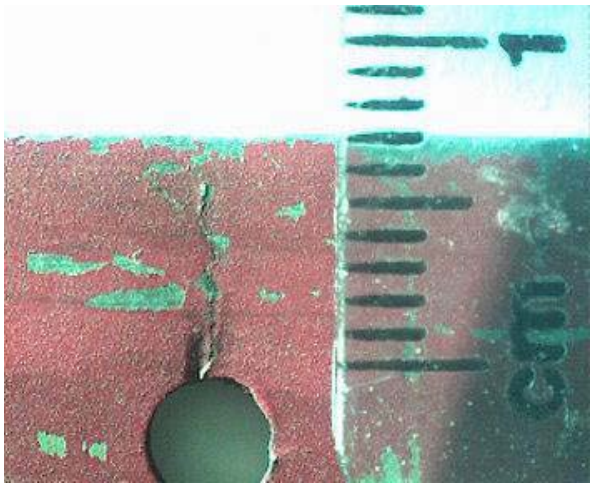

Figure 3.4: Sample of fatigue crack in bolt/rivet hole

In the experiment, an aluminum truss with a 6mm-length crack generated at a rivet hole was used as sample. A 40 kHz ultrasound pulse with length of 800 ms was induce into the sample. The IR camera captured the heat-up process at the crack region caused by the heat generated by the friction of the two surfaces of the crack. Figure 3.5 shows the heat up process at the crack region. These images are IR images with

background subtracted. High temperature area shows bright and low temperature shows dark.

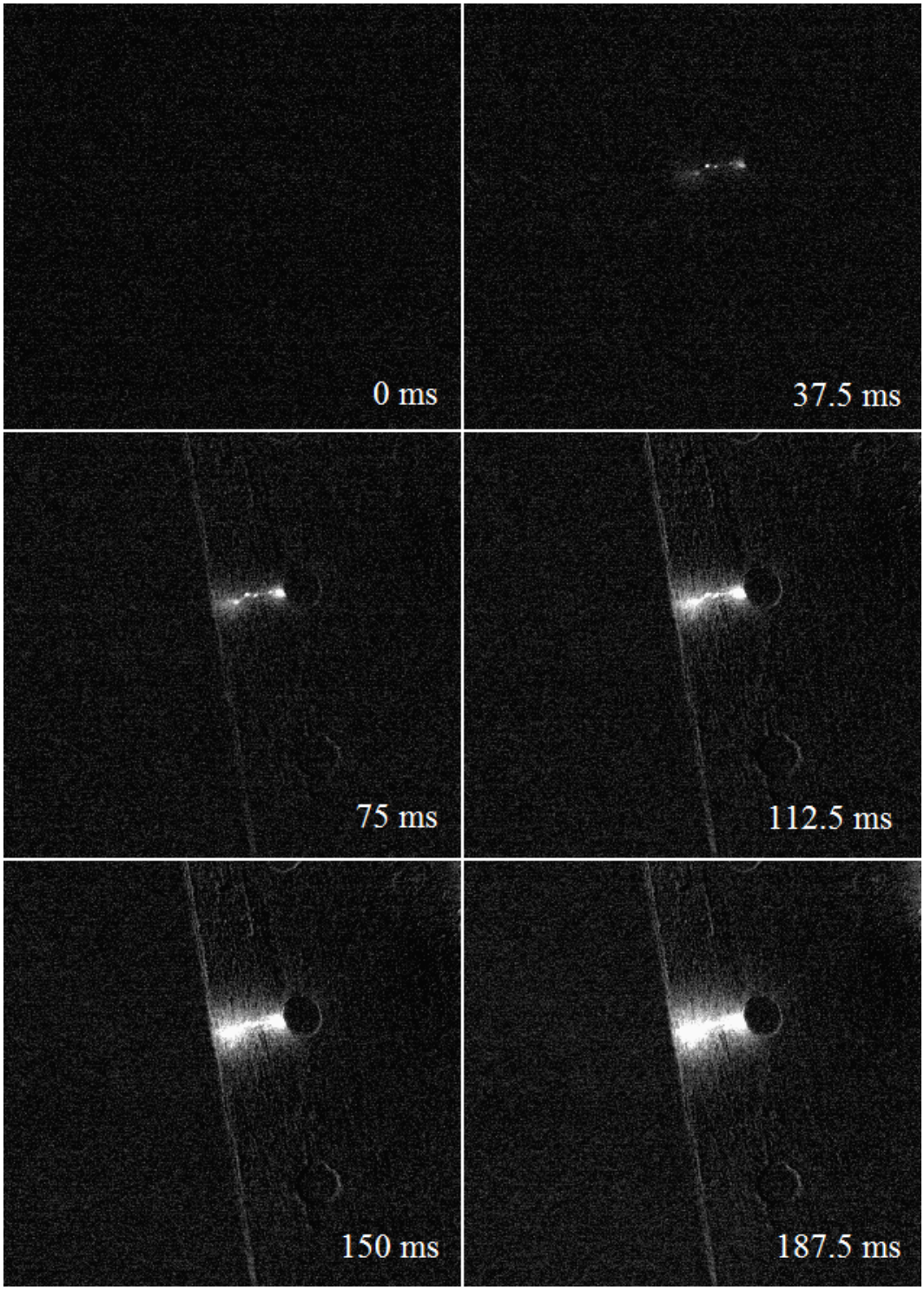

Figure 3.5: Rivet Hole Crack Heating process

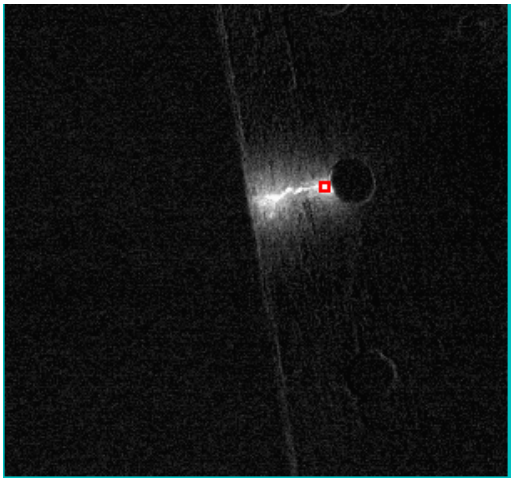

(a)

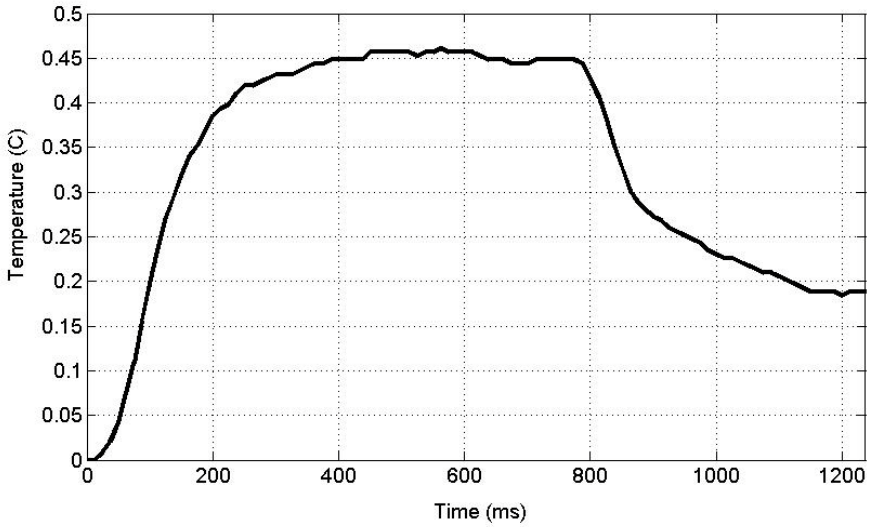

(b)

Figure 3.6: Time-Temperature Plot of the Crack

(a): Time-Temperature sampling position (red square)

(b): Time-Temperature sampling position

In Figure 3.6, the Time-Temperature plot extract from the IR image series captured during the experiment also confirms the temperature change along the crack is caused by the ultrasound excitation. From the Time-Temperature plot, it is obvious that the temperature started to rise at the beginning when ultrasound excitation starts. At

800 ms when ultrasound excitation was removed, the temperature along the crack starts to drop due to the removal of the heat source. The Time-Temperature plot shows the link between the temperature rise and the ultrasound excitation.

3.3 Experiment of cracks in welding joints

Welding is another wildly used joint method in construction works. Welding is a fabrication or sculptural process that joins materials, usually metals or thermoplastics, by causing coalescence. This is often done by melting the work-pieces and adding a filler material to form a pool of molten material (the weld pool) that cools to become a strong joint, with pressure sometimes used in conjunction with heat, or by itself, to produce the weld. This is in contrast with soldering and brazing, which involve melting a lower-melting-point material between the work-pieces to form a bond between them, without melting the work-pieces.

Many reasons can cause cracks in welding joints, including gas inclusions, non-metallic inclusions, lack of fusion, incomplete penetration, lamellar tearing. In many cases picking the wrong welding stick can also cause crack due to different contraction rate of the welding and base material during the cooling processes.

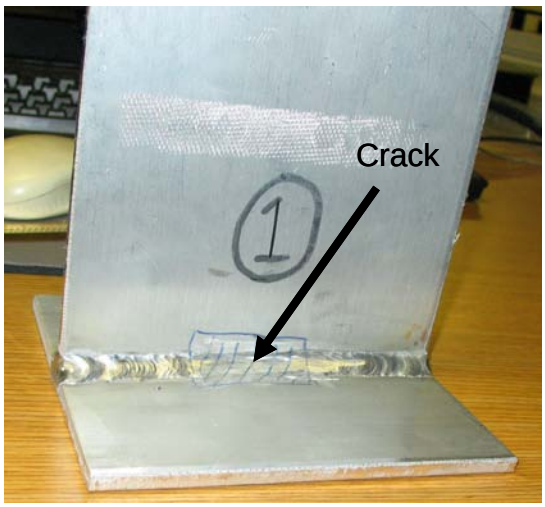

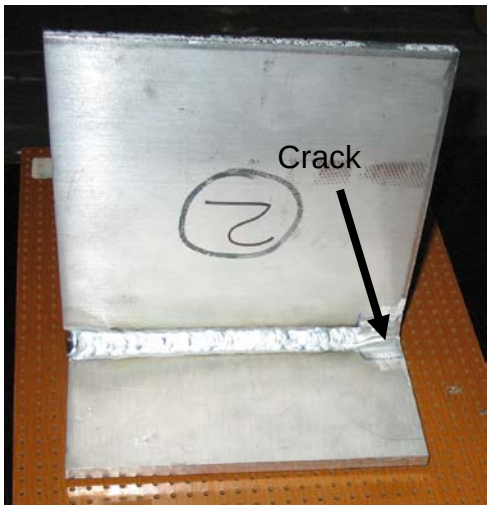

Figure 3.7: Optical Images of Welding Joint Crack Samples

Two samples were used for studying the effectiveness of sonic IR Imaging technology on welding joint crack. These samples have the same shape and size. Each of them contain 2 6in x 6 in x 0.25 in aluminum plate, with one welded to the middle of the other. They are marked as Sample 1 and Sample 2. Sample 1 has a crack at the center of the welding, and sample 2 has a crack on the edge. Figure 3.7 shows the detail of these 2 samples.

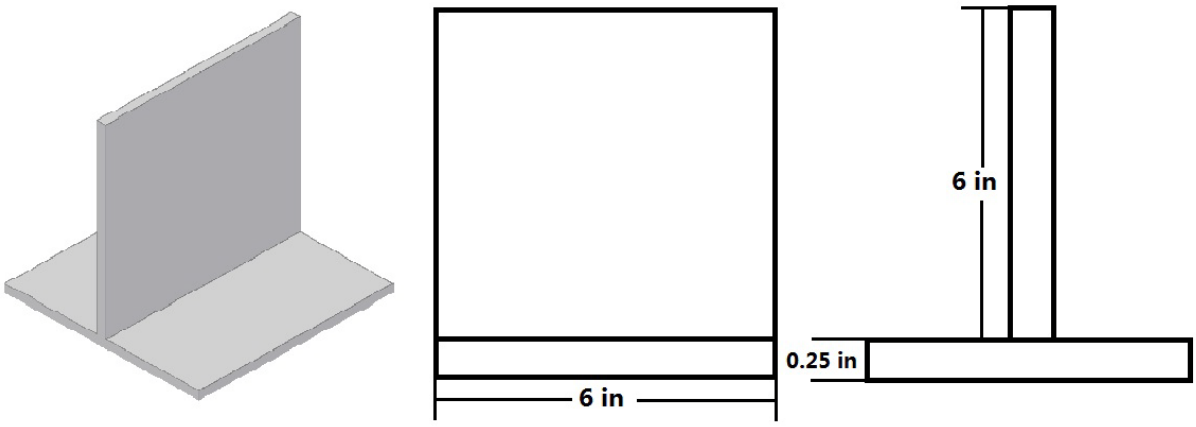

Figure 3.8: and Dimension of Welding Joint Crack Samples

A 40 kHz ultrasound pulse with length of 800 ms was induce into sample 1. The IR camera captured the heat-up process at the crack region. Figure 3.9 shows the time-temperature plot sampled at the center of the crack; Figure 3.11 shows the whole heating and cooling process at the crack region.

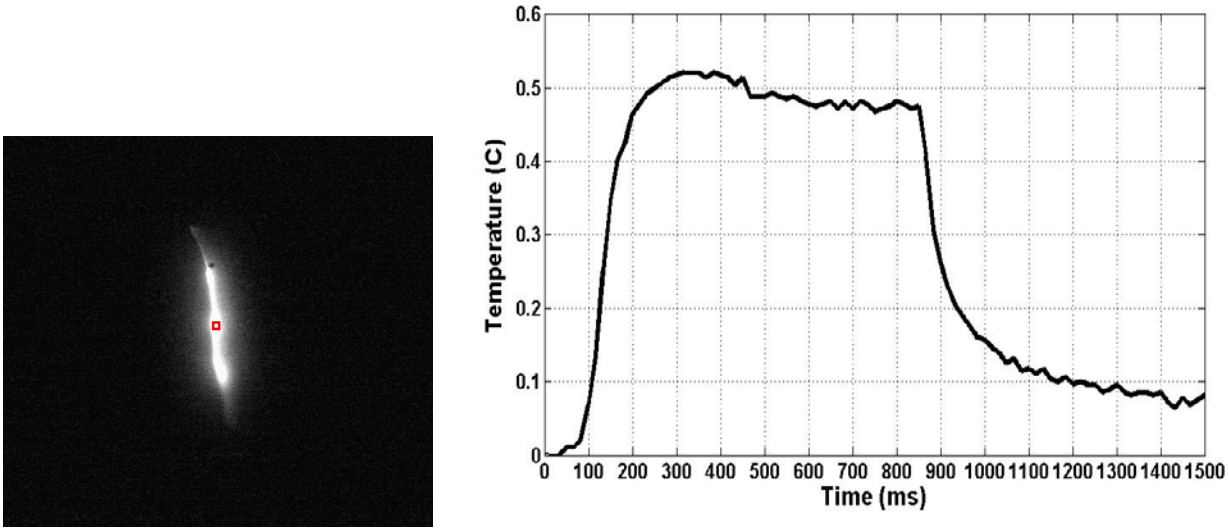

Figure 3.9: Sample 1 Crack Center Time-Temperature Plot

With Sample 2, an 800 ms 40 kHz ultrasound pulse was used to excite the sample. From the Time-Temperature Plot (Figure 3.10), we can see the temperature of the crack increased with the ultrasound excitation and dropped dramatically after the ultrasound was removed at 800ms. Figure 3.12 shows the whole heating and cooling process at the crack region.

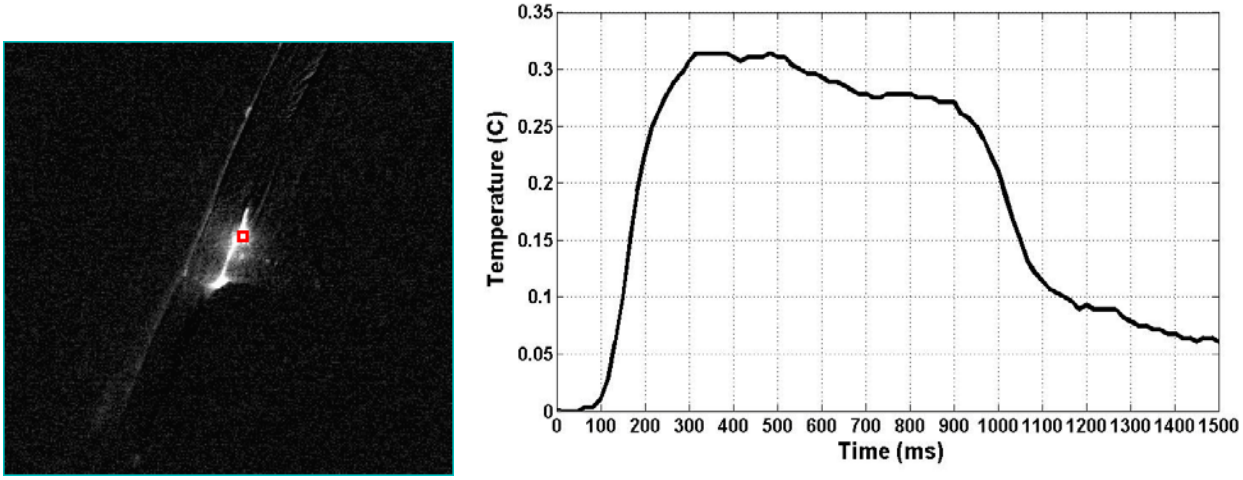

Figure 3.10: Sample 2 Crack Time-Temperature Plot (800ms)

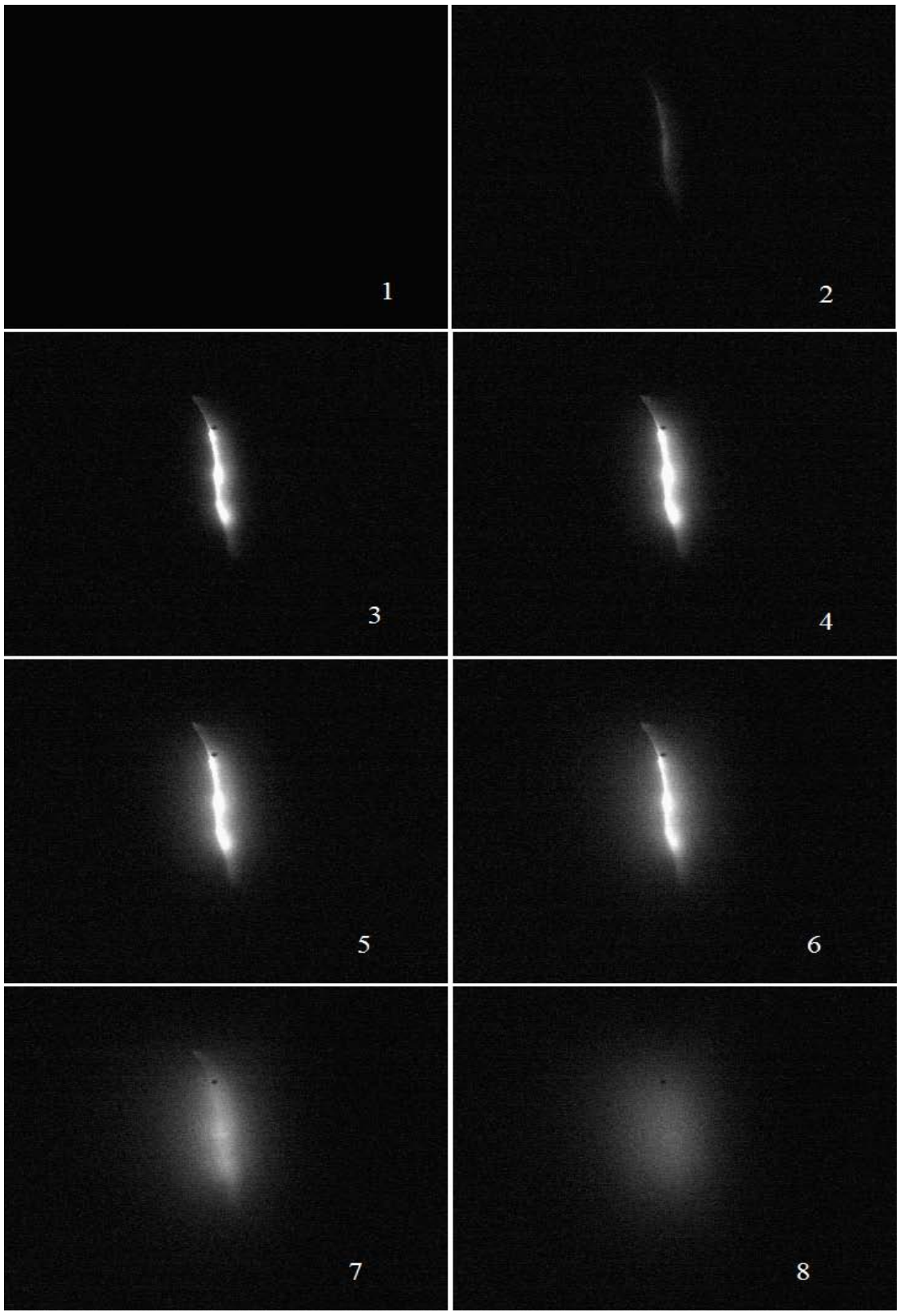

Figure 3.11: Sample 1 Crack Center Heating Process

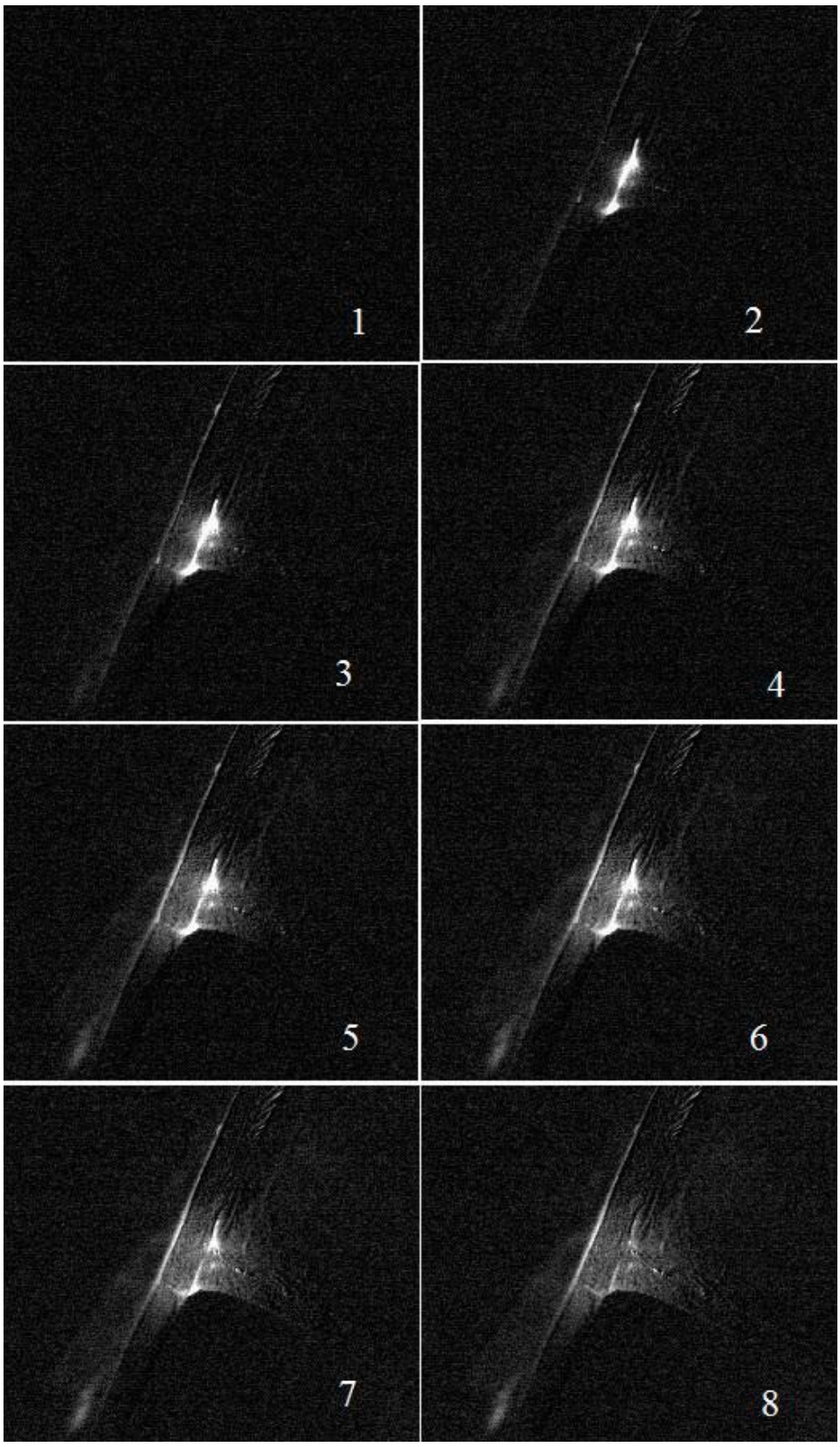

Figure 3.12: Sample 2 Crack Center Heating Process

3.4 Experiment of fatigue crack in girders/beams (steel C channel)

In the study of the fatigue crack generated in girders/beams, a steel C-channel was used as experiment example in the experiment. Following is detailed specification about the C-channel.

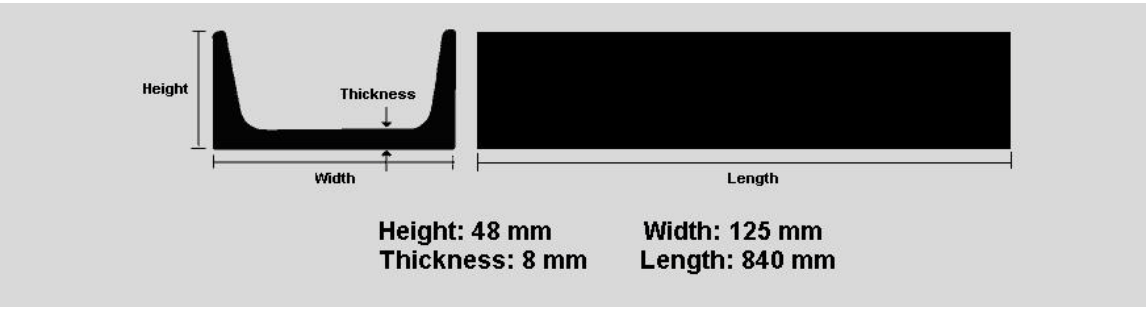

Figure 3.13: 3D Image and Specification of Experiment Example (C Channel)

In order to create a crack as close as possible to the real world situation, the C-channel was hammered multiple times, which resulted in fragments and cracks in the C-channel body as demonstrated in Figure 3.14. The square marked as Area of Interest (AOI) is the cracked area where will be examed by Sonic IR Imaging technology.

Figure 3.14: Optical Image of Experiment Example (C Channel)

In Figure 3.15 (a), 2 cracks, marked as A and B, are shown. These 2 closed cracks A and B have length of 80mm and 60mm respectively; crack B joined A at the middle. Ultra-sonic sound wave is infused into the C channel through the coupling material by an ultrasonic transducer at one end of the C-channel 650mm away from the cracks. In Figure 3.15 (b), heat generation can be easily observed by the different grey scale level along the crack A and B which had been marked respectively.

(a)

(b)

Figure 3.15: Optical and IR image of cracked area

(a) Optical image of part of the crack area (magnified 10X)

(b) Infrared image of cracks after ultra sound induced

For the purpose of heat pattern research, the temperature change history of the point with highest temperature along the cracks was recorder, as shown in Figure 3.16 (a). With the known camera filming speed of 80 frames per second and the camera calibration data providing the convert relationship between grey-scale and real temperature, the temperature change history had been interpreted into the time-temperature plot in Figure 3.16 (b).

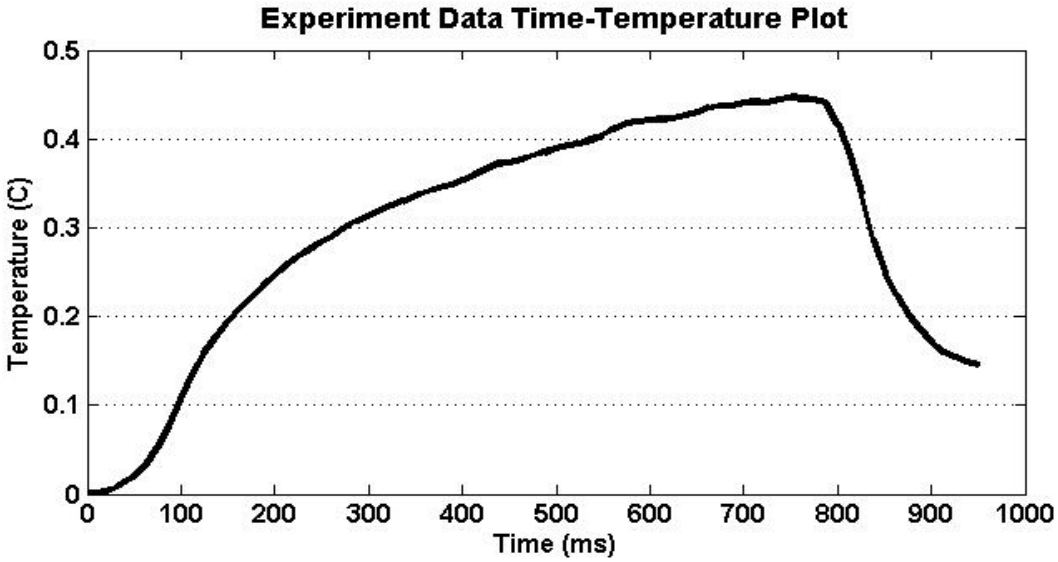

Figure 3.16: Time-Temperature Plot of the highest point in the image sequence

From the time-temperature plot, we can find that in the first 200ms the temperature change is nearly exponentially. After that, it slowed down and temperature became almost linearly, at the point of 780ms, when the ultrasonic excitation source was taken away, there was a temperature plunge.

3.4 Experiment on DTE boiler tubes

Four boiler tubes in Figure 3.17 were provided for Sonic IR Imaging Examination by DTE Energy. There are 2 types of tubes included; one is a longer and slimmer tube with outer diameter of 45mm and inner diameter of 33mm; the others are slightly shorter tubes with outer diameter of 50mm and inner diameter of 38mm. All the tubes have wall thickness of 6mm. As demonstrated in Figure 3.17, Tubes A, C and D are the shorter tubes; and tube B is the longer tube.

Figure 3.17: Sample boiler tubes used in experiment

Each of these 4 boiler tubes had been subjected to a thorough Sonic IR Imaging Exam. During the Sonic IR Imaging Exam, a short pulse of ultra-sonic sound wave is infused into the tubes ((Marked as 3 in Figure 3.18) through the coupling material by an ultrasonic transducer (Marked as 2 in Figure 3.18). As the sound wave propagates thought the tubes in various directions, it works as an excitation source by causing the 2 surfaces of each crack and disband in this sample to rub with each other. The friction activity between the crack surfaces produces heat and as a result temperature rises at the vicinity of that crack region. An infrared camera (Marked as 1 in Figure 3.18) is used to detect this temperature rise and is captured as an image showing it as a bright region with a relative higher gray-scale value. The IR images captured by the IR camera are processed by digital image processing software, and thus the presence of a crack is detected by searching for these brighter regions which have higher temperatures.

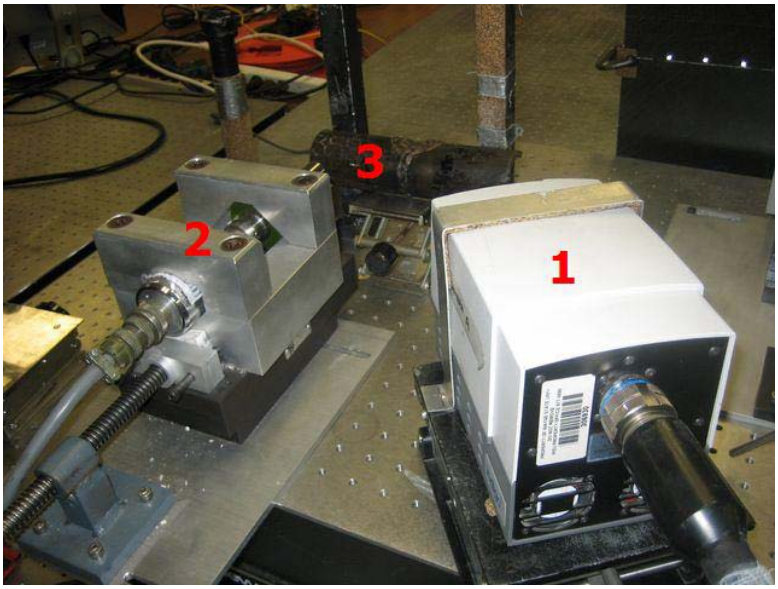

Figure 3.18: Experimental Equipment Arrangement

The experimental procedure is designed as a 3-step-procedure. Step 1, all of the 4 boiler tubes will go through a Sonic IR Imaging exam at Sonic IR Imaging Lab in the University; Step 2, the boiler tubes are sent back to the provider for X-Ray and destructive examination; Last step, the cut-open pieces are sent to Sonic IR Imaging Group again for another round of Sonic IR Imaging Exam, data acquired from these steps will be compiled for cross reference.

In the following section, experimental results of the boiler tubes will be presented and discussed, we will only focus on the part of the tubes where the welding activity was performed. These are the places where the cracks could initiate due to improper welding or uneven cooling process of welding heat affected zone.

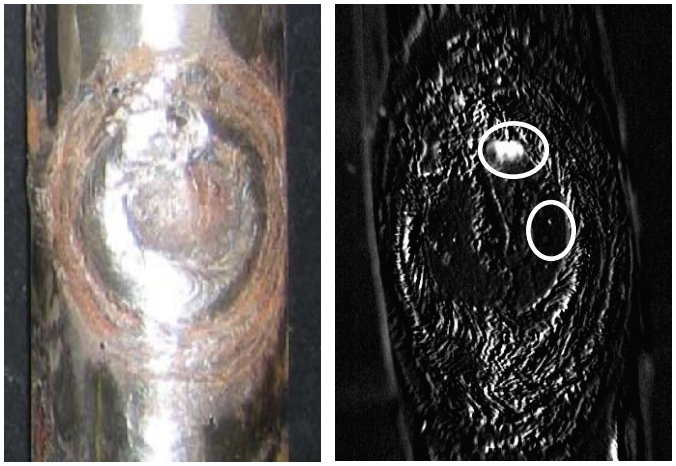

Tube A

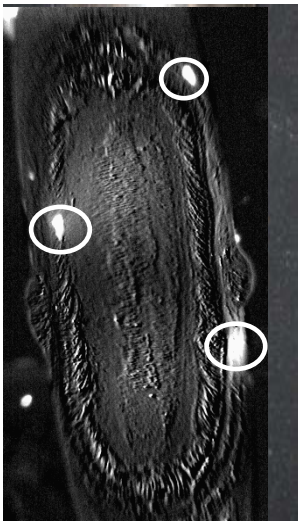

Tube B

Figure 3.19: Optical Images (left column) and first round IR Imaging results (right column) of the boiler tub

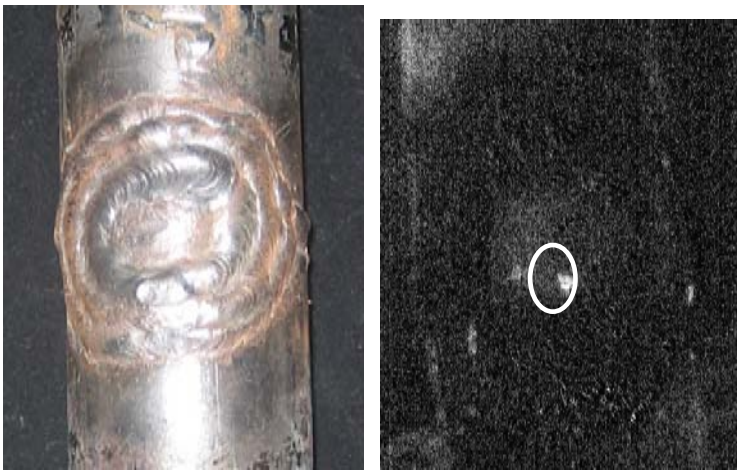

Tube C

Tube D

Figure 3.20: Optical Images (left column) and first round IR Imaging results (right column) of the boiler tubes (Cont'd)

As demonstrated in Figure 3.20, the images in the left Colum are optical images of the tubes; images in right column are IR Images. All the potential defects discovered in Sonic IR Imaging exam are marked by white circles in the IR images.

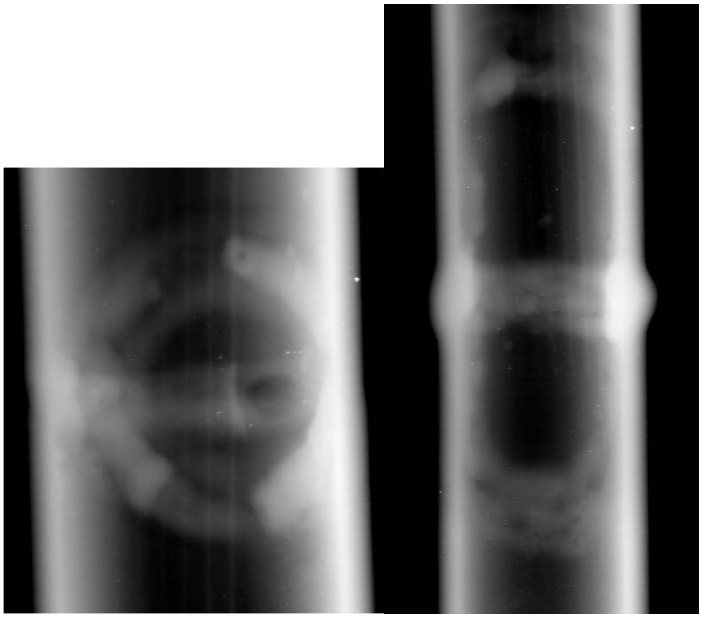

Tube A Tube B

Tube C Tube D

Figure 3.21: Boiler tubes X-ray exam results

Demonstrated in Figure 3.21 are the X-ray exam results for reference. Although the X-ray has the capability of seeing through the metal structure, it requires that the X-ray source and film to be positioned at a specific angle to the crack in order to “capture”

the image and view a potential defect. The X-ray images in Figure 3.21 do not present clear identification of the cracks in the tubes however, after the tubes were destructively examined, it was confirmed that the actual indications of defect areas did show up in the Sonic IR images. In addition, a second round of Sonic IR Imaging Experiments was conducted, in spite of some defects being destroyed by the saw blade cutting process. In the following figures, comparisons between images from first round and second round Sonic IR Imaging experiments are shown. Showed in Figure 3.22, defect 1 was destroyed by cutting; defect 2 remains intact. Shown in Figure 6, defect 1 can no longer be found in the cut-open pieces. However, visible cracks are found at positions of defect 2 and 3 in image Figure 3.23 (a) after the cutting process; Defect 2 and 3 were cut open along the defect for further investigation, the results are shown in Figure 3.24 and Figure 3.25. Shown in Figure 3.26, defect remains intact. Shown in Figure 3.27, defect 1 was destroyed by cut, and defect 2 and 3 remain intact.

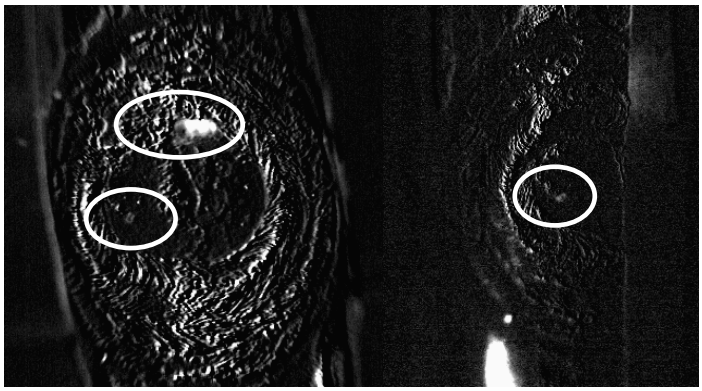

(a) (b)

Figure 3.22: Tube A first round and second round IR image comparison

(a) First round IR Image(b) Second round IR Image

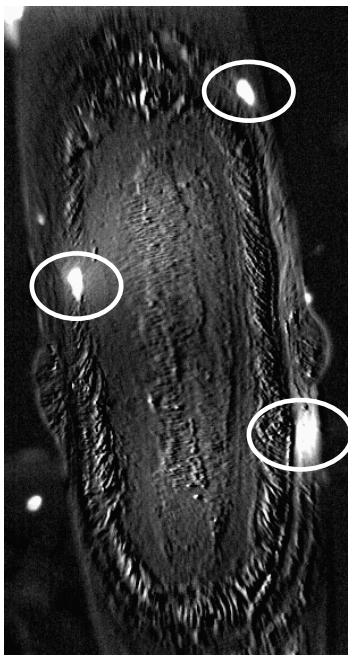

Figure 3.23: Tube B first IR image

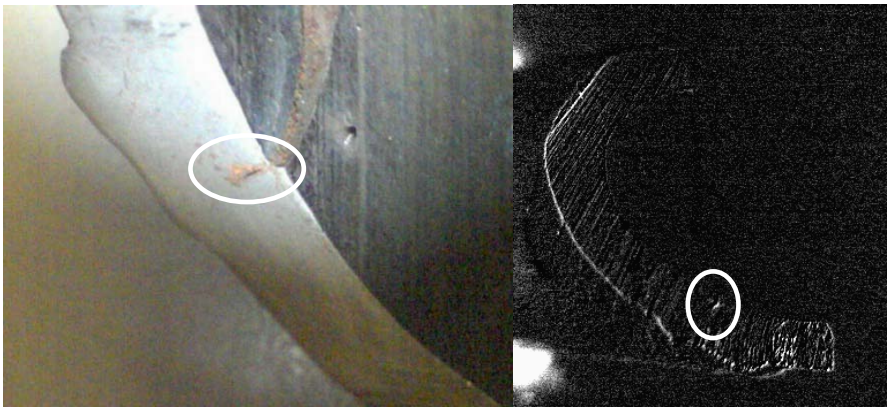

(a) (b)

Figure 3.24: Tube B defect 2 Optical Image and IR Image

(a) Crack optical image with 60X magnification (b) Second round IR Image

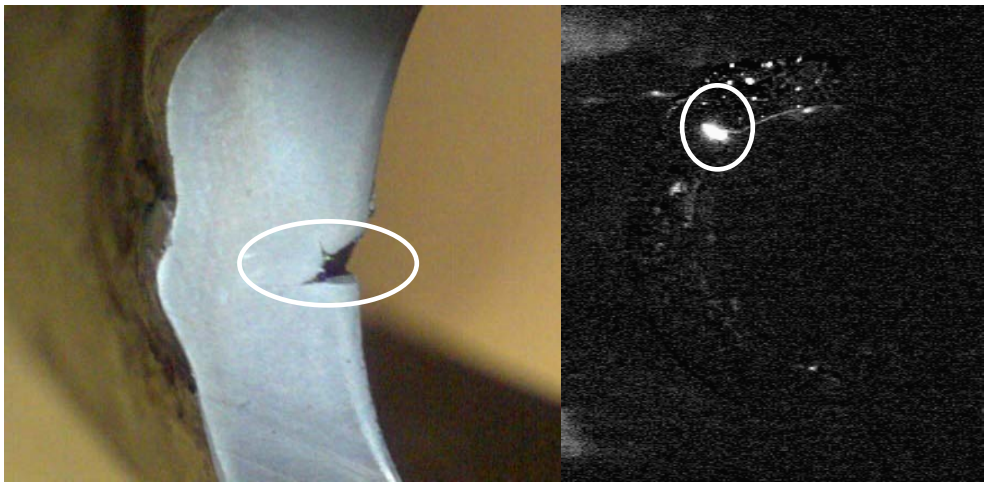

(a) (b)

Figure 3.25 Tube B defect 3 Optical Image and IR Image

(a) Crack optical image with 60X magnification (b) Second round IR Image

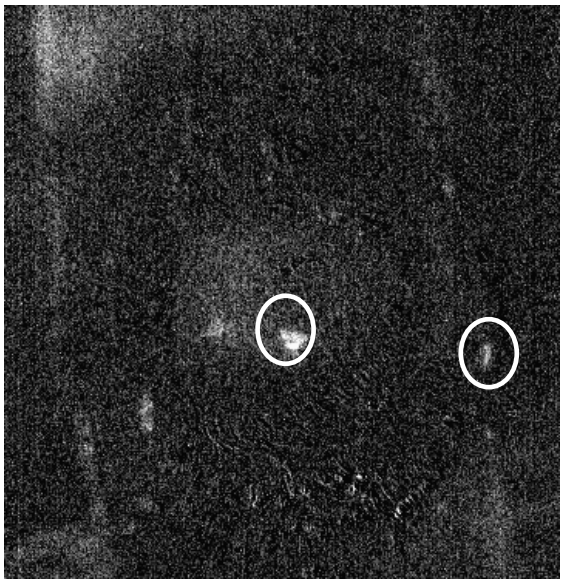

(a)

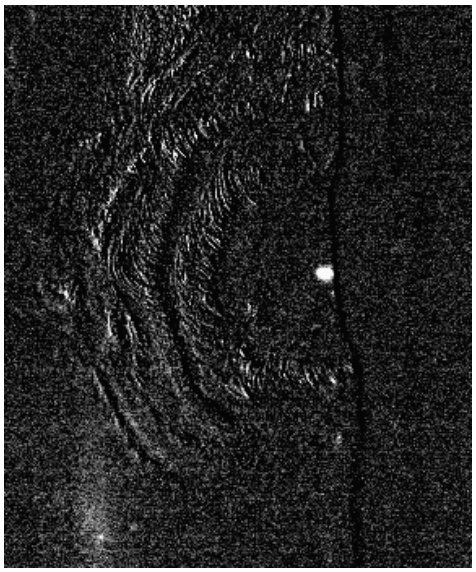

(b)

Figure 3.26: Tube C first round and second round IR image comparison

(a) First round IR Image (b) Second round IR Image

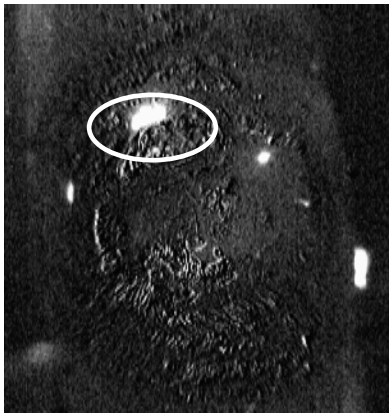

(a)

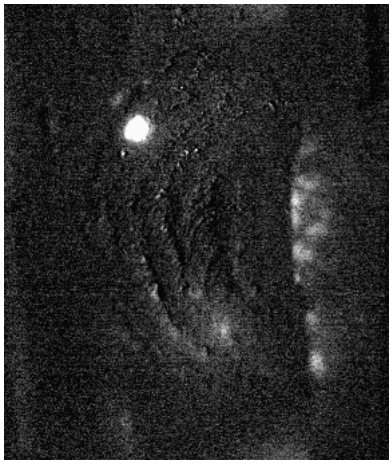

(b)

(c)

Figure 3.27: Tube D first round and second round IR image comparison

(a) First round IR Image (b)Second round IR Image (left half) (c) Second round IR Image (right half)

Sonic IR Imaging technique can successfully detect the defects in the welding joints of the Utility Power Boiler tubes and is further confirmed by the visible defect found in the right half of Tube B.

CHAPTER 4

FINITE ELEMENT ANALYSIS AND RESULTS

4.1 Introduction of Finite Element Analysis:

Finite element Analysis (FEA) is a numerical method for solving problems of engineering and mathematical physics; Finite element Analysis also frequently referred to as the finite element method (FEM). Typical problem areas of interest in engineering and mathematical physics that are solvable by use of the finite element analysis include structure analysis, heat transfer, fluid flow, mass transport, and electromagnetic potential. For problems involving complicated geometries, loadings and material properties, it is general not possible to obtain analytical mathematical solution. Analytical solutions are those given by a mathematical expression that yields the values of the desired unknown quantities at any location in a body and thus are valid for an infinite number of locations in the body. These analytical solutions generally require the solution of ordinary or partial differential equations, which, because of the complicated geometries, loadings, and material properties, are not usually obtainable. These limitation had force us to employ numeric methods for an acceptable solution.

Unlike traditional analytical solutions, FEA uses a numerical technique to minimize variational calculus and obtain approximate solutions. FEA uses a complex system of points called nodes which make a grid called a mesh (Figure 4.1). This mesh is programmed to contain the material and structural properties which define how the structure will react to certain loading conditions. Nodes are assigned at a certain density throughout the material depending on the anticipated stress levels of a particular area.

Regions which will receive large amounts of stress usually have a higher node density than those which experience little or no stress. Points of interest may consist of: fracture point of previously tested material, fillets, corners, complex detail, and high stress areas. The mesh acts like a spider web in that from each node, there extends a mesh element to each of the adjacent nodes. This web of vectors is what carries the material properties to the object, creating many elements.

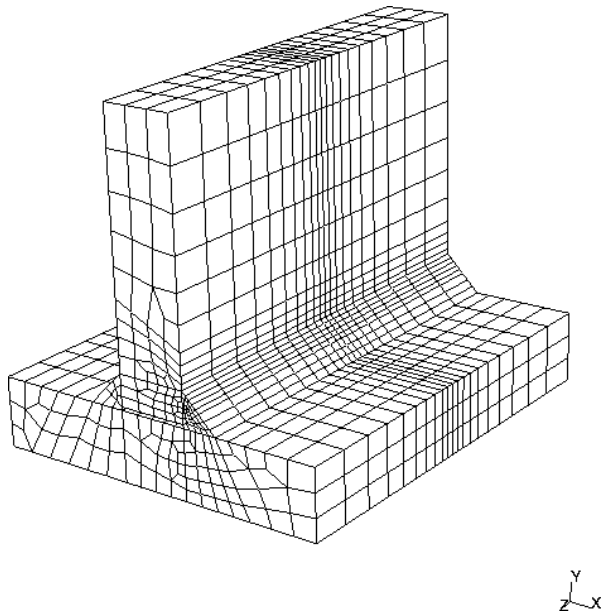

Figure 4.1: Typical FEA Mesh

A wide range of objective functions (variables within the system) are available for minimization or maximization:

- Mass, volume, temperature
- Strain energy, stress strain
- Force, displacement, velocity, acceleration
- Synthetic (User defined)

There are multiple loading conditions which may be applied to a system.

- Point, pressure , thermal, gravity, and centrifugal static loads
- Thermal loads from solution of heat transfer analysis
- Enforced displacements
- Heat flux and convection
- Point, pressure and gravity dynamic loads

Each FEA program may come with an element library, or one is constructed over time. Some sample elements are:

- Rod elements
- Beam elements
- Plate/Shell/Composite elements
- Shear panel
- Solid elements
- Spring elements
- Mass elements
- Rigid elements
- Viscous damping elements

Many FEA programs also are equipped with the capability to use multiple materials within the structure such as:

- Isotropic, identical throughout
- Orthotropic, identical at 90 degrees
- General anisotropic, different throughout

Generally, three steps are applied in a numerical FEA simulation:

- Pre-process or Modeling – building up the finite element model and setting up boundary conditions. Building up a finite element model is the first step in using FEA. The topology and geometry of the structure is been set up in this step, a variety of elements can be used in either 1D, 2D, or 3D form. The primary objective of this step is to realistically replicate the important parameters and features of the real model.

- Solving or Calculation – solution of the finite element model. The second step of the FEA is calculation. The FEM processes a series of calculations based on loads, boundary conditions and material properties which applied to the model. The results such as displacement, stress, strain and temperature are collected in this step.

- Post-processing – display the results. The results collected in step two can be viewed by using post-processing tools which embedded in FEM. Results of specified location can be displayed graphically.

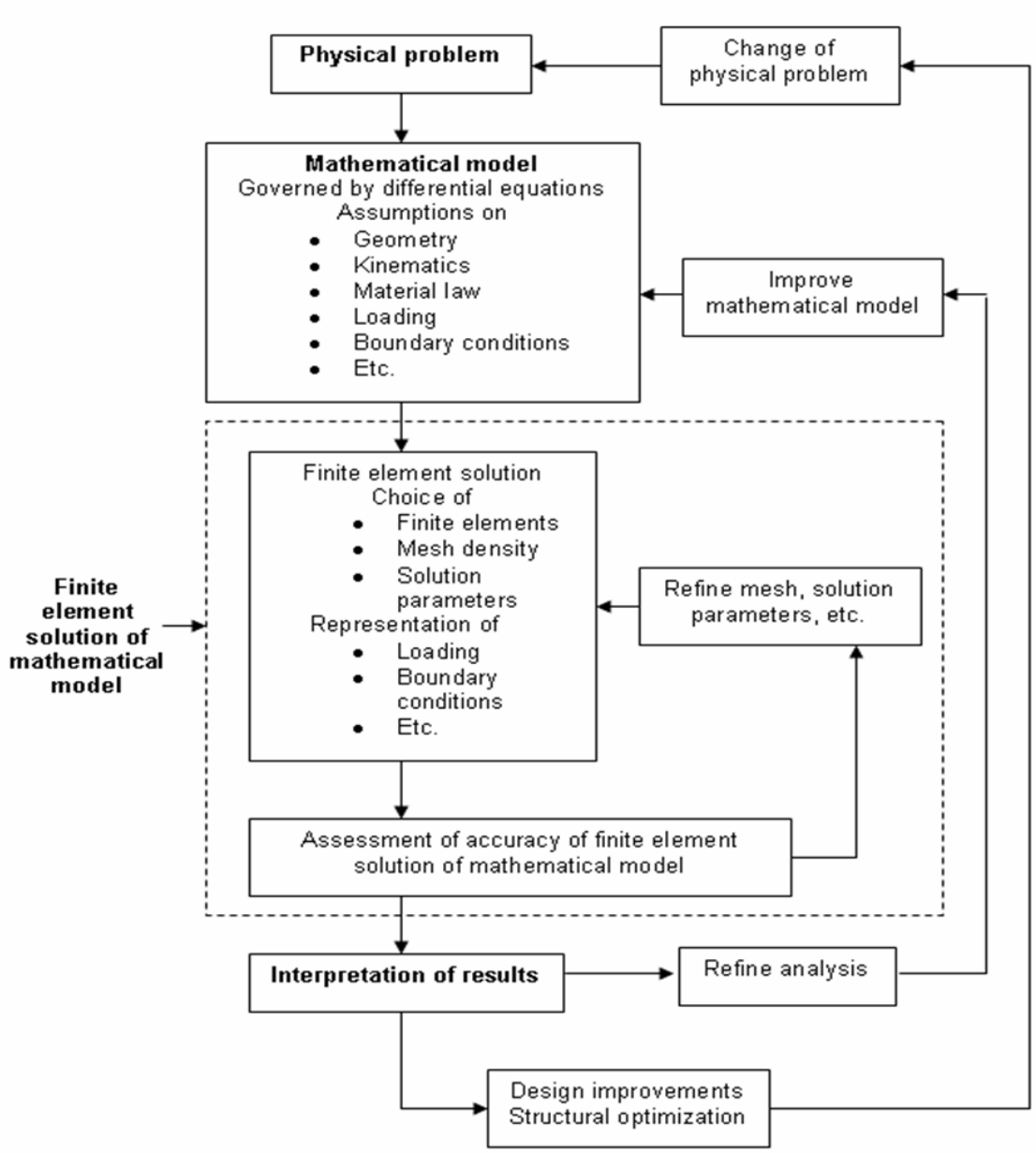

Figure 4.2: The summary of the process of finite element analysis.

4.2 Typical Types of FEA Engineering Analysis

Structural analysis consists of linear and non-linear models. Linear models use simple parameters and assume that the material is not plastically deformed. Non-linear

models consist of stressing the material past its elastic capabilities. The stresses in the material then vary with the amount of deformation.

Vibrational analysis is used to test a material against random vibrations, shock, and impact. Each of these incidences may act on the natural vibrational frequency of the material which, in turn, may cause resonance and subsequent failure.

Fatigue analysis helps designers to predict the life of a material or structure by showing the effects of cyclic loading on the specimen. Such analysis can show the areas where crack propagation is most likely to occur. Failure due to fatigue may also show the damage tolerance of the material.

Heat Transfer analysis models the conductivity or thermal fluid dynamics of the material or structure. This may consist of a steady-state or transient transfer. Steady-state transfer refers to constant thermo properties in the material that yield linear heat diffusion.

FEA has become a solution to the task of predicting failure due to unknown stresses by showing problem areas in a material and allowing designers to see all of the theoretical stresses within. This method of product design and testing is far superior to the manufacturing costs which would accrue if each sample was actually built and tested.

4.3 FEA Tools and Basic Physics Concepts

There are several FEA tools available in the market. The most common ones are Ls-Dyna, Abacus. LS-DYNA is an advanced general-purpose multiphysics simulation

software package that is actively developed by the Livermore Software Technology Corporation (LSTC). While the package continues to contain more and more possibilities for the calculation of many complex, real world problems, its origins and core-competency lie in highly nonlinear transient dynamic finite element analysis (FEA) using explicit time integration. LS-DYNA is being used by the automobile, aerospace, construction, military, manufacturing, and bioengineering industries.

During this research LS-Dyna is employed to perform all the numerical analysis work. In the following chapters, some basic physics and mechanical concepts incorporated in LS-Dyna will be listed for future reference.

4.3.1 Dynamic Equations, Mass and Damping Matrices in LS-Dyna

Figure 4.2 shows a single degree of freedom damped system, and Figure 4.3 shows forces acting on mass, m.

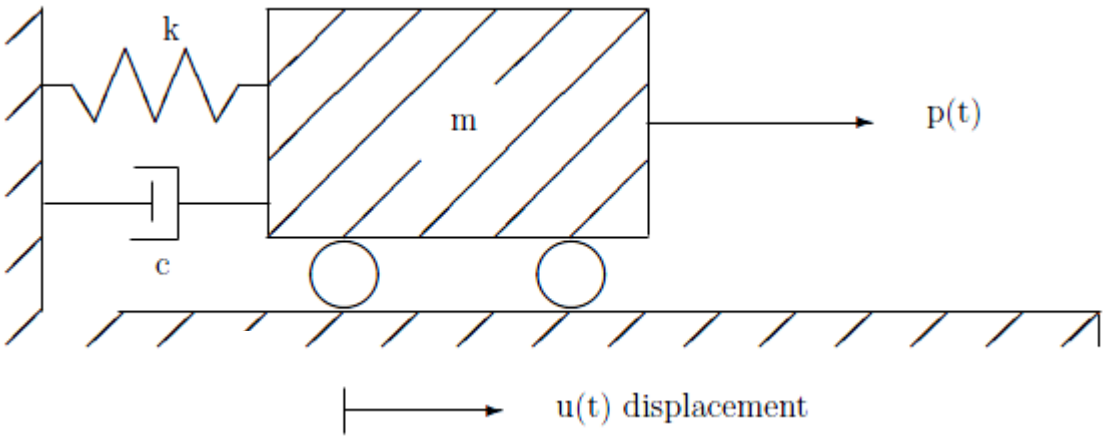

Figure 4.3: Single degree of freedom damped system.

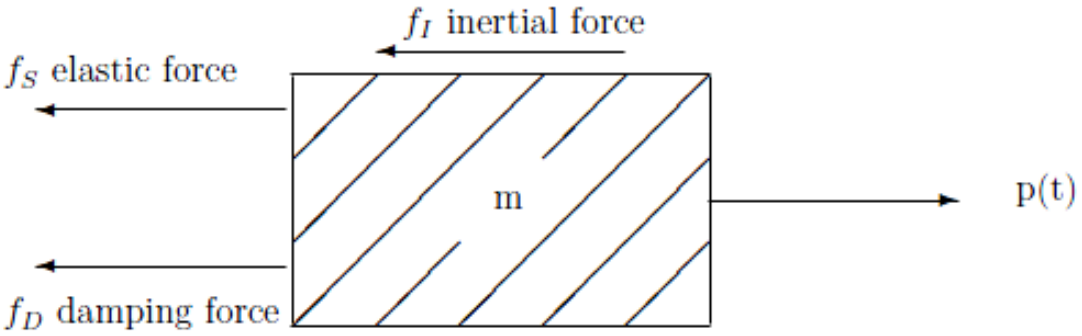

Figure 4.4: Forces acting on mass, m.

The equilibrium equations from d'Alemberts's principle

$$f_I + f_d + f_{\text{int}} = p(t) \qquad \text{..... (4.1)}$$

$$f_1 = m\ddot{u}; \quad \ddot{u} = \frac{d^2u}{dt^2} \qquad \text{..... (4.2)}$$

$$f_D = c\dot{u}; \quad \dot{u} = \frac{du}{dt} \qquad \text{..... (4.3)}$$

$$f_{\text{int}} = k.u; \quad u \qquad \text{..... (4.4)}$$

where

u = displacement,

c = damping coefficient,

m = the mass

k = linear stiffness.

$$m\ddot{u} + c\dot{u} + ku = p(t) \qquad \text{..... (4.5)}$$

For critical damping $c=c_{cr}$. The equations of motion for linear behavior lead to a linear ordinary differential equation (o.d.e),

For nonlinear case the internal force varies as a nonlinear function of the displacement, leading to a nonlinear o.d.e:

$$m\ddot{u} + c\dot{u} + f_{\text{int}}(u) = p(t) \qquad \text{..... (4.6)}$$

4.3.2 Dynamic Nonlinear Process in LS-Dyna:

The solution of the nonlinear dynamic response of a finite element system is obtained by using the procedures like the incremental formulations, the iterative solution procedures and the time integration algorithms. LS-DYNA uses the explicit central difference method to integrate the equations of motion.

The semi-discrete equations of motion at time t are:

$$ma^n = P^n - F^n + H^n \qquad \text{..... (4.7)}$$

Where m is the diagonal mass matrix, P^n accounts for external and body force loads, F^n is the stress divergence vector and H^n is the hourglass resistance. To advance to time t^{n+1} the central difference time integration is used:

$$a^n = m^{-1}\left(P^n - F^n + H^n\right)$$

$$v^{n+1/2} = v^{n-1/2} + a^n \Delta t^n$$

$$u^{n+1} = u^n + v^{n+\frac{1}{2}} \Delta t^{n+\frac{1}{2}} \qquad \text{..... (4.8)}$$

where

$$\Delta t^{n+1/2} = \frac{\left(\Delta t^{n} + \Delta t^{n+1/2}\right)}{2} \qquad \text{..... (4.9)}$$

v and u are the global nodal velocity and displacement vectors, respectively. The geometry is updated by adding the displacement increments to the initial geometry[13].

$$x^{n+1} = x^{0} + u^{n+1} \qquad \text{..... (4.10)}$$

4.3.3 Equations of Frictional Force

Friction in LS-DYNA is based on a Coulomb formulation. Let f^{*} be the trial force, f_n the frictional force at time n, the frictional algorithm, outlined below, uses the equivalent of an elastic plastic spring. [13] The steps are as follows:

1. Compute the yield force, F_y:

$$F_y = \mu \left| f_n \right| \qquad \text{..... (4.11)}$$

2. Compute the incremental movement of slave node:

$$\Delta e = \mathrm{r}^{n+1}\left(\xi_c^{n+1}, \eta_c^{n+1}\right) \quad -\mathrm{r}^{n+1}\left(\xi_c^{n}, \eta_c^{n}\right) \qquad \text{..... (4.12)}$$

3. Update the interface force to a trial value:

$$f^{*} = f^{n} - k\Delta e \qquad \text{..... (4.13)}$$

4. Check the yield condition:

$$f^{n+1} = f^{*} \qquad if \left| f^{*} \right| \le F_y \qquad \text{..... (4.14)}$$

5. Scale the trial force if it is too large:

$$f^{n+1} = \frac{F_y f^{*}}{\left| f^{*} \right|} \quad \text{if } \left| f^{*} \right| > F_y \qquad \text{..... (4.15)}$$

An exponential interpolation function smooth the transition between the static, μ_s and dynamic, μ_d, coefficient of friction where v is the relative velocity between the slave node and the master segment:

$$\mu = \mu_d + \left(\mu_s - \mu_d \right) \; e^{-c|v|} \qquad \text{..... (4.16)}$$

Where

$$v = \frac{\Delta e}{\Delta t} \qquad \text{..... (4.17)}$$

Δt is the time step size, and c is the decay constant.

The interface shear stress that develops as a result of Coulomb friction can be very large and in some cases may exceed the ability of the material to carry such

a stress, we therefore allow another limit to be placed on the value of the tangential force:

$$f^{n+1} = \min\left(f_{Coulomb}^{n+1}, \kappa A_{master}\right) \quad \text{…….} (4.18)$$

Where A_{master} is the area of the master segment and k is is the viscous coefficient. Since more than one node may contribute to shear stress of a segment , we recognize that the stress may still in some case exceed the limit k.

4.3.4 Heat Transfer

LS-DYNA can be used to solve for the steady state or transient temperature field on three-dimensional geometries. Material properties may be temperature dependent and either isotropic or orthotropic. A variety of time and temperature dependent boundary conditions can be specified including temperature, flux convection, and radiation. The implementation of heat conduction into LS-DYNA is based on the work of Shapiro[1985].[13]

Conduction of Heat in Orthotropic Solid Materials

The differential equation of conduction of heat in a three-dimensional continuum is given by:

$$\rho c_p \frac{\partial \theta}{\partial t} = \left(k_{ij}\theta_{,j}\right)_{,i} + Q, \qquad \ldots\ldots\ldots (4.19)$$

Subject to the boundary conditions

$$\theta = \theta_s \qquad \text{on } \Gamma_1$$

$$k_{ij}\theta_{,j}n_i + \beta\theta = \gamma \quad \text{on } \Gamma_2 \qquad \ldots\ldots\ldots (4.20)$$

And initial conditions at t_0 :

$$\theta_\Gamma = \theta_0(x_i) \text{ at } t=t_0 .$$

Where

$\theta = \theta\left(x_i, t\right)$ ……temperature

$x_i = x_i\left(t\right)$ …… coordinates as function time

$\rho = \rho\left(x_i\right)$ …… density

$c_p = c_p\left(x_i, \theta\right)$ …… specific heat

$Q = Q\left(x_i, \theta\right)$ …… internal heat generation rate per unit Ω

$k_{ij} = k_{ij}\left(x_i, \theta\right)$ ……..…..... thermal conductivity

θ_Γ ……prescribed temperature on Γ_1

n_i ……normal vector to Γ_2

These equations above represent the strong form of a boundary value problem to be solved for the temperature field within the solid.

The finite element method provides the following equations for the numerical solutions of equations

$$\left[\frac{C_{n+\alpha}}{\Delta t}+\alpha H_{n+\alpha}\right]\{\theta_{n+1}-\theta_n\}=\{F_{n+\alpha}-H_{n+\alpha}\theta_n\} \quad \ldots\ldots (4.21)$$

Where

$$[C]=\sum_e\left[C_{ij}^e\right]=\sum_e\int_{\Omega^e} N_i\ \rho c\ N_j d\Omega \quad \ldots\ldots (4.22)$$

$$[H]=\sum_e\left[H_{ij}^e\right]=\sum_e\left[\int_{\Omega^e}\nabla^T N_i K\nabla N_j d\Omega+\int_{\Gamma^e} N_i\beta N_j d\Gamma\right] \quad \ldots\ldots (4.23)$$

$$[F]=\sum_e\left[F_i^e\right]=\sum_e\left[\int_{\Omega^e} N_i q_g d\Omega+\int_{\Gamma^e} N_i\gamma d\Gamma\right] \quad \ldots\ldots (4.24)$$

The parameter α is taken to be in the interval [0,1]. Some well know members of this α - family are:

α	method
0	forward difference; forward Euler
1/2	midpoint rule; Crank-Nicolson
2/3	Galerkin
1	backward difference, fully implicit

4.4 Reason for Finite Element Simulation

In Sonic IR imaging technology, it is pretty straightforward that the heat generated along the crack is caused by the frication of the two surfaces of the crack. The vibration of the crack takes a leading role in the process of the heat generation. Some previous study conducted reveled that in small parts made by softer material like aluminum. However there is not a clear answer to the question of how the vibration really effect the heat generation in large size structures like beams and channels? The vibration contains several key components. Among these key properties, the vibration frequency and vibration amplitude are two most important properties we would like to study. It is important to know that which properties effect the heat generation in larger civil structures. By answering this specific question, we can lay a solid ground for the application of the Sonic IR NDE technology in civil engineering applications.

In order to study the effect caused solely by the frequency, we need to keep the input energy the sample for all the frequencies. However the nature of the ultrasound equipment we possessed had limited our ability to do that. As an alternative, FEA has provided the exactly right tool for us to break the limitation and conduct the research. Furthermore, FEA also granted us the ability to change one or several aspects of the sample material property to see their effects on Sonic IR imaging, which is impossible to do in real experiment. In the following part, I will present the process and result of the FEA simulation we had done for this study.

4.4.1 of Bolt/Rivet-Hole Crack

Based on the sample which was used in the experiment, a FEA model was built to simulate the bolt/rivet-hole crack. The sample used in experiment has a complicate

geometry. While building the FEA model, the geometry of the sample had been simplified. As shown in Figure 4.6, the FEA was built as a long plate with dimensions of 500mm x 100mm x 4mm. A hole with diameter of 10mm was place in the left half of the plate 50mm away from the left end. Shown in lower picture in Figure 4.6, a crack was place on the edge of the hole.

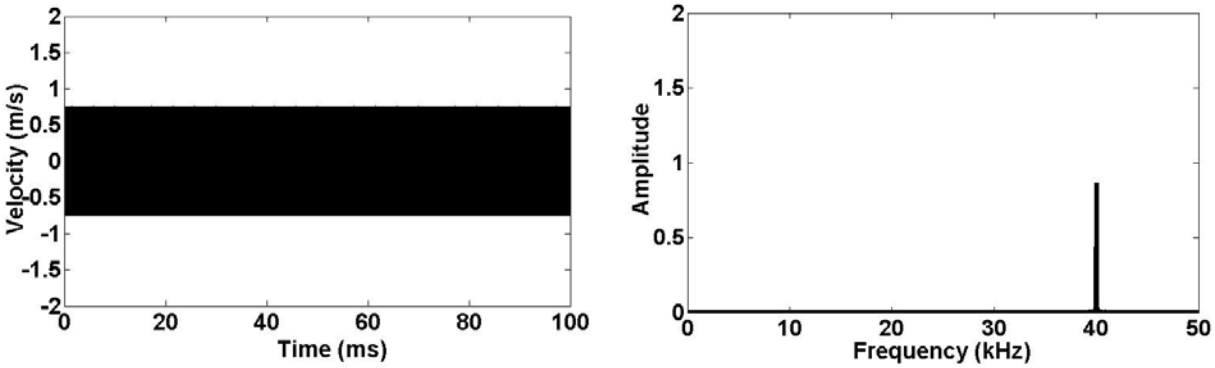

Figure 4.5: 40 kHz Input Signal

To save calculation time, a 40 kHz sinusoidal wave with length of 100ms was used as input excitation source. The total simulation time was set at 200ms, so we can observe both heating and cooling process at the crack region. Material properties for aluminum alloy used in simulation are listed in table 4.1.

Density	2.70e+03 kg/m
Elastic Modulus	7e+10 Pa
Thermal Conductivity	237 W/m C
Heat Capacity	890 J/kg C
Flux	1 W/ m2
Mechanical Equivalent of heat	1 J/Nm

Table 3: Material and Thermal Properties of Aluminum Alloy

In the simulation one end of the plate was fixed and the transducer is placed at the far end to the hole and crack (show in Figure 4.6).

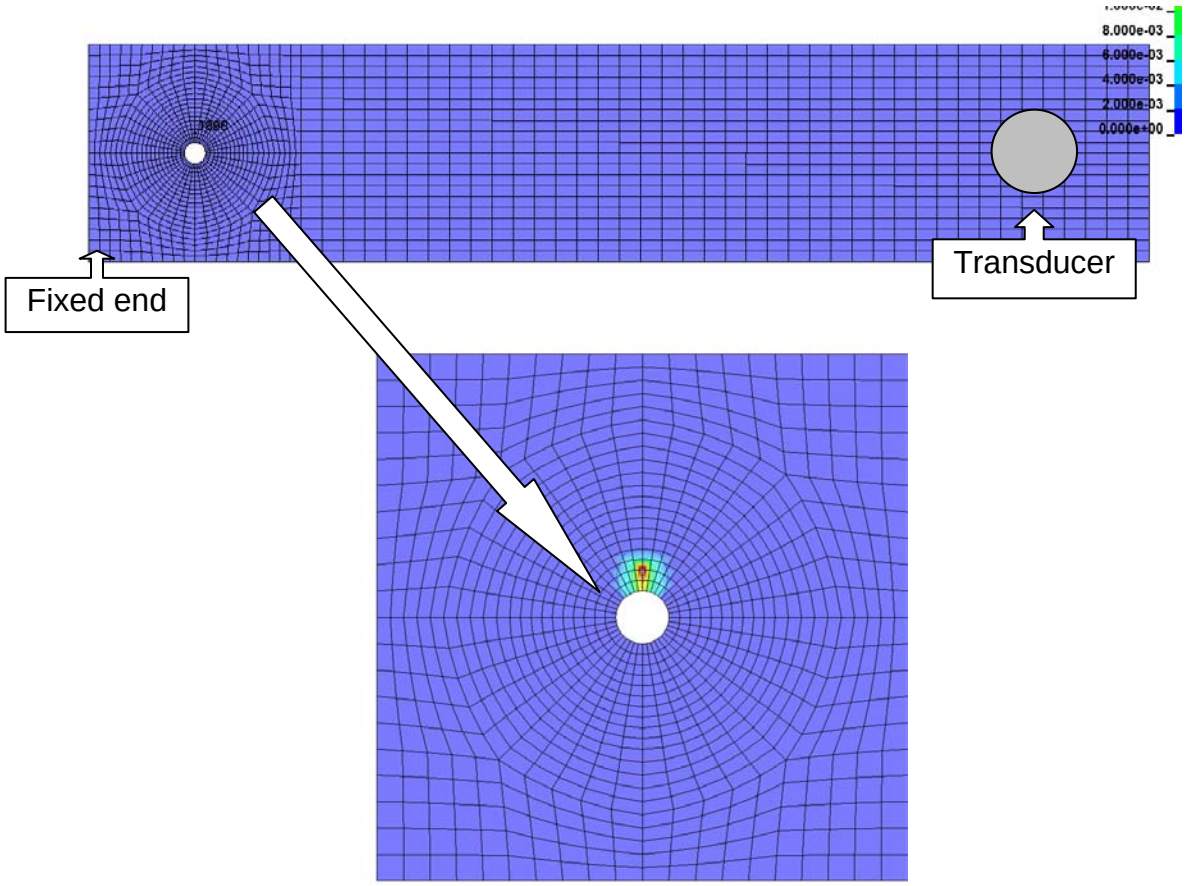

Figure 4.6: Finite Element Model of Rivet Hole

In Figure 4.7 both Time-Temperature plots from simulation and experiment are shown. Although the temperature increase after 100ms excitation time is 0.044 degree Celsius which is lower than the 0.15 degree Celsius in experiment, we can find that the heating and cooling process are very similar which can tell us that the FEA model is has the same response to the excitation as the sample in real experiment. Because material properties were arbitrarily chosen, the difference in the temperature rise could be caused by the material properties we chosen for the model. We consider this FEA model is accurate and working.

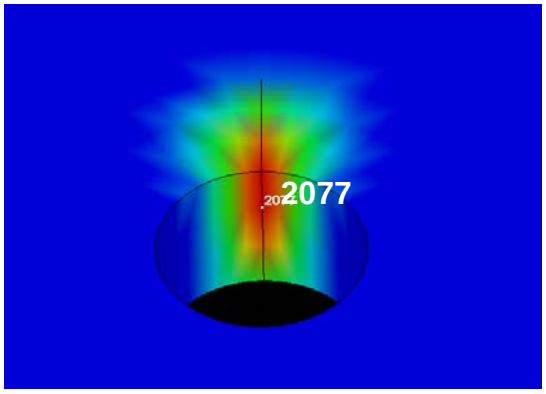

(a) Position of node 2077

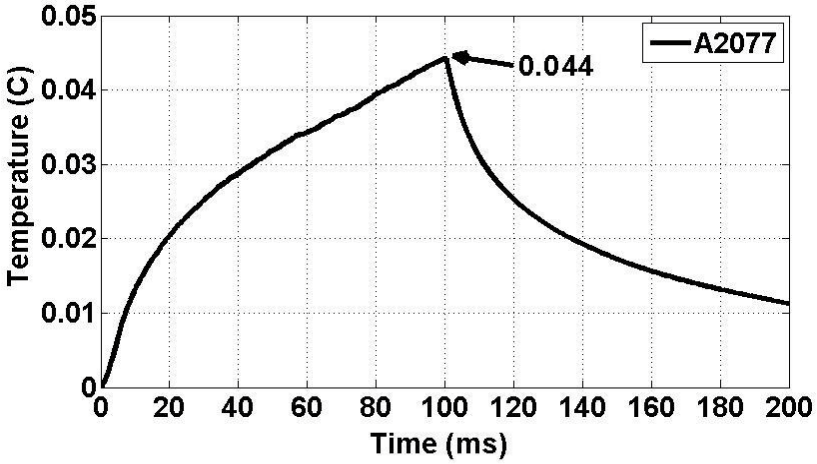

(b) Node 2077 Simulation Time-Temperature Plot

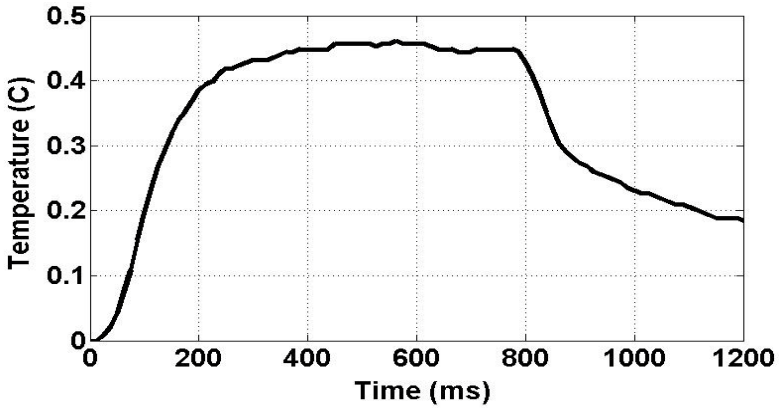

(c) Experiment Time-Temperature plot

Figure 4.7: Time-Temperature (t-T) of Node 2077 on the crack

(Camera delay time in experiment Time –Temperature plot has been removed)

4.4.2 Welding Joint Crack

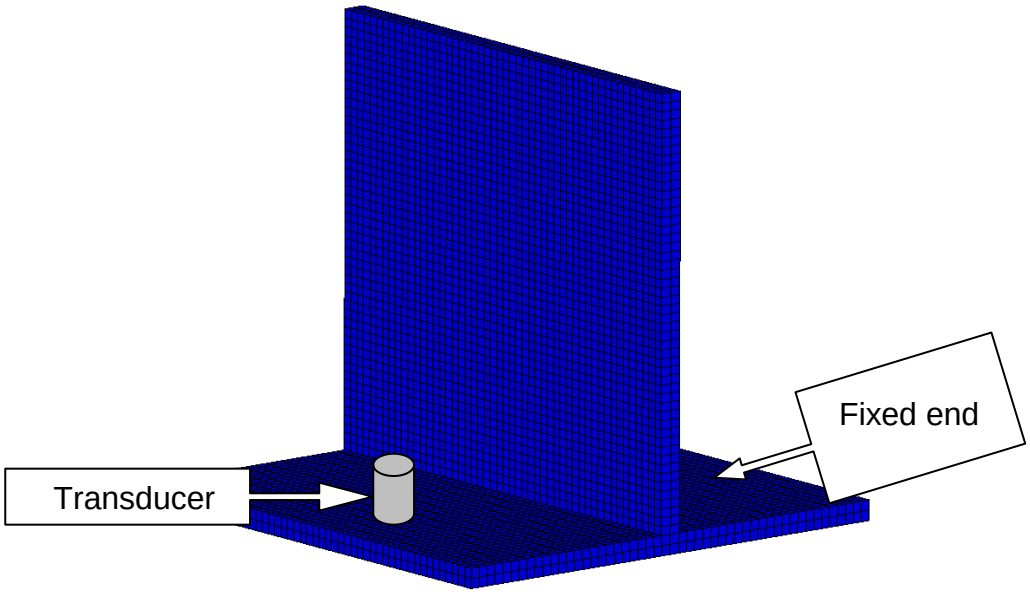

Figure 4.8: FEA model used for welding crack study

Following the real experiment, a FEA model was built for the welding joint crack study. The physical dimension of the model is exactly following the sample used in the real experiment. The aluminum alloy material properties used are list in table 3.

In this study, we did separate simulation for 2 different scenarios. One is the crack at the center of the welding joint; the other one, the crack is on the edge of the welding joint. As observed in experiment, after 300ms, the heat generation reaches a relative stable state and no big temperature increase occurred along the crack. To simplify the simulation, a 40 kHz sinusoidal ultrasound wave with length of 400 ms was used as the input excitation source for both center crack case and edge crack case. Transducer position and fixed end is demonstrated in Figure 4.8, where one end of the sample is fixed and transducer is place at the other end of the base. In the following part, we show the results from the simulation and compare them with the result from the experiment.

In the center crack case as shown in Figure 4.9 (b), the heating up processes in the whole 1 second period after the 800 ms ultrasound wave was input into the sample are very similar. The heating and cooling process of both simulation and experiment have the same pattern.

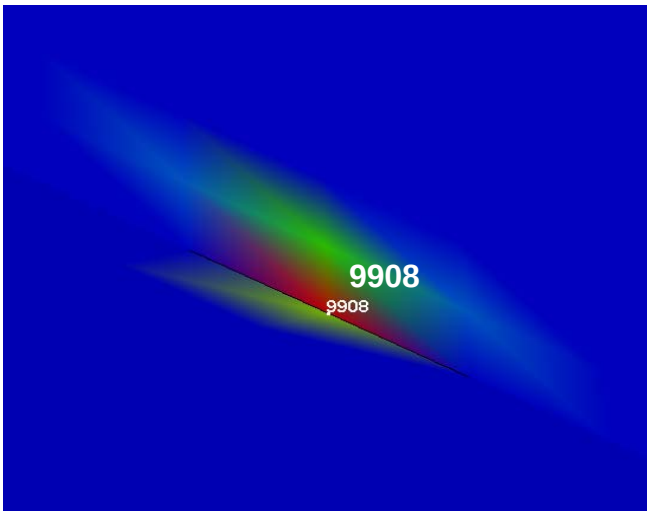

(a) Position of node 9908

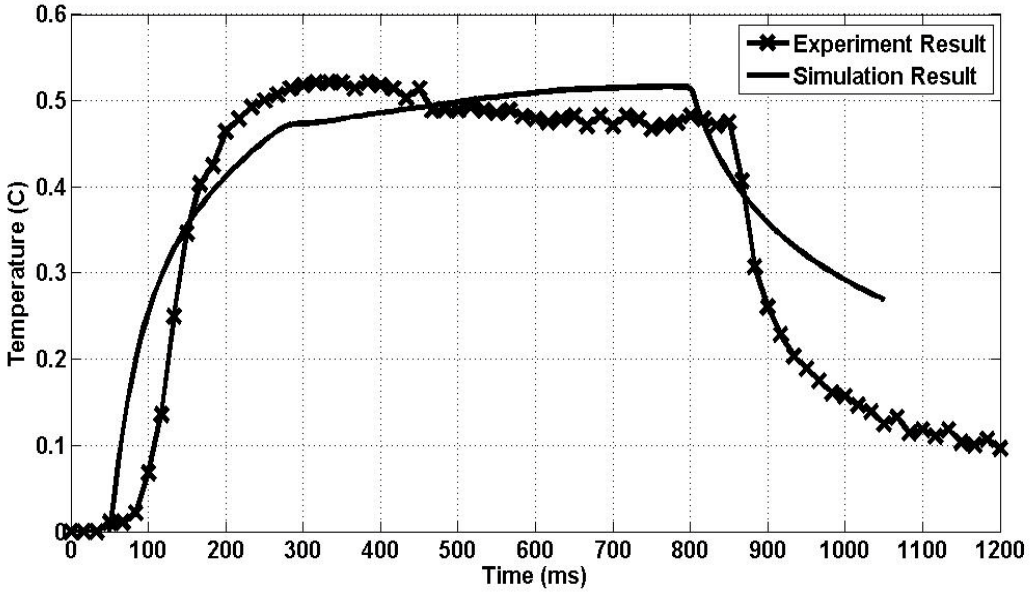

(b) Node 9908 Simulation Time-Temperature Plot

Figure 4.9: Time -Temperature of center crack

(Camera delay time in experiment Time –Temperature plot has been removed)

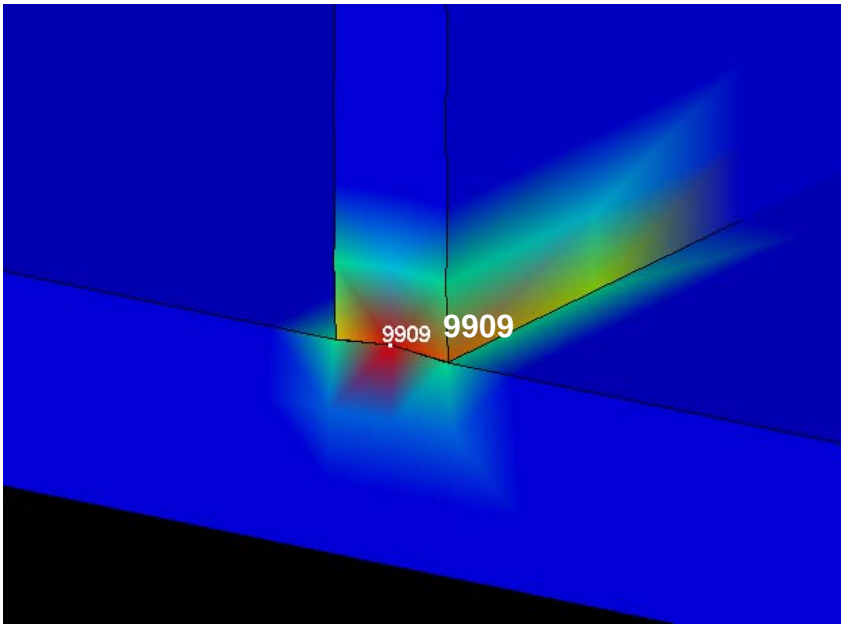

(a) Position of node 9909

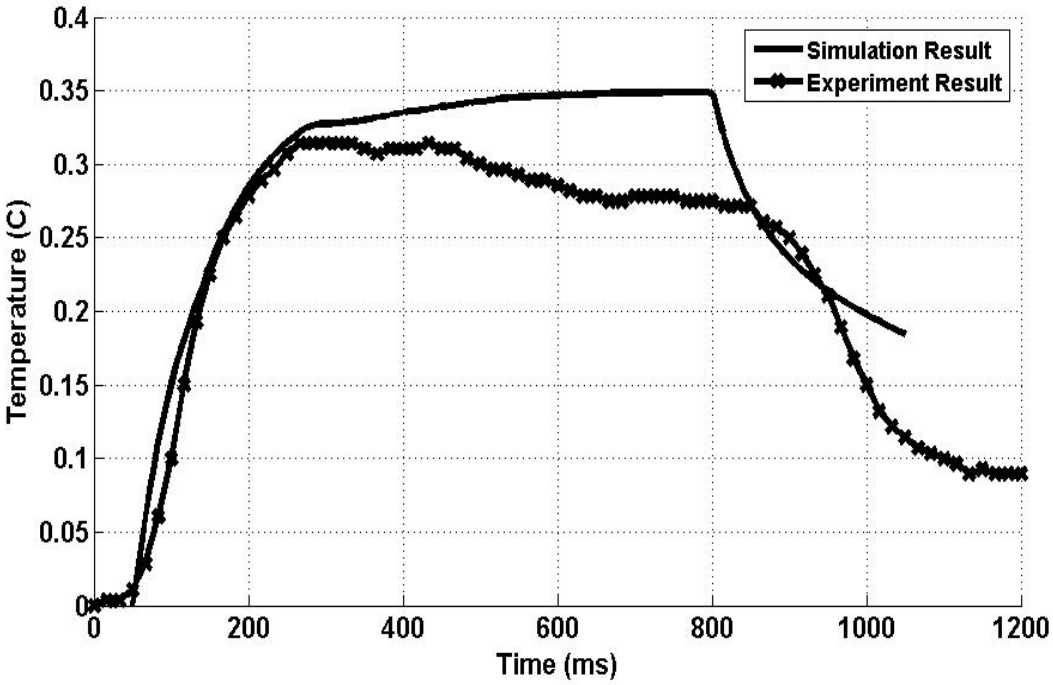

(b) Node 9909 Simulation Time-Temperature Plot

Figure 4.10: Time-Temperature of edge crack

(Camera delay time in experiment Time –Temperature plot has been removed)

The same experiment was also done for the edge crack case, which is shown in Figure 4.10 (b). Because the location is on the edge, only one end of the crack is constrained. The crack is much easier to vibrate after the ultrasound was put in. After comparing the two temperature-time cures in Figure 4.10 (b), we can see these 2 results are also fairly close. The heating processes of both simulation and experiment results have the same pattern.

By comparing the results from both simulation and experiment, we have the confidence that the FEA model built for the welding joint crack is an accurate numerical model of the experiment and can be used for further study in the application of Sonic IR Imaging technology in detecting welding joints cracks.

4.4.3 Girder/Beam Structure (C-Channel)

i) Creating a finite element base model

In Figure 4.11, it shows the finite element model we built for the C-channel, which has a crack on one end of the C-channel and the excitation point on the other end.

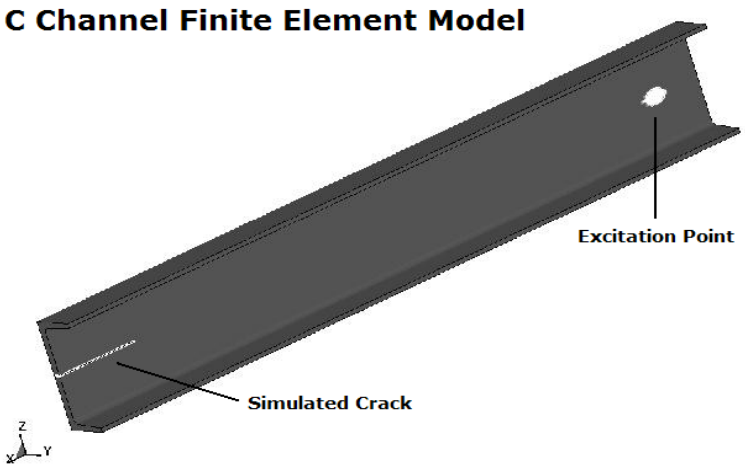

Figure 4.11: C-channel Finite Element Model

Without the specific material and properties of the steel C-channel in hand, the general steel material and thermal properties were used in the simulation. Following in table 4 are the material properties used in the finite element method simulation. All units listed in the table are using international system of units (SI).

Density	7.87e+03 kg/m
Elastic Modulus	2.05e+11 Pa
Thermal Conductivity	51.9 W/m C
Heat Capacity	486 J/kg C
Flux	1 W/ m2
Mechanical Equivalent of heat	1 J/Nm

Table 4: Material and Thermal Properties of Steel

In this simulation, we were trying to create a scenario as close to the experiment as possible. With the help of the laser vibrometer, we recorded the vibration generated by the 15 kHz ultrasonic transducer and used this 15 kHz signal as input for the finite element model we have created for the C-channel.

From Figure 4.12 (b), we can find out the major frequency components in this input signal are 15 kHz and 30 kHz. Although there are some minor frequencies beyond 100 kHz, they are low enough to be ignored.

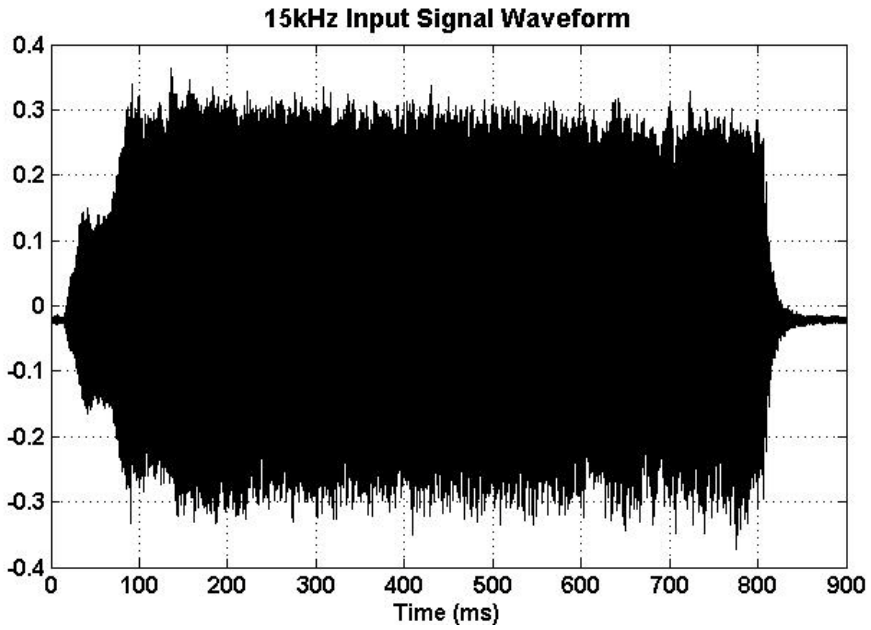

(a)

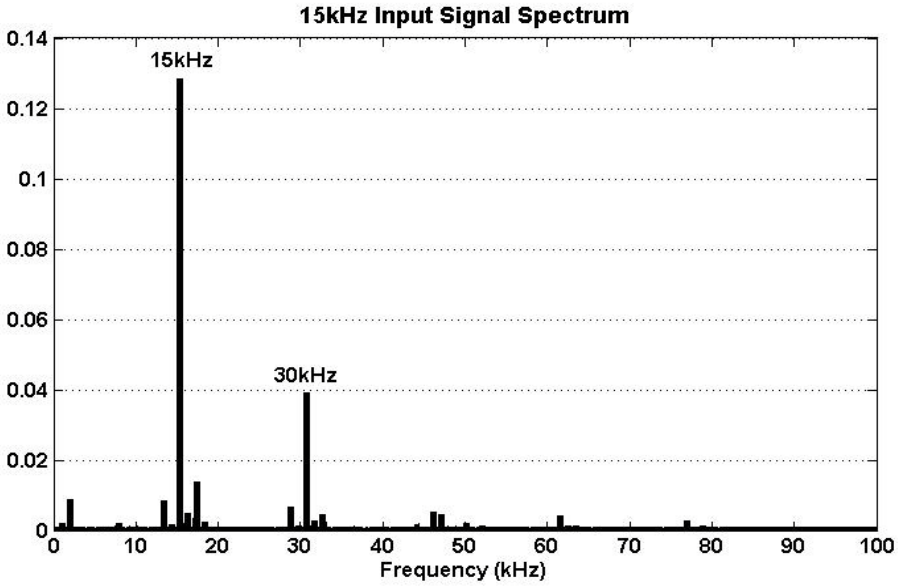

(b)

Figure 4.12: C-channel Finite Element Model Excitation Source

(a)Input signal waveform (b) Input signal spectrum

In Figure 4.12, the time-temperature change of the point with highest temperature in the simulation is plotted. With the finite element simulation result, we can see much finer temperature change from the time-temperature plot showed in Figure 4.13. In the first 100ms, temperature increased dramatically, the plot is going at a roughly 45 degree angle. After the first 100ms, temperature change slowed and entered the linear increase stage, at 550ms, it slowed down again. At 800ms, after the excitation source is gone, the temperature dropped quickly.

ii) Experiment and Simulation Comparison and analysis

In experimental Time-Temperature plot, the data correspond to X, Y axis are frame sequence number and grey scales; in the simulation data, they are actually time and temperatures. For purpose of an easy comparison, the frame sequence number and grey scales were converted in to time in millisecond (ms) and degree Celsius (C) which were used in the simulation result, and the experiment result is scaled with a factor of 0.1.

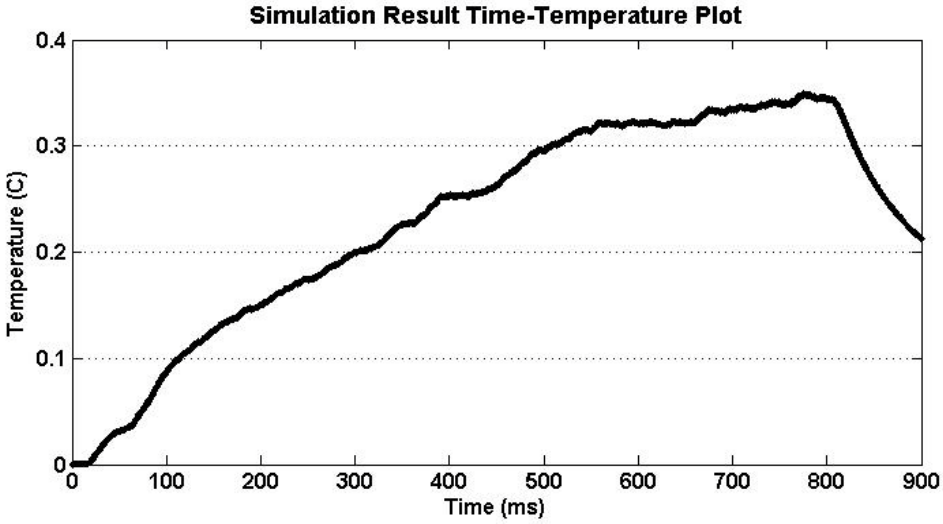

Figure 4.13: Time-Temperature Plot of the highest point in the simulation

2

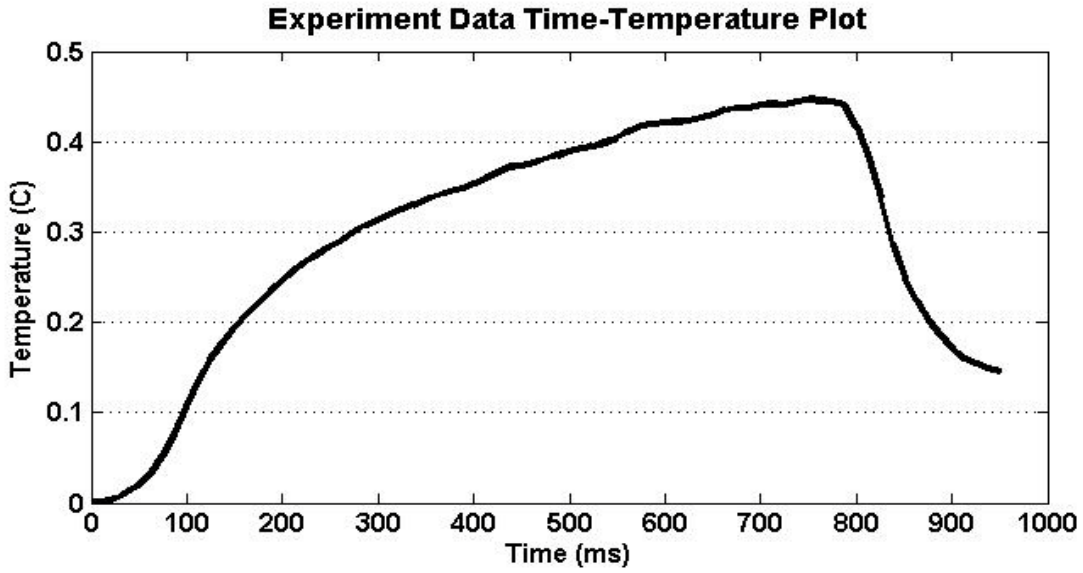

Figure 4.14: Time-Temperature Plot of the highest point in the image sequence (Camera delay time in experiment Time –Temperature plot has been removed)

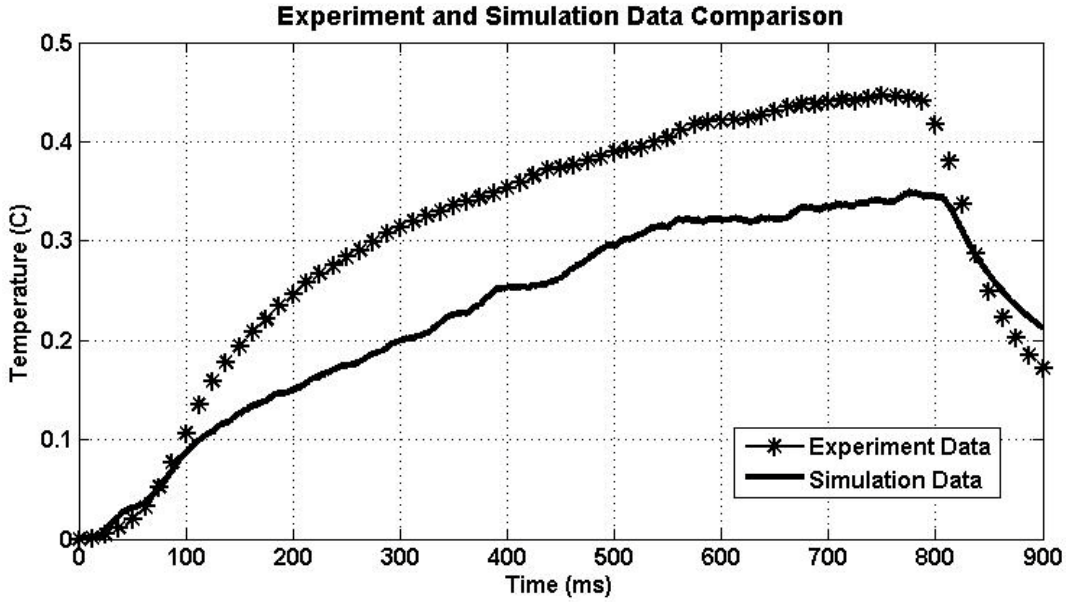

Figure 4.15: Time-Temperature Plot Comparison

From the above comparison, we can find that thought the simulation result showed some difference from the experiment result, from the big picture they were showing the same heating trend. At the first stage after the ultrasound is infused, the temperature increase quickly, then it enters a plateau stage, followed by a temperature plague after the ultrasound excitation ends. From the comparison, we can say that the simulation result is confirmed by the experiment result. From this comparison, we have gained enough confidence to use this FEA model as the base models to conduct further simulation research on this C-Channel Sample.

4.5 Comparison of heat generation from different ultrasound frequency inputs.

The C-Channel used in experiment was chosen to be the base of the study. Following the exact size and material properties, a finite element model was built and calculation result was compared to the experiment to confirm that the FEA model is working the way it should be.

4.5.1 Simulation process and result

With the tested C-Channel FEA model built, the study of the relationship between heat generation and vibration properties had set its feet on solid ground. Next step is to build a practical schema and test different vibrations. From the experience of numbers experiments we have conducted, we selected four (4) different input frequencies, which are 10 kHz, 20 kHz, 30 kHz, and 40 kHz. These selected frequencies components are very common in the spectra obtained from real experiments. We choose 100ms of duration for the excitation pulse for the four frequencies. The reason of choosing 100ms

excitation length is to reduce computation time. At the lowest frequency 10 kHz, 100ms will contain 1000 vibration cycles. From the data gathered from experiments, we are confident to believe that this 1000 vibration is enough to reveal the relation between heat generation and different frequency properties.

An important requirement is keeping input energy of all excitation inputs at the same level. In this case we can assure that the changes of heat generation are caused by different vibration properties, not excessive energy input.

The energy of an input pulse can be expressed as:

$$E = \frac{1}{2} \times A^2 \times 2\pi f \ ,$$

where E is energy, A is the amplitude of an input pulse, f is vibration frequency.

In order to achieve the same input energy requirement, the amplitudes of the four input pulses were adjusted. Four waveforms are displayed in Figure 4.16.

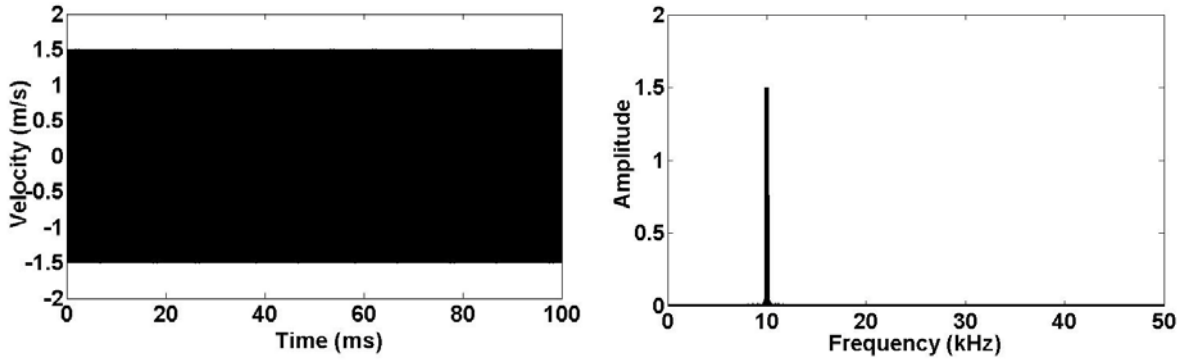

10 kHz Input Source

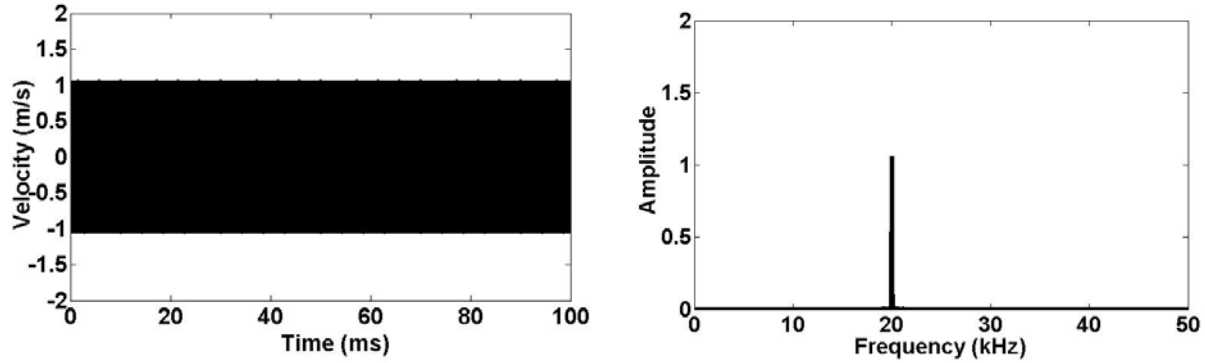

20 kHz Input Source

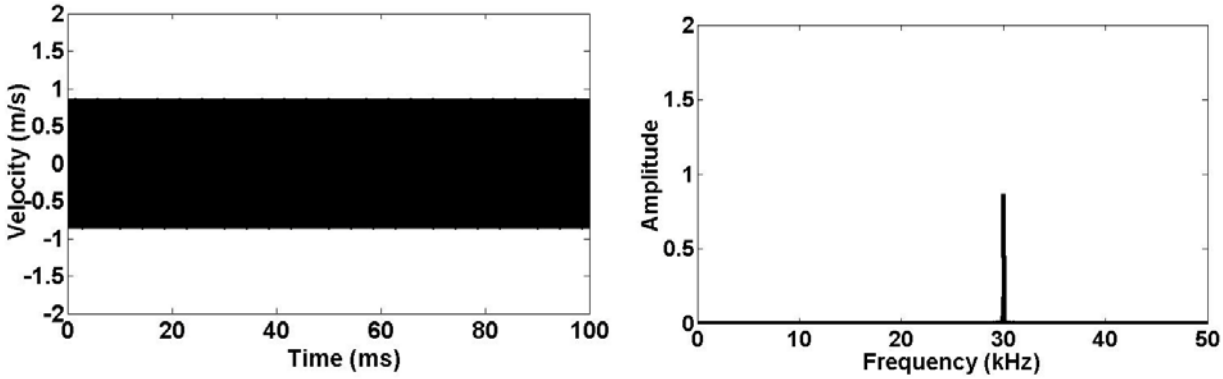

30 kHz Input Source

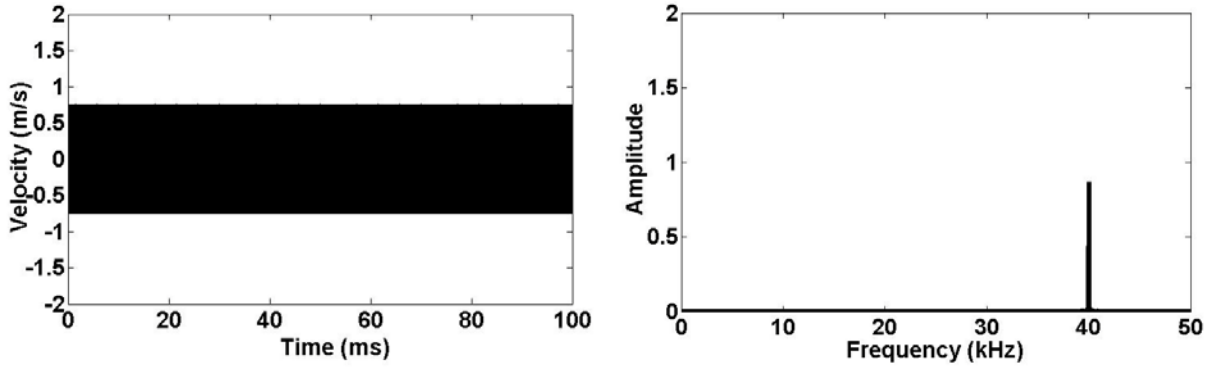

40 kHz Input Source

Figure 4.16: Four different input frequencies used in the FEA simulation.

To make the power of the four input pulses the same, the amplitude of 10kHz input is set to be 1.5, the amplitude of 20 KHz is set to be $1.5*\sqrt{1/2}=1.0607$, the amplitude of 30kHz is set to be $1.5*\sqrt{1/3}=0.866$, and the amplitude of 40kHz is set to be $1.5*\sqrt{1/4}=0.75$. The amplitude comparison of all four input frequencies is showed in Figure 4.17.

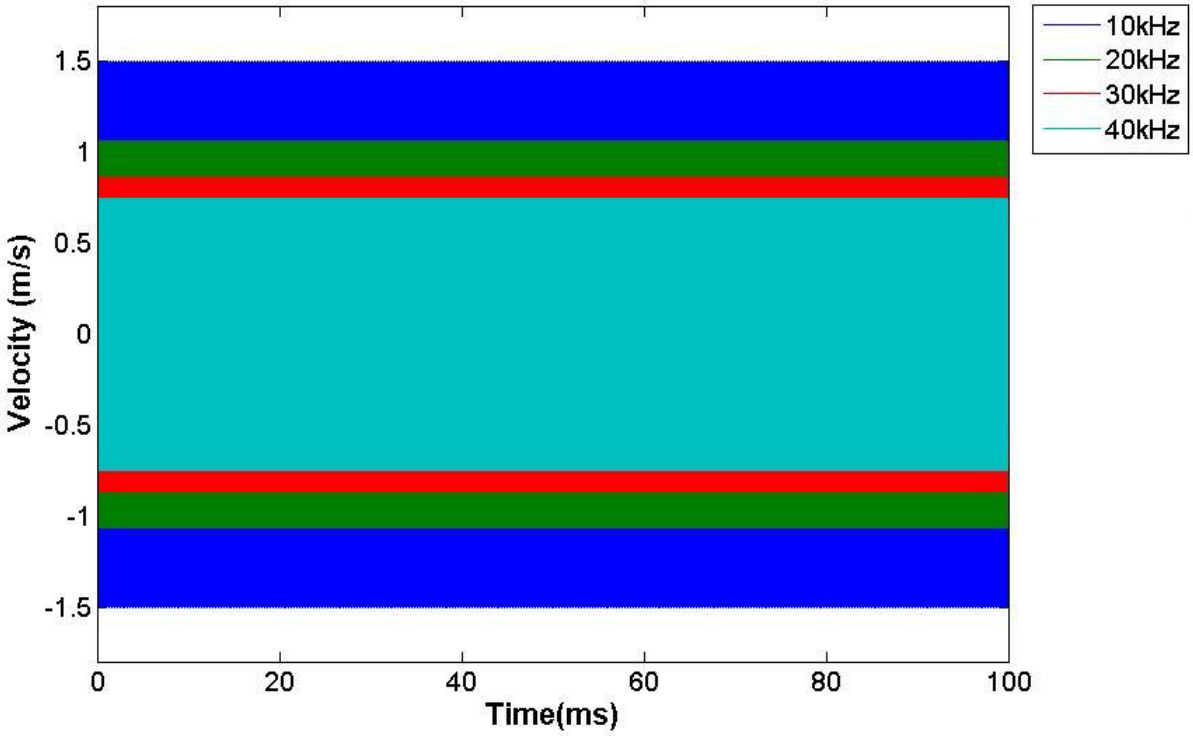

Figure 4.17: Amplitude comparison of the six different input frequencies

The total calculation time of each case in this study is set to be 200 ms which allows the temperature plots to show both the heating up and cooling down process. The excitation sources are induced into the sample at the beginning of the simulation and ended at 100ms of the simulation. Showed in Figure 4.18 are the temperature plots of the highest temperature points in each case. The first 100ms period is the heating up

process where we see temperature rising, and the second 100ms is the cooling process where we see temperature dropping.

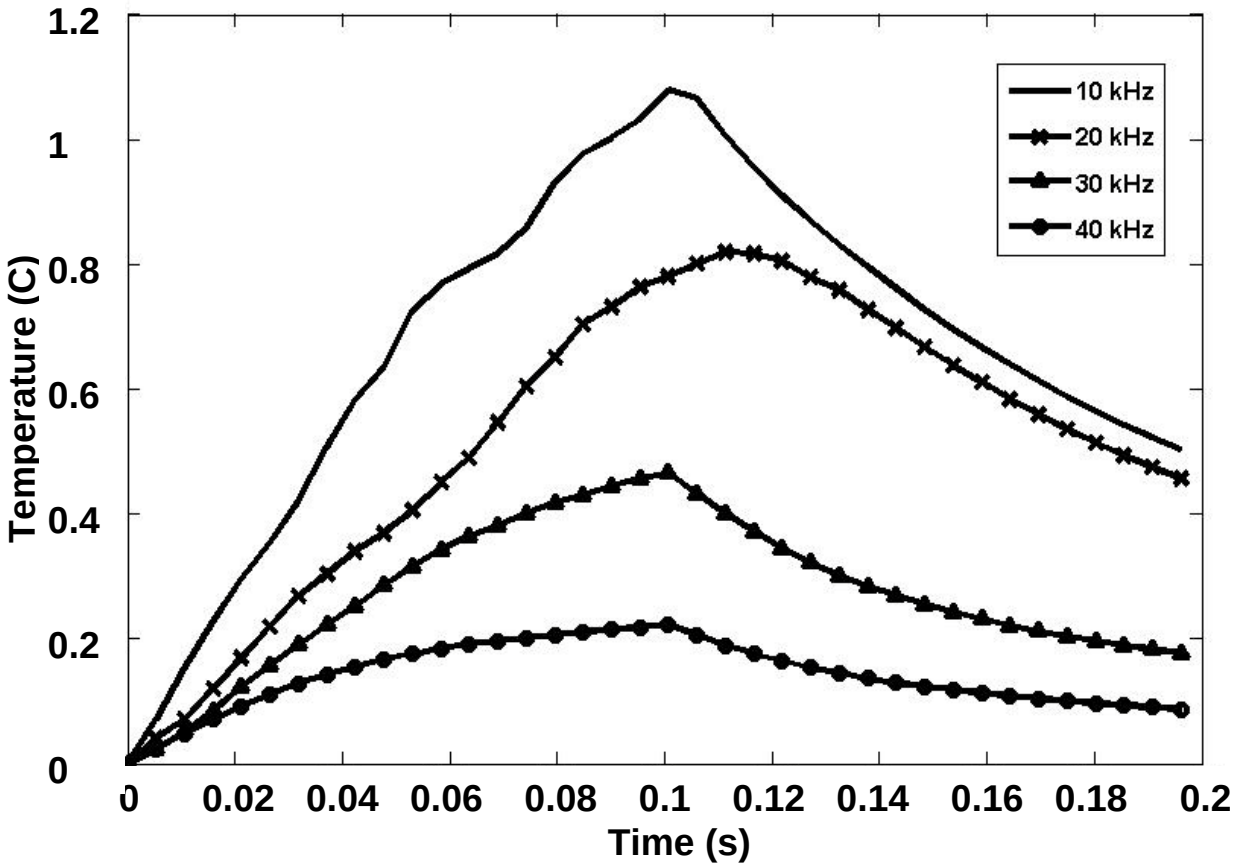

Figure 4.18: Temperature change comparison of four different input frequencies

In Figure 4.18, the plot shows the comparison of temperature change caused by four different input frequencies with the same input energy. From the plot, it clearly shows that 10kHz input pulse generated the highest temperature among all four input frequencies we used in the simulation, which are 10, 20, 30, 40 kHz, thought the all four frequencies we used as input sources had been adjusted to maintain the same energy level.

4.5.2 Simulation result analysis

In the previous section, we had found out that 10 kHz excitation with the highest vibration amplitude among all four inputs sources generated most heat and had the highest temperature change. In this section, a more close study will be conducted to find out the reason that low frequency vibration with higher amplitude generated more heat than high frequency vibration with low amplitude.

Before the study, it is better to know more information about how frication energy transfer into heat and what aspects would affect this change process. All we studied here are kinetic frictions because most frictions Sonic IR encounters during real time situation are kinetic frictions. And the study will majorly focus on kinetic friction.

During movement, an object lost its energy to kinetic friction. According to the law of conservation of energy, no energy is destroyed due to friction, though it may be lost to the system of concern. Energy is transformed from other forms into heat. A sliding hockey puck comes to rest because friction converts its kinetic energy into heat. Since heat quickly dissipates, many early philosophers, including Aristotle, wrongly concluded that moving objects lose energy without a driving force.

When an object is pushed along a surface, the energy converted to heat is given by:

$$E_{th} = \mu_{\mathrm{k}} \int F_{\mathrm{n}}(x)dx$$

where

F_n is the normal force,

μ_{k} is the coefficient of kinetic friction,

x is the coordinate along which the object travels.

From this equation, it is easy to notice that the heat generated by kinetic friction majorly affect by the F_n, μ_k and x, which are normal force applied on the object, coefficient of kinetic friction of the kinetic friction surface and the total travel distance of this object. In our case we used a single model for all four excitation source, so the coefficient of kinetic friction would stay the same for all four frequencies. All we need to study are the x, total travel distance of this object and F_n, normal force applied on the object.

In Figure 4.19, the highest temperature point, node 35907, is showed. Node 3797 is the corresponding node on the other side of the crack opposite to node 35907. The study on the relative motion of node 35907 and 3797 can provide us the information for total travel distance. The pressure data at node 35907 can provide information for normal force.

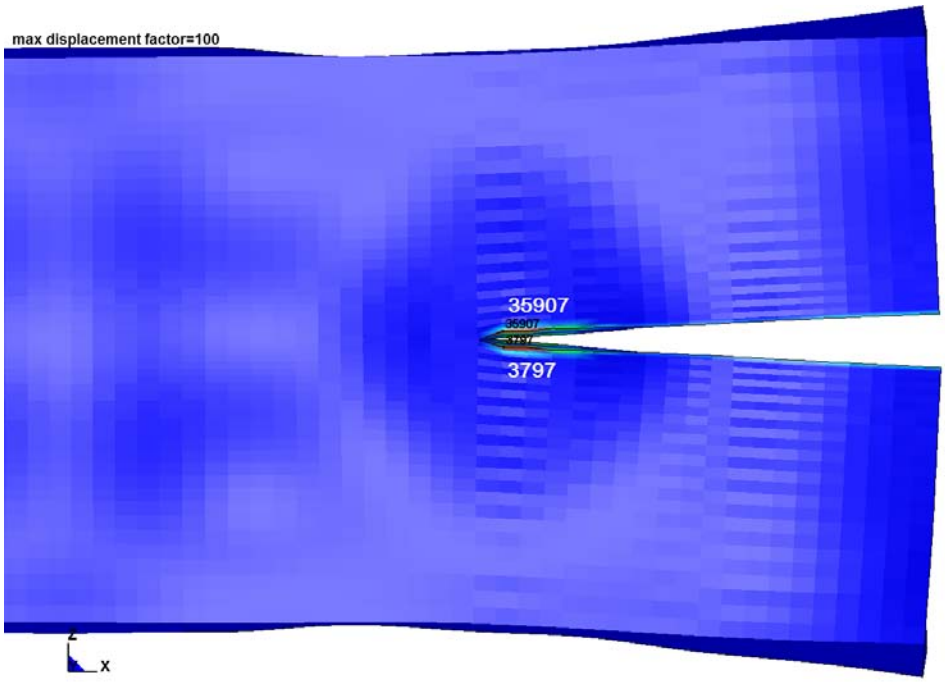

4.19: 10 kHz input highest temperature point

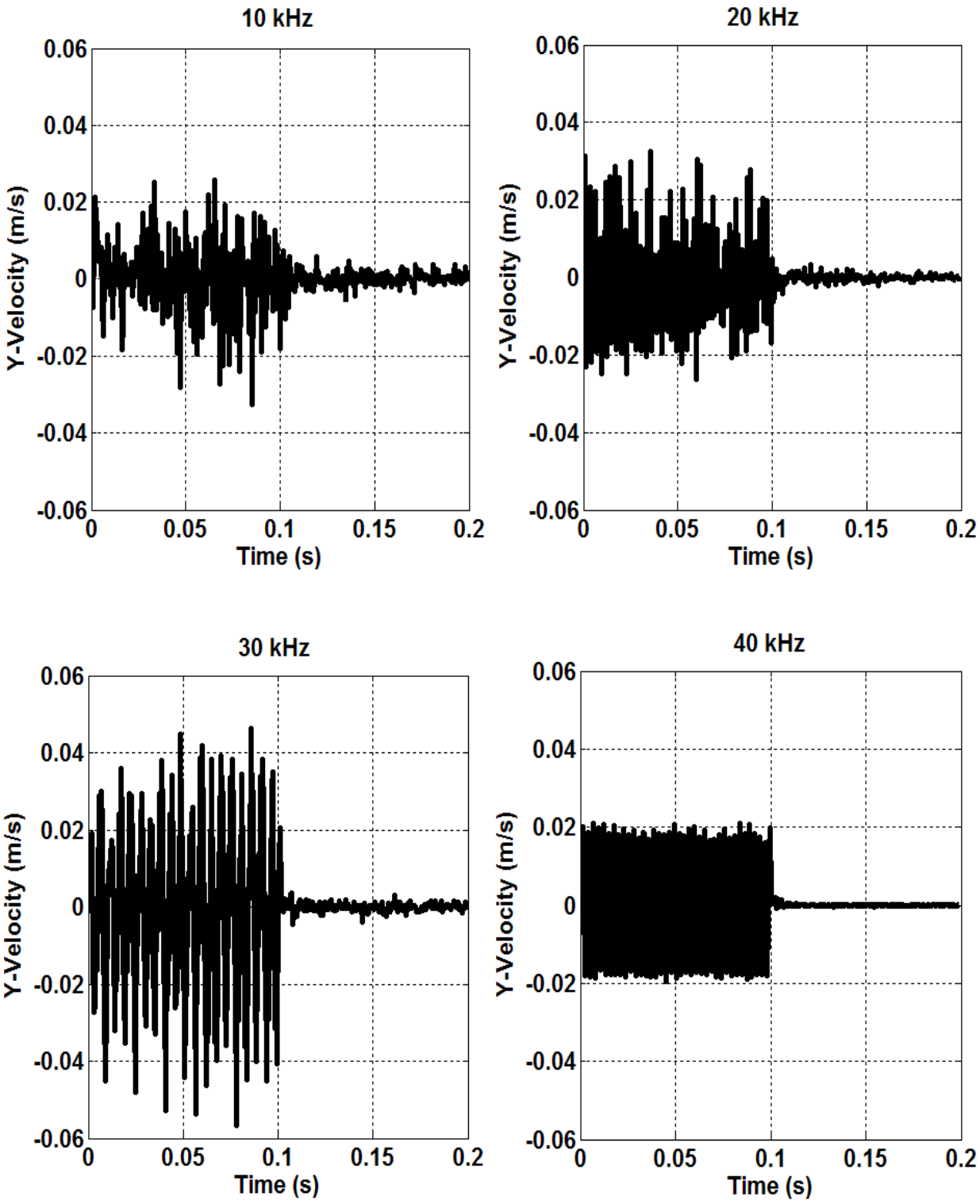

Figure 4.20: Comparison of relative Y-Velocity at the highest temperature points

In LS-Dyna, only the position, velocity, displacement and other similar information of the nodes at a certain moment are recorded in each stage output. There is no record of the total distance a node traveled during the simulation. However using the relative velocity of a node and its opposite node on the other surface of the crack during a fix period of time, we still can draw a big picture of the total distance a node traveled along a contain direction. Although the information acquired from the relative velocity is not enough for accurate calculation, it is enough for the analytical purpose.

Figure 4.20 shows the 30 kHz case has the highest relative velocity among all four cases, hence the highest temperature node in 30 kHz case has the longest travel distance. But a revisit paid to the temperature plots showed that 30 kHz case has the second lease heat generation. And the 10 kHz case which has the highest temperature change actually has a relative low velocity. This can confirm that in this simulation the total travel distance is not the dominant parameters affecting the heat generation. With the total travel distance had been ruled out as the dominant affecting aspect, the normal force is the next and last on the list to be examed.

In Figure 4.21, the pressure curves at the highest temperature point are showed. In this figure, we can see that 10 kHz frequency input source cause the highest pressure on the element where the highest temperature nodes resides, and 20 kHz source has the second highest pressure, 30 kHz input followed and finally 40 kHz has the lowest pressure among all four input frequencies. The order of the nodal pressure among four input frequency is exactly the same as the heat generation for the same group of input frequency.

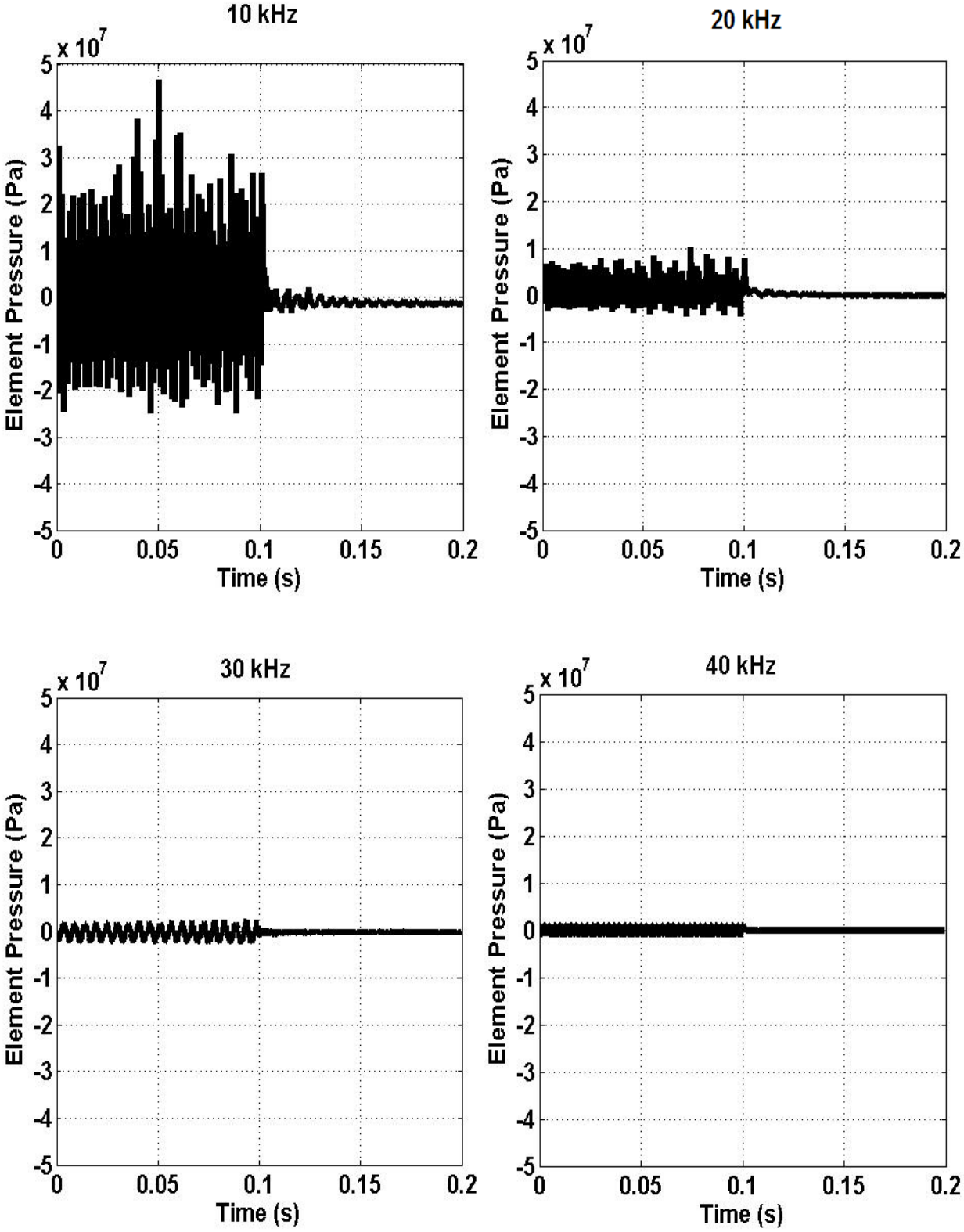

Figure 4.21: Comparison of element pressure at the highest temperature points

From the above analysis, it is reasonable to believe that the normal force caused by vibration on the highest temperature nodes is the dominant parameter affect the heat generation. The higher the normal force applied the more heat will be generated.

The major reason for this to happen is that steel has high elastic modulus and harder to deform. Higher vibration amplitude is needed to better excite the sample and create more normal force on the crack surface, which would leads to more heat generation.

4.6 Effect of material elastic modulus

In previous part, we found that the amplitude of the excitation signal is dominant among all the parameters that affect the heat generation in large steel structure with high elastic modulus. Here raised the question – what will happen when the sample high amplitude excitation source is applied on a low elastic modulus material? Will it vibrate more and generate more heat? With these questions in mind, the FEA model used above was modified. The elastic modulus of steel, 2.05e+11 Pa was changed to aluminum's elastic modulus of 7.31e+10 Pa. Aluminum is another often seen softer material in civil structures. All other parameter used in the FEA model is kept unchanged, so that we can confirm it is the elastic modulus which caused the difference. In the following part, the results will be presented and cause will be investigated.

Looking at the simulation results shown in Figure 4.22, under the same excitation source lower elastic modulus sample actually generated less heat than high elastic modulus. Is this caused by less vibration? The answer is no. After a close exam, we

found out the high amplitude excitation source vibrates the soft material too much that it keeps the crack open and reduced the normal force on the crack surface.

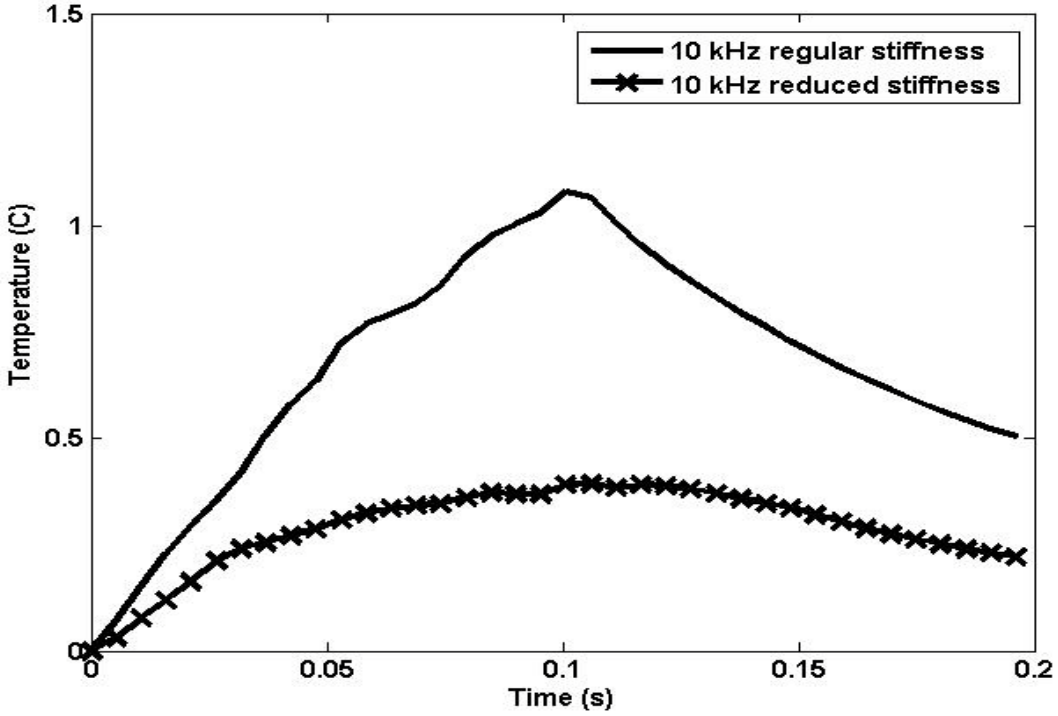

Figure 4.22: Temperature change comparison of regular and reduced elastic modulus

From the simulation result we found out that the high amplitude excitation source applied on the lower elastic modulus sample vibrates the sample at a much higher level due to the low elastic modulus. This higher vibration had caused the cracked to open up. In Figure 4.23, the distance between the two opposite crack surface in both high and low elastic modulus cases are shown. It is not hard to notice that the gap between 2 crack surfaces in the low elastic modulus case is higher than the high elastic modulus case. The gap almost doubled.

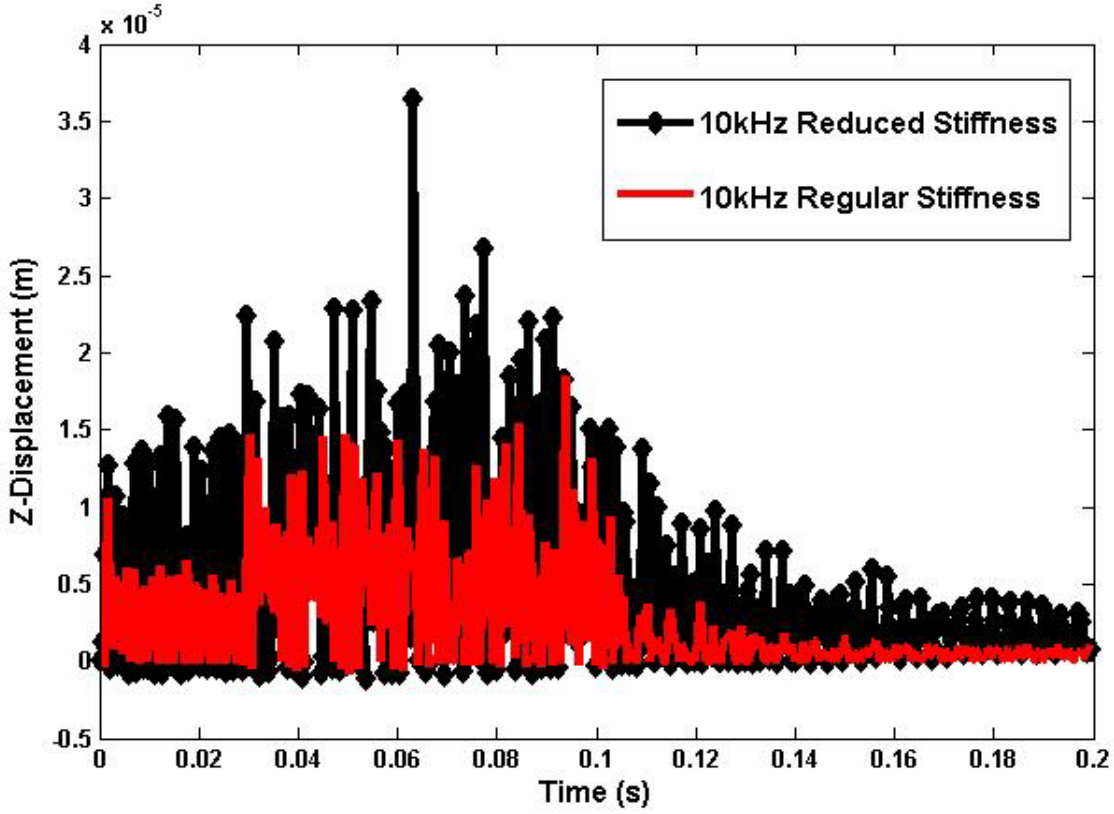

Figure 4.23: Z-displacement comparison of regular and reduced elastic modulus

The immediate consequence of this crack open-up is the decrease of normal force applied on crack surfaces. In Figure 4.24, the surface pressure of crack in both low elastic modulus case and high elastic modulus case are presented side by side for comparison. From the comparison, we can see the surface pressure of crack dropped almost half in the low elastic modulus case and cased less heat generation.

From this section of study we learnt that high amplitude excitation source on a low elastic modulus sample might cause the sample to be ‘over-excited’. High amplitude excitation source will vibrate the sample more which is good, however much of the energy would be wasted on open the crack. The increase on the gap distance between two crack surfaces also caused the drop of normal force applied on crack surface and

caused less heat generation. While choosing amplitude of excitation source, the elastic modulus of sample material also needed to be put into consideration.

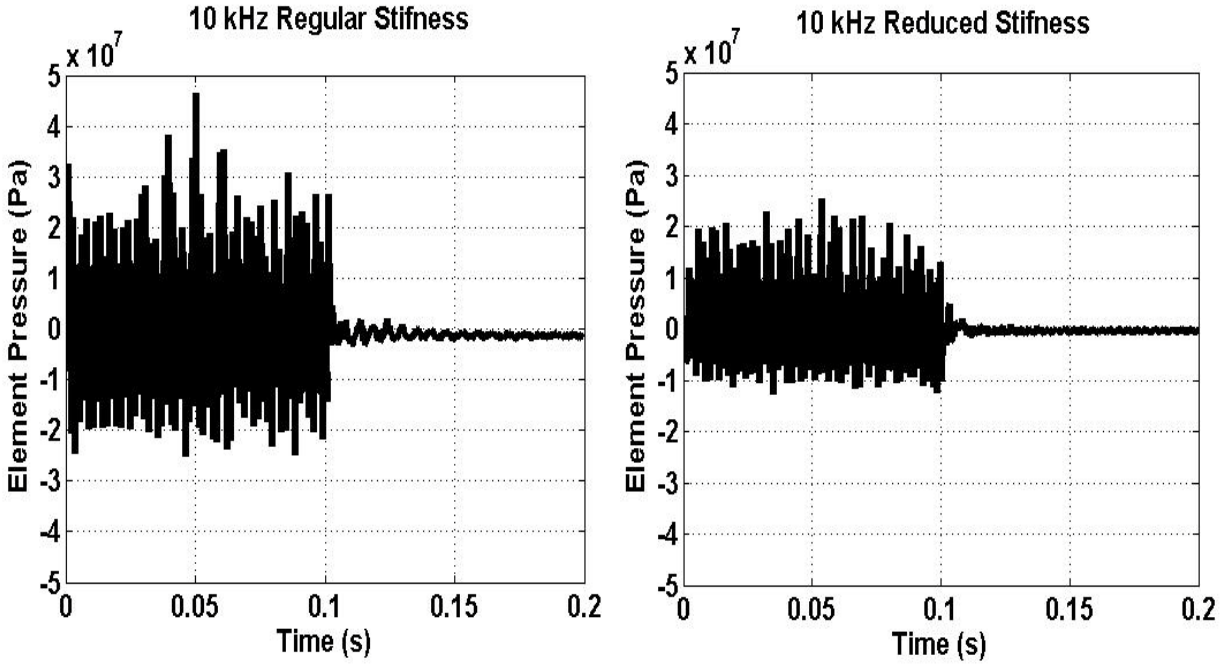

Figure 4.24: Element Pressure comparison of regular and reduced elastic modulus

Chapter 5

CONCLUSIONS AND FUTURE WORKS

The major goal and most important purpose of my research work is to study the application of sonic IR imaging technique on large size civil engineering structures like beams and channels and to find out the relationship between the input ultrasound excitation and the output IR signal in this technique. Finite Element Analysis is used to do simulations and gather data which are hard to gather or not available in real experiment. The approach I was taking is to do the experiment first and gather enough information through these experiments. Based on the information gather through real sample experiments, a finite element model was built. The real experiment results can be further used to confirm the finite element model simulation results. The comparison of experimental results and computational simulation results shows the reliability of the finite element models for further investigation, and the simulation results from different vibration frequency inputs give a clear picture of the relationship between input excitation sources and heat generation from the crack. All these knowledge learnt from this study can help us to make a better application of Sonic IR Imaging Technique in larger size civil engineering structures.

There are three conclusions we can draw from this paper:

1. Sonic IR Imaging technique is applicable for detecting cracks and defects in large size civil engineering structures. From the results of various real sample experiments we had conducted, Sonic IR Imagining had successfully detected all of the defects reside in the samples. In the DTE boiler tube case, Sonic IR imaging had beat the X-Ray exam by detecting all the defects that had been missed by the X-Ray test. All

these results had give us the confidence to introduce the Sonic IR Imaging NDE technique in to the civil engineering NDE field, and believe it would be one of the competitive members of the civil engineering structure NDE technology family.

2. The amplitude of the excitation source has a dominant effect on the heat generation in civil engineering structures where most materials have high elastic modulus. It is the nature of the Sonic IR Imaging technique that in detecting defects the amount of heat generated by the crack has a direct effect to the possibility of detection. The more heat the crack generates, the easier and accurate Sonic IR Imaging technique will detect the defects. With a better understanding of the relationship between the amplitude of vibration source and the heat generation on the crack surface, it is easier to choose right excitation source and get a better possibility of detection. This is very important for Sonic IR imaging technique to be a successful NDE technique in the civil engineering structure NDE family.

3. The situation of ‘over-excite’ which would leads to the decrease in heat generation while high amplitude excitation source is applied on low elastic modulus or soft material. During the study we found that when high amplitude excitation source is applied on materials with relatively low elastic modulus or softer material, the high vibration amplitude would not help to generate more heat but actually decrease the heat generation. The decrease of heat generation is caused by the open-up of the crack by high vibration amplitude and low elastic modulus which will decrease the normal force applied on crack surface. This finding would greatly help in selecting the right excitation source for different structures according to the material it is made o, thus achieve higher

probability of detection of defects. Higher probability of detection would definitely make Sonic IR Imaging technique a more attractive one among other NDE technologies.

Beyond the study included in this paper, there are still more works need to be done in the future. First of all, the frictional coefficients of both edge through crack and surface crack are currently adjusted according to the experimental results, and the shape of the crack is a straight line. That means a specific model is needed for a particular sample, and more finite element models with different shapes and different types of cracks need to be built. In addition, so far, both experimental and theoretical research work on SIR imaging are mainly focused on metallic materials. Nowadays more and more composite material had been used in civil structures, further work on composite materials and structures are to be carried out.

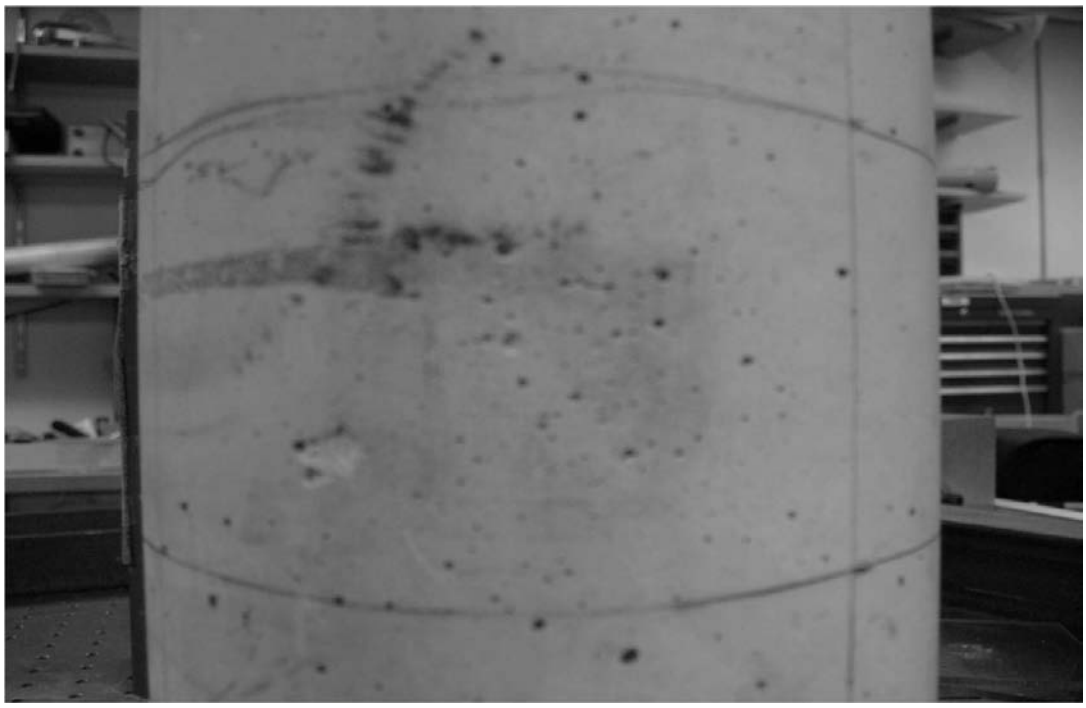

Figure 5.1: Heat Damage in a Concrete Pillar

Other than the materials listed above, we also laid our eyes on the most important material used in civil engineering constructions --- Concrete. Although concrete is a very common construction material, it is complicate material property make it difficult target for NDE research. Concrete is a mixture of several different materials, normal including: cement, aggregate, water, and chemical admixtures. Concrete solidifies and hardens after mixing with water and placement due to a chemical process known as hydration. The water reacts with the cement, which bonds the other components together, eventually creating a stone-like material.

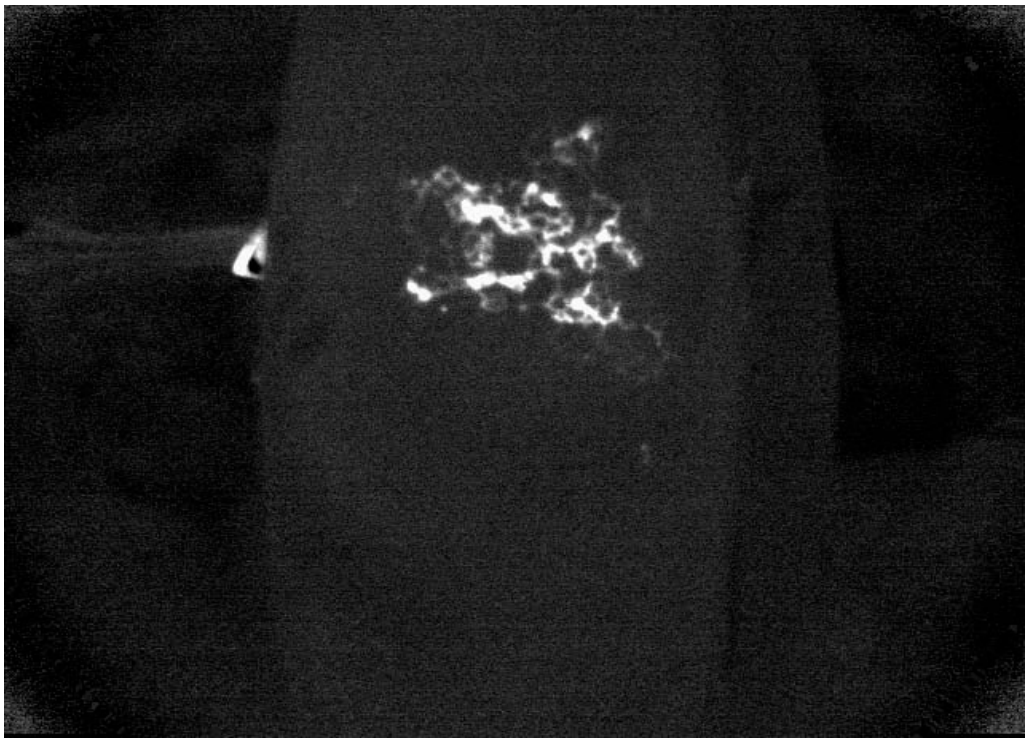

Figure 5.2: IR image taken during a Sonic IR Imaging Experiment of the Concrete Pillar

We had done some preliminary experiments on concrete structure, such like the concrete pillar demonstrated in Figure 5-1, which has cracks caused by fire damage.

Cracks in concrete structure due to fire damage are very common in buildings after a building under-went a fire disaster and can dramatically weaken the structure. Shown in Figure 5-2 is the cracks detected by Sonic IR Imaging technology in concrete pillar showed in Figure 5-1. Further study of Sonic IR imaging techinology on concrete structures is planed and will be carried out in the near future.

REFERENCES

1. Qi He, Xiaoyan Han, ***Crack Detection Using Sonic Infrared Imaging in Steel Structures: Experiments and Theory of Heating Patterns***, SPIE, *Smart Structures and Materials 2008*, Vol. 7292, 72920Q-1-7, 2009
2. YuYang Song, Garrett Godfrey, Xiaoyan Han, ***What Role A Coupling Material Could Play In Sonic Ir Imaging***, AIP, *Review of Progress in Quantitative Nondestructive Evaluation*, Vol. 28, pp511-517, 2009
3. Xiaoyan Han, Abhijith S Ajanahalli, Zeeshan Ahmed, Wei Li, G. Newaz, L.D. Favro, and R.L. Thomas, ***Finite Element Modeling of Sonic IR imaging of cracks in Aluminum and Titanium Alloys***, AIP, *Review of Progress in Quantitative Nondestructive Evaluation*, Vol. 27, pp 483-490, 2008
4. Marc Dubois, Tony Dunhill, Dong Fei, Xiaoyan Han, Tammana Jayakumar, Anton Lavrentyev, Eric Lindgren, Katy Milne (Alphabetic order), ***Perspectives in NDE Education***, AIP, *Review of Progress in Quantitative Nondestructive Evaluation*, Vol. 27, pp 1802-1825, 2008
5. Xiaoyan Han, Yuyang Song, Garrett Godfrey, ***Investigation of Non-Linear Effects of Coupling Materials in Sonic IR Imaging***, SPIE, *Smart Structures and Materials 2008*, Vol. 6932, 6932 on-1-6, 2008
6. Xiaoyan Han, ***Sonic Infrared Imaging: A novel NDE Technology for Detection of Crack/Delamination/Disbond in Materials and Structures***, Development in *Ultrasonic and Advanced Methods in NDT*, edited by C.H. Chen, World Scientific Publishing. July, 2007.

7. Jianping Lu, Xiaoyan Han, G. Newaz, L.D. Favro, R.L. Thomas, ***Study of the Effect of Crack Closure in Sonic Infrared Imaging***, *Journal of Nondestructive Testing and Evaluation, Special Issue on Thermographic Techniques and Results in Nondestructive Testing and Evaluation*, 127-135, September, 2007

8. Xiaoyan Han, Rui Yu, ***Studying the Effect of Coupling Materials in Sonic IR Imaging***, SPIE, *Smart Structures and Materials 2007*, Vol. 6529, pp 652937-1-6, 2007

9. Xiaoyan Han, Qi He, Nebojsa Sebastijanovic, Tianwei Mac, Henry T.Y. Yang, ***Developing Hybrid Structural Health Monitoring Via Integrated Global Sensing And Local Infrared Imaging*** , SPIE, *Smart Structures and Materials 2007*, Vol. 6529, pp 65291E-1-6, 2007

10. Xiaoyan Han, Md. Sarwar Islam, G. Newaz, L.D. Favro, and R.L. Thomas, ***Further Development of the simulation of Sonic IR imaging of cracks in Metals with Finite Element Models***, AIP, *Review of Progress in Quantitative Nondestructive Evaluation*, Vol. 26, pp 471-477, 2007

11. Xiaoyan Han, Md. Sarwar Islam, G. Newaz, L.D. Favro, R.L. Thomas, ***Finite-Element Modeling of the Heating of Cracks in Sonic Infrared Imaging***, *Journal of Applied Physics*, 99, 074905-1~ 074905-7,April, 2006

12. Xiaoyan Han, Qi He, ***Developing Thermal Energy Computing Tools for Sonic Infrared Imaging***, SPIE, *Smart Structures and Materials 2006*, Vol. 6174, pp 617432-1-7, 2006

13. Xiaoyan Han, L.D. Favro, G. Newaz, and R.L. Thomas, ***Recent Developments in IR Imaging with Chaotic Sound excitation for NDI of Aircraft Structures***, *9th joint FAA/DOD/NASA conference on Aging Aircraft*, pp-, 2006

14. Xiaoyan Han, Md. Sarwar Islam, G. Newaz, L.D. Favro, and R.L. Thomas, ***Simulation of Sonic IR Imaging of Cracks in Metals with Finite-Element Models***, AIP, *Review of Progress in Quantitative Nondestructive Evaluation*, Vol. 25, pp544-549, 2006

15. Joe Dimambro, Michael Ashbaugh, Xiaoyan Han, L. D. Favro, Jianping Lu, Zhi Zeng, Wei Li, G.M. Newaz, R. L. Thomas, ***The Potential of Sonic IR to Inspect Aircraft Components Traditionally Inspected with Fluorescent Penetrant and or Magnetic Particle Inspection***, AIP, *Review of Progress in Quantitative Nondestructive Evaluation*, Vol. 25, pp536-543, 2006

16. Xiaoyan Han, Md. Sarwar Islam, G. Newaz, L.D. Favro, R.L. Thomas , ***Finite-Element Modeling of Acoustic Chaos in Sonic Infrared Imaging***, *Journal of Applied Physics*, 98, 014907-1 -014907-4, July 1, 2005

17. Xiaoyan Han, J. Lu, Md. Sarwar Islam, Wei Li, Zhi Zeng, L.D. Favro, G. Newaz and R.L. Thomas, ***Sonic Infrared Imaging NDE***, Proceedings of SPIE-Volume 5765, Smart Structures and Materials 2005: Sensors and Smart Structures Technologies for Civil, Mechanical and Aerospace Systems, Masayoshi Tomizuka, Editor, May 2005, pp. 142-147.

18. Xiaoyan Han, J. Lu, Md. Sarwar Islam, Wei Li, Zhi Zeng, N. Kashyap, E. Yitamben, L.D. Favro, G.M. Newaz and R.L. Thomas, AIP, ***Developing***

Sonic IR Imaging NDE for Aircraft Structures**,** Review of Progress in Quantitative Nondestructive Evaluation, Vol. 24, pp. 632-636, 2005

19. Xiaoyan Han, Wei Li, Zhi Zeng, L.D. Favro, G.M. Newaz, and R.L. Thomas, ***Study The Effect Of Geometry In Sonic IR Imaging***, AIP, *Review of Progress in Quantitative Nondestructive Evaluation*, Vol. 24, pp637-641, 2005

20. Xiaoyan Han, V. Loggins, and Zhi Zeng, L.D. Favro, R.L. Thomas, ***Mechanical Model for the Generation of Acoustic Chaos in Sonic IR Imaging***, *Applied Physics Letters*, Vol.85, No.8, pp1332-1334, August 23, 2004

21. Xiaoyan Han, Zhi Zeng, Wei Li, Md. Sarwar Islam, J. Lu, V. Loggins, E. Yitamben, L.D. Favro, G. Newaz and R.L. Thomas, AIP, ***Acoustic Chaos for Enhanced Detectability of Cracks by Sonic Infrared Imaging***, Journal of Applied Physics, Vol. 95, No. 7, pp. 3792-3797, April 1, 2004.

22. Xiaoyan Han, Zhi Zeng, Wei Li, Md. Sarwar Islam, Jianping Lu, Vera Loggins, Lawrence Dale Favro, Golam Mohammed Newaz and Robert Leighton Thomas, ***Importance of Acoustic Chaos in Sonic IR Imaging NDE*****,** AIP, *Review of Progress in Quantitative Nondestructive Evaluation*, Vol. 23, pp496-500, February 26, 2004

23. Xiaoyan Han, Jianping Lu, L.D. Favro, Kathleen M. Garland, and Paul L. Benson, ***Infrared Imaging for Detection of Defects and Real-time Monitoring of a Consolidation Treatment in Stone Sculpture***,

AIP, *Review of Progress in Quantitative Nondestructive Evaluation*, Vol. 23, pp501-506, 2004

24. Xiaoyan Han, L.D. Favro and R.L. Thomas, ***Recent Developments in Sonic IR Imaging*****,** Review of Progress in Quantitative Nondestructive Evaluation, AIP, Vol.22, 2003, pp. 500-504.

25. Xiaoyan Han, ***Frequency Dependence of the Thermosonic Effect***, Review of Scientific Instruments, Vol. 74, No. 1, pp. 414-416, January, 2003

26. Xiaoyan Han, Md. Sarwar Islam, Wei Li, V. Loggins, J. Lu, Zhi Zeng, L.D. Favro, G.M. Newaz and R.L. Thomas, AIP, ***Acoustic Chaos in Sonic Infrared Imaging for cracks in Aerospace Components*****,** the International Journal on Structural Health Monitoring, pp. 1285-1292, 2003.

27. Xiaoyan Han, L.D. Favro, and R.L. Thomas, ***Development In Thermosonic NDE Technique***, The Nondestructive Characterization of Materials XI, 497, 2003

28. Xiaoyan Han, Md. Islam, Wei Li, V. Loggins, Jianping Lu, Zhi Zeng, L.D. Favro, G. Newaz and R.L. Thomas, ***Acoustic Chaos in Sonic Infrared Imaging of Cracks in Aerospace Components***, *The International Journal on Structural Health Monitoring*, pp1285-1291, 2003

29. Xiaoyan Han, L.D. Favro, and R.L. Thomas, ***Sonic IR Imaging And Vibration Pattern Studies Of Cracks In An Engine Disk***, AIP, *Review of Progress in Quantitative Nondestructive Evaluation*, Vol. 22, pp. 513-516, 2003

30. Xiaoyan Han, L.D. Favro, and R.L. Thomas, ***Recent Developments In Sonic IR Imaging***, AIP, *Review of Progress in Quantitative Nondestructive Evaluation*, Vol. 22, pp. 500-504, 2003

31. Xiaoyan Han, L.D. Favro, and R.L. Thomas, ***Development In Thermosonic NDE Technique***, the *Nondestructive Characterization of Materials XI*, 497, 2003

32. Xiaoyan Han, Wei Li, and Zhi Zeng, L.D. Favro, R.L. Thomas, ***Acoustic Chaos and Sonic Infrared Imaging***, Applied Physics Letters, vol.81, 17, pp3188-3190, October 21, 2002

33. Xiaoyan Han, L.D. Favro, Zhong Ouyang, and R.L. Thomas***, Recent Developments In Thermosonic Crack Detection***, Review of Progress in Quantitative Nondestructive Evaluation, Vol. 21, pp. 552-557, 2002.

34. Ignacio Perez, Xiaoyan Han, ***Pulsed Thermography Modeling****, Review of Progress in Quantitative Nondestructive Evaluation*, Vol. 21, pp. 564-571, 2002

35. Zhong Ouyang, L.D. Favro, R.L. Thomas, and Xiaoyan Han, ***Theoretical Modeling of Thermosonic Imaging of Cracks***, *Review of Progress in Quantitative Nondestructive Evaluation*, Vol. 21, pp. 577-581, 2002

36. L.D. Favro, Xiaoyan Han, Li Li, Zhong Ouyang, Gang Sun, and R.L. Thomas, ***Thermosonic Imaging for NDE*** , Review of Progress in Quantitative Nondestructive Evaluation, Vol. 20, pp. 478- 482, 2001.

37. L.D. Favro, Xiaoyan Han, Zhong Ouyang, and R.L. Thomas, ***Progress In Thermosonic Crack Detection***, Thermosense XXIII, 2001, SPIE Vol.4360 pp. 546-549

38. L.D. Favro, R.L.Thomas, Xiaoyan Han, Zhong Ouyang, Golam Newaz, and Dominico Gentile, ***Sonic Infrared Imaging of Fatigue Cracks*****,** The International Journal of Fatigue, Vol.23/1001, pp471-476, Dec. 2001.

39. X. Chen, Xiaoyan Han, G. Newaz, ***Damage Assessment In Thermal Barrier Coatings Using Thermal Wave Imaging Technique***, *ASME International*, 2001

40. Xiaoyan Han, L.D. Favro, R.L. Thomas, ***Thermosonic Imaging Of Cracks: Applications To Teeth***, the proceeding of *European Conference on Biomedical Optics, 2001*

41. Xiaoyan Han, L.D. Favro, and R.L. Thomas, ***Detecting Cracks In Teeth Using Ultrasonic Excitation And Infrared Imaging***, proceedings of the *International Biomedical Optics Symposium*, 2001, SPIE vol. 4256, pp.188-191

42. Xiaoyan Han, L.D. Favro, Li Li, Zhong Ouyang, Gang Sun and R.L. Thomas, ***Quantitative Thermal Wave Corrosion Measurements on a DC-9 Belly Skin in the Presence of Irregular Paint Thickness Variations***, *Review of Progress in Quantitative Nondestructive Evaluation*, Vol. 20, pp. 483- 486, 2001

43. L L.D. Favro, Xiaoyan Han, Zhong Ouyang, Gang Sun, and R.L. Thomas, ***Sonic IR Imaging: A novel crack-detection method***, The Fourth Joint DoD/FAA/NASA Conference on Aging Aircraft, May, 2000.

44. L.D. Favro, Xiaoyan Han, Zhong Ouyang, Gang Sun, and R.L. Thomas, ***Sonic IR Imaging of cracks and Delaminations***, the *11th International Conference in Photoacoustic and Photothermal Phenomena*, June 2000.

45. L.D. Favro, Xiaoyan Han, Zhong Ouyang, Gang Sun, Hua Sui, and R.L. Thomas, ***IR Imaging Of Cracks Excited by an Ultrasonic Pulse***, Thermosense XXII, 2000, SPIE Vol.4020 pp. 182-185

46. L.D. Favro, Xiaoyan Han, Zhong Ouyang, Gang Sun, Hua Sui, and R.L. Thomas, ***Infrared imaging of defects heated by a sonic pulse*****,** Review of Scientific Instruments, Vol. 71, P2418-2421, June 2000.

47. Indigo Systems, ***Phoenix Camera System User's Guide****.*

48. BRANSON Ultrasonic Corp., ***2000t Power Supply Instruction Manual****. 2000*

49. Polytec, ***Polytec Vibrometer Software:*** Theory manual.

50. Polytec, ***Laser Doppler Vibrometer,*** User manual***.***

51. Livermore Software Technology Corporation, ***LS-DYNA Keyword User's Manual***, version 970, April 2003.

52. John O. Hallquist, ***LS-DYNA Theoretical Manual***, Livermore Software Technology Corporation, May 1998.

53. Livermore Software Technology Corporation, ***LSPOST a New Post Processor for LS-DYNA***, May 1999

54. Altair Engineering, Inc, ***Altair HyperMesh User's Guide,*** version 6.0.

55. Altair Engineering, Inc, ***Altair HyperMesh Interfacing with LS-DYNA,*** version 5.1.

56. Robert D. Cook, David S. Malkus, Michael E. Plesha, Robert J. Witt, Concepts and Applications of ***Finite Element Analysis***, fourth edition 2001.

57. John D. Reid, ***LS-DYNA Examples Manual***, Livermore Software Technology Corporation, June 2001.

58. Klaus-Jurgen Bathe, ***Finite Element Procedures.*** 2002.

59. http://www.kettering.edu/~drussell/Demos/superposition/superposition.html

60. http://www.as.wm.edu/Nondestructive.html

61. http://www.cinde.ca/ndt.shtml

ABSTRACT

DEVELOP SONIC INFRARED IMAGING NDE FOR LOCAL DAMAGE ASSESSMENT IN CIVIL STRUCTURES

by

Qi He

December 2010

Advisor: Dr. Xiaoyan Han

Major: Electrical Engineering

Degree: Doctor of Philosophy

Nondestructive Evaluation (NDE) is an interdisciplinary field of study, which is concerned with the development of analysis techniques and measurement technologies for the quantitative characterization of materials, tissues and structures. Ultrasonic IR Imaging is a novel NDE technique, which combines a short ultrasonic pulse excitation and infrared imaging to detect defects in materials and structures. In this technique, a sound pulse with a frequency in the range of 20-40 kHz is infused on a target material for a short duration (usually less than one second). The sonic/ultrasonic sound waves travel into the material and cause rubbing and clapping between the surfaces of any defects (such as cracks, delamination) that may be present in that material. The rubbing causes friction that generates heat in the defect area and ultimately raises the temperature at that region. An infrared video camera is set up to record the series of IR radiation change from the target object. Ultrasonic Infrared Imaging technique has several advantages compared with other traditional NDE techniques. This technique is able to detect both surface and subsurface cracks and it is effective for metallic, ceramic and composite materials, it is also very efficient for detecting delaminations in coupled

structures, disbonds between coatings and substrates. This technique is wide-area, fast, non-invasive and truly dark-field since only the defects respond to the excitation.

The NDE technologies for structure health mentoring of civil engineering structures, like building and bridges, had always been a popular research area. The purpose of this research work is to explore the application potentials of Sonic IR Imaging NDE technique in civil engineering structures. Experiments had been done on various samples with different structures and materials. Finite Element Analysis had been used to correlate with experimental data. Multiple Finite Element models had been built for both structural and thermal analysis based on experiments with corresponding material prosperities and structure information to test the accuracy of Finite Element models. Study of the effects of excitation source frequency and amplitude, material stiffness on civil engineering structure Sonic IR Imagining technique were done using the experiment tested FEA models.

AUTOBIOGRAPHICAL STATEMENT

QI HE

Education:

- Ph.D. EE, Wayne State University, Detroit MI USA, 2010
- M.S. EE, Wayne State University, Detroit MI USA, 2004
- B.S. EE, Shanghai Jiaotong University, China, 2001

Research:

- Structure health assurance of civil engineering structure.
- Contact analysis of cracks in beam, channel and other construction materials.
- Ultrasound vibration analysis of civil engineering structure.
- Thermal analysis of high frequency friction.
- Ultimate strength and stress analysis of steel and aluminum structures.

Publications:

(1) "Progress on Developing Sonic Infrared Imaging for Defect Detection in Composite Structures", Xiaoyan Han, Qi He, Wei Li, Golam Newaz, Lawrence D. Favro, Robert L. Thomas, Review of Progress in Quantitative Nondestructive Evaluation, Vol. 29. AIP Conference Proceedings, Volume 1211, pp. 518-523, 2010

(2) “Crack Detection Using Sonic Infrared Imaging in Steel Structures: Experiments and Theory of Heating Patterns”, Qi He, Xiaoyan Han, *SPIE, Sensors and smart structures technologies for civil, mechanical, and aerospace systems 2009*, Vol. 7292, pp. 72920Q-72920Q-7, 2009

(3) “Developing Hybrid Structural Health Monitoring Via Integrated Global Sensing And Local Infrared Imaging”, Xiaoyan Han, Qi He, Nebojsa Sebastijanovic, Tianwei Mac, Henry T.Y. Yang, *SPIE, Smart Structures and Materials 2007*, Vol. 6529, pp65291E-1-6, 2007

(4) “Developing Thermal Energy Computing Tools for Sonic Infrared Imaging”, Xiaoyan Han, Qi He, *SPIE, Smart Structures and Materials 2006*, Vol. 6174, pp 617432-1-7, 2006